Development of ^{13}C Nuclear Magnetic Resonance Methods for Studying the Structural Dynamics of Nucleic Acids in Solution

by

Alexandar Louis Hansen

A dissertation submitted in partial fulfillment
of the requirements for the degree of
Doctor of Philosophy
(Chemistry)
in The University of Michigan
2009

Doctoral Committee:

    Associate Professor Hashim M. Al-Hashimi, Chair
    Professor Anthony H. Francis
    Professor Ayyalusamy Ramamoorthy
    Associate Professor Jens-Christian D. Meiner

2009

To my family and friends, who have supported me tirelessly throughout the years and given me strength when I had little left to give.

Acknowledgements

I would first like to thank my advisor, Hashim Al-Hashimi for all of his kindness and support throughout this adventure known as graduate school. Working with him has been a truly rewarding and inspirational experience that I will keep with me throughout my career. I would also like to thank all of the current and past members of the Al-Hashimi lab, who have become close friends and colleagues, for making coming to work never feel like work. Finally, I would especially like to thank my family who, despite my lack of phone calls, have always supported and encouraged me no matter what I do or how far away I am.

Table of Contents

List of Figures

List of Tables

List of Abbreviations

AIC — Akaike's Information Criteria

ARG — Argininamide

CSA — Chemical Shift Anisotropy

CSAa — CSA magnitude (in ppm)

DD — Dipole-dipole interaction

DFT — Density functional theory

DHPC — 1,2-Diheptanoyl-*sn*-Glycero-3-Phosphocholine

DMPC — 1,2-Dimyristoyl-*sn*-Glycero-3-Phosphocholine

DNA — Deoxyribonucleic Acid

D_{ratio} — Ratio of diffusion tensor components $D_{parallel}$ / $D_{perpindicular}$

E-RNA — Elongated RNA

E-TAR — Elongated TAR RNA

GDO — Generalized Degree of Order

HIV — Human Immunodeficiency Virus

HSQC — Heternuclear Single Quantum Coherence

Hz — Hertz

INEPT — Insensitive Nucleus Enhanced Polarization Transfer

J_{NN}-COSY — Trans-hydrogen bond Correlated Spectroscopy

kHz	Kilohertz (1000 Hz)
MHz	Megahertz (10^6 Hz)
ms	Millisecond (10^{-3} seconds)
NMR	Nuclear Magnetic Resonance
NOE	Nuclear Overhausser Effect (Enhancement)
ns	Nanosecond (10^{-9} seconds)
PAS	Principle Axis System
ppm	Parts per million
ps	Picosecond (10^{-12} seconds)
R_1	Longitudinal (spin-lattice) relaxation rate
$R_{1\varrho}$	R_1 in the rotating frame
R_2	Transverse (spin-spin) relaxation rate
RCSA	Residual Chemical Shift Anisotropy
RDC	Residual Dipolar Coupling
RMSD	Root Mean Squared Deviation
RNA	Ribonucleic Acid
S^3E	Spin-State Selective Excitation
TAR	Transactivation Response element
TD	TROSY-Detected
TROSY	Transverse Relaxation Optimized Spectroscopy
η	Chemical shift or Order tensor asymmetry
μs	Microsecond (10^{-6} seconds)

Abstract

An understanding of both structure and dynamics is essential to the full characterization of any biomolecule, but is especially relevant with respect to RNA for which dynamics is used in myriad ways to achieve functional complexity that would otherwise be inaccessible based on its rigid framework composed of only four chemically similar nucleotides. Due to experimental difficulties in resolving the plethora of motional modes that exist in RNA, their dynamical properties remain poorly understood. Solution nuclear magnetic resonance (NMR) is one of the most powerful tools for the characterization of structural dynamics, as it provides atomic level detail on a variety of timescales, from picoseconds to seconds. Spin relaxation measurements can in principle provide information at sub-nanosecond timescales, providing that internal motions are not correlated to overall molecular tumbling. Residual dipolar couplings and residual chemical shift anisotropies (RCSAs) report on the average global RNA structure and provide insight into sub-millisecond motions. Finally, chemical exchange measurements can provide quantitative kinetic information on the micro-to-millisecond timescale. Unfortunately, many of the techniques commonly used for studies of RNA are limited to nitrogen resonances, which are not frequently observable in functionally relevant, non-canonical regions of RNA. In addition, target RNAs are relatively small, typically less than 30 nucleotides or 10,000 molecular weight. In this thesis, I develop the much needed NMR methods which can target the carbon nuclei of RNA and in systems up to 150 nucleotides. A combination of new spin relaxation, RCSA, and chemical exchange techniques are developed to probe site specific motions over the picosecond to

millisecond time regime and provide important insight into some of the fundamental properties of RNA. Spin relaxation revealed a surprisingly complex dynamical landscape for the relatively simple transactivation response element from HIV-1 RNA where intriguing entropy compensation occurs upon ligand binding in the bulge region, with order parameters of 0.2-0.3, as global domain motions are suppressed. New, selective $R_{1\rho}$ dispersion experiments detected previously unobservable chemical exchange in functionally important regions of the bacterial ribosomal A-site RNA, with a timescale of 320 μs, and the modified base in a 1,N6-ethenoadenine - damaged DNA.

Chapter 1. Introduction

The molecular machinery within a cell is critically important for maintaining the viability of the cell. The ribosome, a 2.5 megadalton nucleoprotein complex made of 3 large RNAs and over 50 proteins, is a prime example of this machinery that produces the numerous proteins found in the cell by translating the genetic code from a messenger RNA (mRNA).[1] Riboswitches, cis-acting gene control elements found in the 5′ untranslated region (UTR) of many mRNAs, regulate the gene expression in response to changes in various physiological parameters. After the initiation of transcription, transfer RNAs (tRNA) are recruited to insert the correct amino acid in the sequence and then leave to allow translocation in the protein elongation cycle. This continues until a stop codon is reached in the mRNA and the complete protein is released. Every step along the way, molecular motions have been involved in order to allow the process to continue: from local fluctuations to accommodate the recognition of a particular mRNA or tRNA structure, to dramatic secondary structure rearrangements in the formation of new helical elements. A description of these motions is therefore essential to understand how they drive biomolecular function. This is especially true for nucleic acids which use dynamics to add diversity to an otherwise simple chemical and structural makeup.[2]

Evidence for significant internal motions in large biomolecules has existed for over 50 years.[3] These ubiquitous motions have timescales ranging from picoseconds for localized motions in the sugar or nucleobases, to seconds or longer for global conformational changes and translation/transcription processes. Peptide bond formation occurs about ten times per second and can be thought of as an upper limit of one or more of the regulatory steps during transcription.[4] For example, the ribosomal A-site RNA decodes the mRNA message by dynamically flipping out two internal loop adenines once a proper codon/anti-codon mini helix is formed between the amino-acyl

tRNA and mRNA. Base flipping motions like this have been found to occur over tens of milliseconds.[5] On the other hand, modified bases in DNA sequences, which play an important role in recognition by repair enzymes, may occur much faster if a number of stabilizing interactions of a canonical base pair are disrupted. These damages disrupt the canonical structure of DNA, allowing sequence specific recognition by various cognate proteins.[6]

Large conformational changes can include secondary structural rearrangements and long range domain reorientations. The former is a characteristic feature of the newfound class of RNA riboswitches mentioned above. Purine-sensing riboswitches accomplish this by forming a transcription (anti)terminator helix at a downstream decision-making expression platform when the physiological concentration of the specific purine under control reaches a predefined threshold.[7]. Recently these RNAs have attracted interest as potential antibacterial targets, given their abundance in bacteria and their ability to bind small molecules. The guanine-sensing riboswitch (G-switch) in particular is found in many bacterial species, including the pathogen associated with anthrax, and is thought to exist as several slowly (30-60 s^{-1}) interconverting conformers in the absence of guanine.[8] Different riboswitches act as either kinetic or thermodynamic switches and have been carefully tuned by evolution for their particular function. Understanding these dynamics will likely be crucial in developing successful new antibiotics.

Global domain reorientations can best be illustrated in the transactivation response element (TAR), a highly conserved RNA element located at the 5'-end of the UTR of the human immunodeficiency virus (HIV) RNA genome.[9] TAR is a natively bent and flexible RNA that must rearrange itself to a more linear state to accommodate binding of the cognate protein Tat.[10,11] Subsequently, additional proteins bind to the TAR-Tat complex in order to hyper-phosphorylate the polymerase, increasing its elongation efficiency to produce viral mRNA.[12,13] By understanding these processes, it may be possible to design therapeutics that target these key regions and prevent viral replication, killing the virus.

Due to the complexity of these motions in nucleic acids, it is difficult to obtain enough experimental measurements to fully describe them and therefore they remain poorly understood. Here, nuclear magnetic resonance (NMR) can be an invaluable asset as it provides unrivaled structural and dynamic information with atomic resolution. Using a variety of experimental techniques, NMR is capable of probing motions over the entire range of biologically relevant timescales. Among the earliest applications of NMR was nuclear spin relaxation which monitors the decay of nuclear magnetization.[14] The rate of decay is dependent on the size and shape of the molecule being studied, the strength of the external magnetic field, and internal motions. Biomolecules typically have global rotational diffusion times on the order of several to tens of nanoseconds, thus setting the upper limit of the timescales accessible to the analysis of spin relaxation rates. While it may be expected that local base wobbling or sugar puckering fall within this limit, global motions, such as diffusion-limited domain reorientations, can also occur on this timescale.[15]

Slow changes in the chemical environment of a nucleus, such as a base flipping from a helical to a solvent exposed state, can introduce another relaxation mechanism known as chemical exchange that is sensitive to motions on the microsecond to millisecond timescale.[16-19] These experiments in particular can provide a wealth of information regarding the kinetics of the dynamic event. Alternatively, fundamental parameters, such as chemical shifts and scalar couplings, can be monitored when the biomolecule is partially aligned with respect to the external magnetic field to produce residual chemical shift anisotropies (RCSAs)[20,21] and residual dipolar couplings (RDCs).[22,23] These measurements provide long range structural information that complements the common short distance constraint measurements, nuclear Overhausser effects (NOEs), which are often sparsely available in nucleic acids as compared to the higher proton density in proteins. RDC and RCSA measurements can also provide rich information about the dynamics of the nucleic acid that occur over timescales faster than milliseconds, supplementing the results of spin relaxation and chemical exchange.[24] Further NMR experiments, such as ZZ-exchange or real-time NMR, can probe motions

up to hundreds of milliseconds and longer.[25,26] However, most of these techniques have been developed almost exclusively for the backbone amide nitrogen spins of proteins. While they are often readily applicable for imino nitrogens in nucleic acids, these nuclei are only observable when they belong to highly structured Watson-Crick base paired regions, whereas in the functionally relevant, non-canonical loops and bulges are mostly unobservable. It is therefore critical to develop these techniques to study the abundant carbon nuclei in the backbone and nucleobases of RNA and DNA nucleotides. In addition, most nucleic acids studied by NMR are relatively small, often less then 30 nucleotides or 10 kDa owing to a number of experimental complications.[27-31] In this thesis, we aim to develop these much needed NMR methods which can target the carbon nuclei of nucleic acids in systems larger than 70 nucleotides or 25 kDa. These techniques will then be used to study the dynamical landscape for the relatively simple transactivation response element (TAR) from HIV-1 RNA and other representative nucleic acid samples.

1.1 The History of Nucleic Acid Dynamics and NMR

The study of nucleic acid structure and dynamics and the development of NMR have occurred roughly over the same period of time (Figure 1.1). The first NMR studies of bulk materials, water and paraffin, occurred in late 1945 by the groups led by Bloch[32] and Purcell[33] with theoretical and instrumental developments in the following year.[34,35] In the early 50s, the first reports of nucleic acid structure appeared in the journal <u>Nature,</u> [36,37] including the landmark discovery of the DNA double helix.[38,39] It took a number of years before the two topics met, with the first proton spectra of polynucleotides taking place in 1964 by two separate groups.[40,41] These early studies predated FT-NMR[42,43] and effective water suppression techniques and were conducted in 100% D_2O solutions. Temperature dependent studies of the proton spectra for polyU and polyC, although polydisperse, were found to have considerable disorder and flexibility about the ribose backbone above room temperature, while polyA and polyI showed a larger degree of
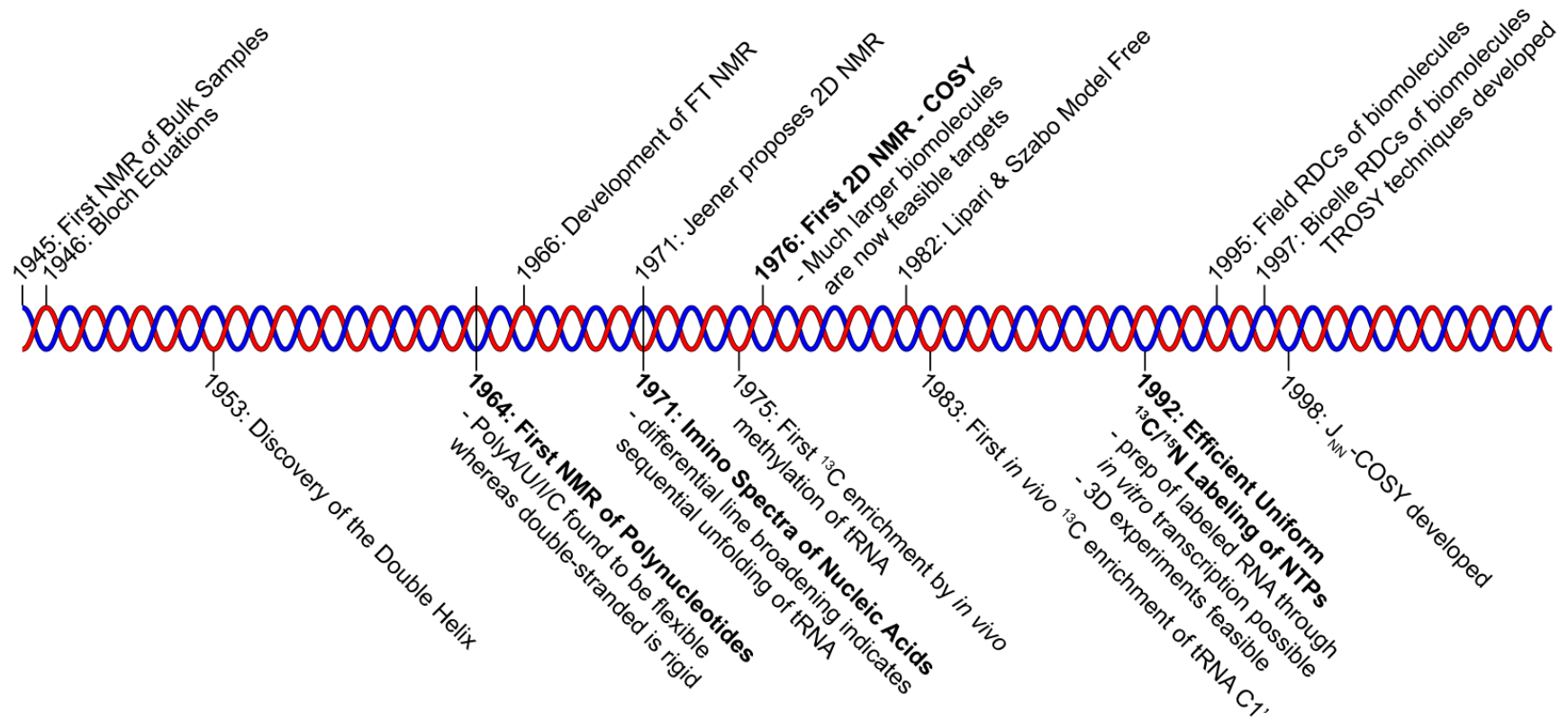
Figure 1.1. Timeline of the progress of nucleic acids studies by NMR.

1945: First NMR of Bulk Samples
1946: Bloch Equations
1953: Discovery of the Double Helix
1964: First NMR of Polynucleotides
- PolyA/U/I/C found to be flexible whereas double-stranded is rigid
1966: Development of FT NMR
1971: Jeener proposes 2D NMR
1971: Imino Spectra of Nucleic Acids
- differential line broadening indicates sequential unfolding of tRNA
1975: First ^{13}C enrichment by in vivo methylation of tRNA
1976: First 2D NMR - COSY
- Much larger biomolecules are now feasible targets
1982: Lipari & Szabo Model Free
1983: First in vivo ^{13}C
1992: Efficient Uniform $^{13}C/^{15}N$ Labeling of NTPs
- prep of labeled RNA through in vitro transcription possible
- 3D experiments feasible
^{13}C enrichment of tRNA C1'
1995: Field RDCs of biomolecules
1997: Bicelle RDCs of biomolecules
TROSY techniques developed
1998: J_{NN}-COSY developed

order. Mixtures of polyA and polyU or polyI and polyC were found to be completely ordered below ~50°C. Signals from tRNA samples similarly showed about 15-25% disorder at 31°C and broad ribose and aromatic resonances indicated a larger variety of local magnetic environment compared to the homopolymers. Later, the first spectra of tRNA in water were recorded by Kearns, Patel, and Shulman[44] and highlighted the exchangeable imino proton region, which is far enough downfield from the significant water resonance to be measurable. These resonances were immediately found to be a good indicator of the number of base pairs in an RNA since a single Watson-Crick pair contributes only one resonance to the region between 12 and 15 ppm. The presence of these peaks indicated lifetimes of the base-paired regions of >2 ms, slow on the NMR timescale, that then broaden out as temperature is increased past its melting temperature, thus allowing the protons to exchange with water at significantly faster timescales. The observation of differential line broadening of the imino resonances as a function of temperature in this first study, as well as in the many experiments that followed, was attributed to sequential unfolding of the tRNA, beginning with tertiary interactions, and followed by the TψC stem, D stem, the anticodon stem, and finally the acceptor stem.[45-48] It was therefore recognized early on that dynamics would play an important role in understanding nucleic acid function.

While the majority of the early magnetic resonance studies in the 1960s and 1970s focused on the abundant proton spins, experiments using other spin-½ nuclei were also investigated. The natural isotope of phosphorus, ^{31}P, is about a tenth as sensitive as protons and is therefore a good reporter on the structure and dynamics of the nucleic acid backbone. In the early 1970s, the ^{31}P spectrum of tRNAs recorded by Guéron was found to be partially resolved allowing investigations of pH and divalent metal ion titrations as well as melting studies.[49,50] Phosphorus relaxation studies were also used to identify fast (~0.5 ns) temperature- and salt-independent local motions in the backbone of large RNAs and DNAs.[51] However, with the advent of superconducting magnets around that time, it was noticed that the dominant relaxation mechanism was the chemical shift anisotropy (CSA), which increases with the square of the magnet strength,

thus counteracting the sensitivity gains typically associated with higher fields. Fluorine, being nearly as sensitive as the proton, 100% naturally abundant as the spin ½ nucleus ^{19}F, and having a larger chemical shift range than protons was incorporated into the uridine bases of tRNA[52] and 5S RNA[53] from E. coli. However, like ^{31}P, its sizeable CSA counteracts the sensitivity gains that could be achieved by going to larger magnetic fields. Despite their obvious biological significance, the carbon and nitrogen nuclei suffer from poor sensitivity (3 and 0.3% of hydrogen, respectively) and very low natural abundance of their spin ½ isotopes ([15]N = 0.37%, [13]C = 1.07%) and required the development of more sensitive heteronuclear NMR techniques[54,55] and/or isotopic enrichment strategies.

Like the first proton spectra, the first recorded ^{15}N spectra in 1975 were of unfractionated tRNA samples.[56] By growing cells in media containing ^{15}N-enriched ammonium chloride, Lapidot et al. showed that tRNA[57], and later DNA[58], could be uniformly ^{15}N labeled, although the sample mixtures could only reveal some basic
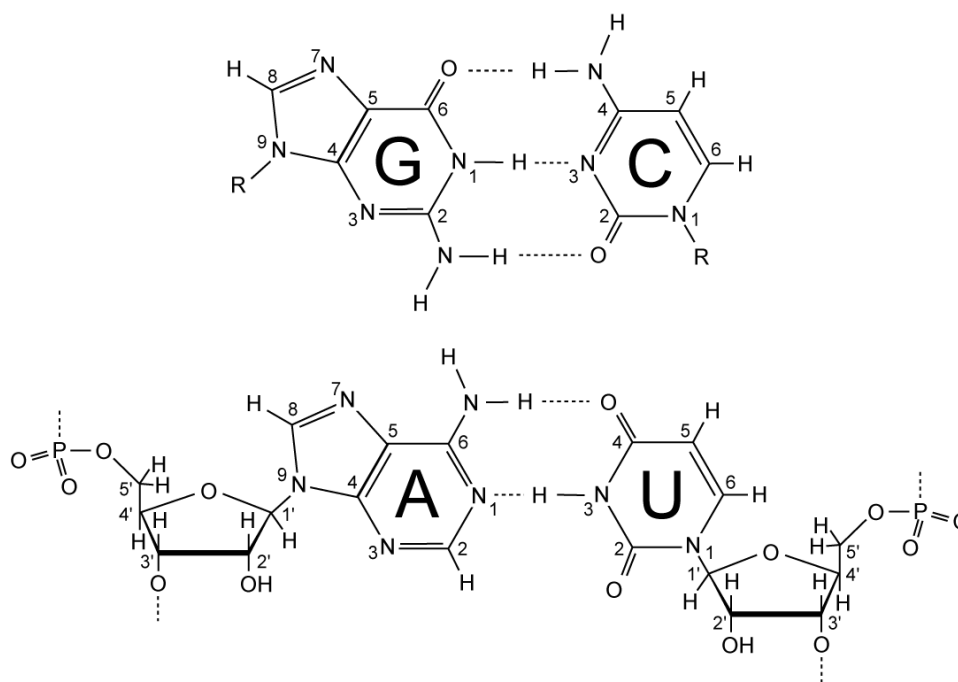
Figure 1.2. RNA mononucleotides. In DNA, the 2' hydroxyl is replaced with a hydrogen and the uridine base is replaced with thymine by substituting a methyl group at the H5 position.

information about the new spin system. Similar studies of ^{13}C were also limited to unfractionated tRNAs and DNAs.[51,59] Relaxation studies of various single- and double-stranded DNAs showed differences in local mobility of the ribose carbons (Figure 1.2), increasing from C1'/C3'/C4' to C2' and finally C5' having the largest degree of freedom. Attempts to isotopically label specific sites in the nucleobase and ribose found success at incorporating [13]C4 of uracil[60,61], [13]C2 of adenine, uracil, and cytidine[62], and ^{13}C-methylation of tRNA[63] (Figure 1.2). In a purified sample of [13]C4-uniformly labeled tRNA, spectra showed single resonance resolution and allowed a temperature-dependent relaxation study of the system.[60] Here, Olsen et al. were able to construct a detailed first description of the dynamics of the tertiary interactions. Relaxation studies of uniformly [13]C1' labeling of tRNA conducted by Schmidt and Agris, although not residue specific, found large amplitude internal motions of about 2 ns, similar to the motions observed in DNA samples.[64] It was not until 1992 when the groups of Pardi and Williamson proposed strategies for uniform ^{13}C/^{15}N labeling of nucleotide 5' triphosphates (NTPs). This finally made it possible to synthesize virtually any RNA sequence using <u>in vitro</u> transcription and enabled the use of 3-dimensional NMR techniques.[65-67] Among the first RNAs prepared using this new method was the transactivation response element (TAR) RNA from the human immunodeficiency virus (HIV). Multidimensional ^{13}C relaxation studies showed a complex profile of ps-ns timescale dynamics of the pyrimidine C6 and purine C8 nuclei, with the most mobility found at the internal trinucleotide bulge and in the several loop residues.[68]

Most recently, three experimental techniques were developed that have revolutionized biomolecular NMR studies. In 1997, Pervushin et al. demonstrated the sensitivity and resolution-enhancing effects of cross-correlated relaxation on [15]N-^{1}H spectra of large proteins.[69] In particular, the dipolar and CSA interactions destructively interfere with each other for one component of the [15]N-^{1}H doublet resulting in significantly decreased transverse relaxation rates. Experiments developed to exploit this effect are termed Transverse Relaxation Optimized Spectroscopy (TROSY). In the same year, Bax and coworkers showed how liquid crystalline media can be utilized to

impart partial molecular alignment to biomolecules and subsequently extract residual dipolar couplings (RDC) from scalar coupling measurements under these conditions.[23] RDCs, and later residual chemical shift anisotropies (RCSAs),[20,21] provide long range orientational restraints useful for structure determination. This is particularly true for nucleic acids which are poorly defined owing to their elongated structure and a dearth of usable short range proton distance restraints that are typically used in protein structure determination. Finally, in 1998, Dingley and Grzesiek reported the first observation of scalar couplings across the hydrogen bonds of Watson-Crick base pairs and developed experiments to generate correlations between the imino nitrogens of the nucleobases.[70] These correlations allow unambiguous characterization of the base pairing of nucleic acids, thus benefitting resonance assignment and providing information regarding relative hydrogen bond strengths. Since these seminal achievements, application of NMR to the study of nucleic acids has spread to a wide variety of constructs, including pseudoknots[71], quadruplexes[72], mRNAs elements[73,74], ribozymes[75-77], and riboswitches.[78]
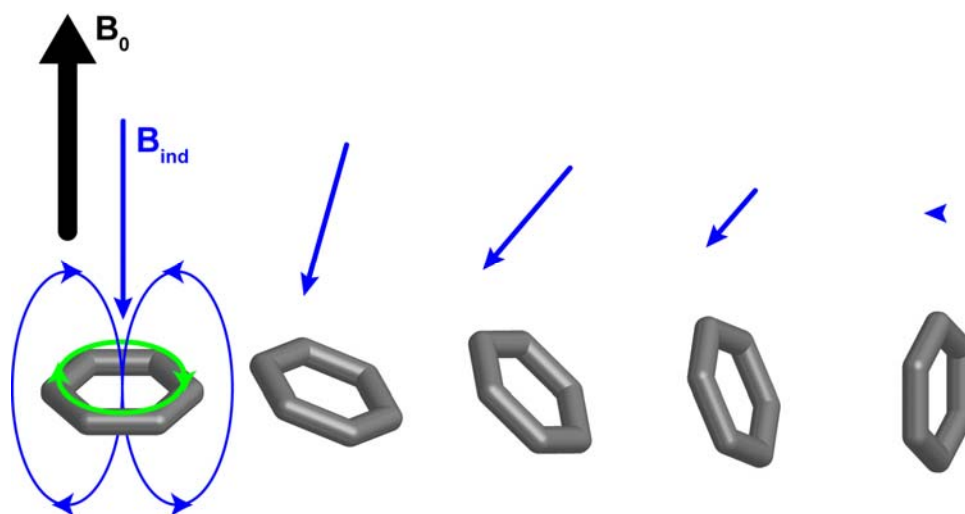
Figure 1.3. Orientation and magnitude dependence of induced magnetic fields (blue) from the circulation of electrons (green) in an aromatic ring.

1.2 Theory

Of interest to the current discussion are descriptions of the dipolar and the chemical shielding interactions and how they give rise to residual anisotropic interactions and nuclear spin relaxation. NMR active nuclei generate their own local magnetic fields which can be felt by neighboring nuclei as a perturbation of the external magnetic field. This dipolar interaction manifests as a resonance splitting in anisotropic solutions, RDC, and is a dominant component of nuclear spin relaxation. The atomic resolution of NMR however results from differences in the electronic environment of various nuclei in a biomolecule known as chemical or nuclear shielding. Circulation of electrons surrounding the nucleus will generate local magnetic fields that introduce perturbations of the external magnetic field observed by the nucleus. An idealized picture of this can be understood by the circulation of electrons in an aromatic ring (Figure 1.3). When the ring normal is parallel with the external magnetic field, a current is induced resulting in a left-handed circulation of the electrons. This circulation generates a magnetic field through the center of the ring that is opposed to the external field and an additive interaction to the protons on the periphery of the ring, resulting in a deshielding of the nuclei and pushing them to higher resonance frequencies compared to a bare nucleus. The effect on the resonance frequency is described by

$$\omega = -\gamma (1-\sigma) B_0 \tag{1.1}$$

where ω is the resonance frequency, γ is the nucleus-specific gyromagnetic ratio, σ is the chemical shielding, and B_0 is external magnetic field strength. While <u>shielding</u> represents the physical phenomenon of local magnetic fields altering the effect of the external field on a nucleus, chemical <u>shifts</u> represent the change in resonance frequency with respect to a common reference resonance:

$$\delta = \frac{\omega - \omega_{\text{ref}}}{\omega_0} = \sigma_{\text{ref}} - \sigma \,. \tag{1.2}$$

The chemical shift, δ, and likewise chemical shielding, σ, are very small numbers and

conventionally reported in parts per million (ppm). Returning to the aromatic ring example, if the ring were rotated in the magnetic field, the current would reduce to zero as the plane normal becomes perpendicular to the external magnetic field, neglecting other electron circulation in the molecule. Clearly, shielding is not a scalar quantity, nor is the induced magnetic field necessarily in the same direction as the external magnetic field. The anisotropic component of chemical shielding (CSA) therefore can result in perturbations to the chemical shift in anisotropic solutions and is another source of spin relaxation. A theoretical development of residual interactions and spin relaxation involves averaging the appropriate spin Hamiltonians under isotropic and non-isotropic solution conditions.[79-83]

While some fundamental concepts of nuclear magnetization can be understood using a classical mechanics description of the bulk magnetization vector, a quantum mechanical representation of the magnetization, known as the density matrix formalism, is required to accurately describe nuclear spin dynamics, which will be relevant to the topics of spin relaxation and the residual anisotropic interactions. For diamagnetic molecules, the nuclear spin Hamiltonian takes the general form

$$\mathcal{H} = \mathbf{u}^T \, \mathbf{R}^\lambda \, \mathbf{v} \tag{1.3}$$

where $\mathbf{u}$ and $\mathbf{v}$ are angular momentum ($\mathbf{u}, \mathbf{v}^T = \{I_x, I_y, I_z\}$) or magnetic field vectors ($\mathbf{v}^T = \{0, 0, B_0\}$), T is the transpose, and $\mathbf{R}^\lambda$ is a second rank Cartesian tensor representing the coupling interaction, λ, between the vectors, such as CSA or dipole. The coupling tensor is described by a 3x3 matrix and can be decomposed into zeroth (isotropic), first (anti-symmetric), and second rank (anisotropic) components with $\mathbf{R}^{(0)} = 1/3 \, \mathrm{Tr}\{\mathbf{R}\} \, \mathbf{E}$, $\mathbf{R}^{(1)} = (\mathbf{R} - \mathbf{R}^T)/2$, and $\mathbf{R}^{(2)} = (\mathbf{R} + \mathbf{R}^T)/2 - \mathbf{R}^{(0)}$. A physical interpretation of the tensor can be obtained by writing the Hamiltonian in the principal axis system (PAS) of the second rank tensor, where the diagonal contains the principal components $d_q = R_{qq} - 1/3 \, \mathrm{Tr}\{\mathbf{R}\}$ for $q = \{x,y,z\}$ and off diagonal components of the first rank part are equal and opposite ($R_{xy} = -R_{yx}$, etc.):

$$\mathcal{H}^{PAS} = \mathbf{u}^T \left(\mathbf{R}^{(0)} + \mathbf{R}^{(1)} + \mathbf{R}^{(2)} \right) \mathbf{v}$$
$$= \tfrac{1}{3} \mathrm{Tr}\{\mathbf{C}\} \mathbf{u} \bullet \mathbf{v}$$
$$+ R_{xy}(u_x v_y - u_y v_x) + R_{xz}(u_x v_z - u_z v_x) + R_{yz}(u_y v_z - u_z v_y)$$
$$+ d_x u_x v_x + d_y u_y v_y + d_z u_z v_z \qquad (1.4)$$

While the Cartesian form provides a useful physical understanding of the nuclear spin interaction, averaging of the Hamiltonian is accomplished more easily using irreducible spherical tensors, T_{lm}, as they have relatively simple transformation properties. The components of the Cartesian angular momentum and field vectors are not themselves irreducible, although a linear combination of them can yield the appropriate first rank spherical components:

$$T_{1\pm1} = v_{\pm1} = \mp \frac{1}{\sqrt{2}} \left(v_x + i v_y \right).$$
$$T_{10} = v_0 = v_z \qquad (1.5)$$

Irreducible spherical tensors of arbitrary rank can be obtained from the direct product of lower rank tensors and the interaction between two spin-½ nuclei (or a spin-½ nucleus and the external field) will only result in tensor components of rank two or less. The Hamiltonian can therefore be written generally using spherical tensors as

$$\mathcal{H} = C^\lambda \sum_{l=0}^{2} \sum_{m=-l}^{l} (-1)^m T_{lm}^\lambda R_{l-m}^\lambda \qquad (1.6)$$

where C^λ contains the factors of proportionality required for coupling interaction, λ. While the spin dependent operators, T_{lm}, can be obtained from the lower rank vector operators, the coupling tensor, R_{lm}, can not be known beforehand. In order to form a relation between the second rank Cartesian and spherical coupling tensors, the components of $T_{lm}R_{lm}$ need to be expressed with Cartesian components. The R_{lm} components can then be obtained from a comparison of the spherical and Cartesian tensor elements and are collected in Table 1.1. In the PAS of the second rank tensor, making use of the traceless and antisymmetric properties, $d_z = -d_x - d_y$, $R_{xy} = -R_{yx}$, $R_{xz} = -R_{zx}$, $R_{yz} = -R_{zy}$, and defining an axial asymmetry parameter $\eta = (d_y - d_x)/d_z$, the nuclear spin Hamiltonian can be expressed as

$$\mathcal{H}^{PAS} = C^{\lambda} \left\{ \begin{array}{l} R_{iso}^{\lambda} T_{00}^{\lambda} \\ - R_{xz}^{\lambda} \left(T_{11}^{\lambda} + T_{1-1}^{\lambda} \right) + i \left[R_{yz}^{\lambda} \left(T_{11}^{\lambda} - T_{1-1}^{\lambda} \right) - \sqrt{2} R_{xy}^{\lambda} T_{10}^{\lambda} \right] \\ + \sqrt{\dfrac{3}{2}} d_z^{\lambda} T_{20}^{\lambda} - \dfrac{1}{2} d_z^{\lambda} \eta^{\lambda} \left(T_{22}^{\lambda} + T_{2-2}^{\lambda} \right) \end{array} \right\} \tag{1.7}$$

where

$$R_{iso}^{\lambda} = 1/3 \mathrm{Tr}\{\mathbf{R}^{\lambda}\} = \left(R_{xx}^{\lambda} + R_{yy}^{\lambda} + R_{zz}^{\lambda} \right)/3$$

$$\left| R_{zz}^{\lambda} \right| \geq \left| R_{xx}^{\lambda} \right| \geq \left| R_{yy}^{\lambda} \right| \tag{1.8}$$

and the parameters $\{C^{\lambda}, R_{iso}^{\lambda}, d_z^{\lambda}, \eta^{\lambda}\}$ are $\{\omega_I, \sigma_{iso}, \sigma_{zz}, \eta\}$ or $\{-2\gamma_I\gamma_S, 0, r^{-3}, 0\}$ for the CSA or dipolar interactions, respectively. Here, the ordering of the principal values R_{xx}, R_{yy}, and R_{zz} follows the ordering used by Spiess[81] as it ensures that either $R_{xx} \geq R_{yy} \geq R_{zz}$ or $R_{zz} \geq R_{yy} \geq R_{xx}$ which will be more convenient when dealing with shielding tensors. While it is useful to consider the Hamiltonian in the principal axis frame of the coupling interaction, the spin dependent operators take on a much simpler form when written in the laboratory frame, listed in Table 1.2, with the z-axis parallel to the magnetic field. Since the spin operators are independent of orientation, a Wigner rotation can be applied to the coupling tensor to bring the Hamiltonian to the laboratory frame:

$$\mathcal{H} = C^{\lambda} \sum_{l=0}^{2} \sum_{m=-l}^{l} (-1)^m T_{lm}^{\lambda} \sum_{k=-l}^{l} R_{lk}^{\lambda,PAS} \mathcal{D}_{k-m}^{l} \left(\alpha^{\lambda}, \beta^{\lambda}, \gamma^{\lambda} \right). \tag{1.9}$$

Now that the Hamiltonian is written in such a way that the T_{lm} and R_{lm} are orientation and time independent, averaging due to rotations of the molecule can be described through the Wigner rotation matrices alone.

The dipolar interaction between two nuclear spins is a purely second rank interaction, as is shown in Table 1.2, and therefore averages to zero under isotropic solution conditions. However, second order perturbations can contribute to relaxation of the magnetization, as will be discussed in §1.2.2. By introducing anisotropy to the solution, incomplete averaging of the dipolar interaction can result in resonance splittings, known as RDCs. These can be used to define long range structure and dynamics of the nucleic acid and will be discussed in §1.2.1. The interaction between

l	m	T_{lm} (spherical)	T_{lm} (Cartesian)	$\mathbf{u}^T \mathbf{R}^{(l)} \mathbf{v}$	R_{lm}^{PAS}
0	0	$u_0 v_0 - u_+ v_- - u_- v_+ \equiv \mathbf{u} \bullet \mathbf{v}$	$u_x v_x + u_y v_y + u_z v_z \equiv \mathbf{u} \bullet \mathbf{v}$	$R_{iso} \mathbf{u} \bullet \mathbf{v}$	R_{iso}
1	0	$\dfrac{1}{\sqrt{2}}\left(u_+ v_- - u_- v_+\right)$	$\dfrac{i}{\sqrt{2}}\left(u_x v_y - u_y v_x\right)$	$R_{xy}\left(u_x v_y - u_y v_x\right)$	$-i\sqrt{2}R_{xy}$
	± 1	$\dfrac{1}{\sqrt{2}}\left(\pm u_\pm v_0 \mp u_0 v_\pm\right)$	$\dfrac{1}{2}\left(u_z v^\pm - u^\pm v_0\right)$	$+R_{xz}\left(u_x v_z - u_z v_x\right)$ $+R_{yz}\left(u_y v_z - u_z v_y\right)$	$R_{xz} \pm i R_{yz}$
2	0	$\dfrac{1}{\sqrt{6}}\left(u_+ v_- + u_- v_+ + 2u_0 v_0\right) = \dfrac{1}{\sqrt{6}}\left(3u_0 v_0 - \mathbf{u} \bullet \mathbf{v}\right)$	$\dfrac{1}{\sqrt{6}}\left(3u_z v_z - \mathbf{u} \bullet \mathbf{v}\right)$	$d_x u_x v_x + d_y u_y v_y + d_z u_z v_z$	$\sqrt{\dfrac{3}{2}}d_z$
	± 1	$\dfrac{1}{\sqrt{2}}\left(u_\pm v_0 + u_0 v_\pm\right)$	$\dfrac{-1}{2}\left(u^\pm v_z + u_z v^\pm\right)$	$= \dfrac{1}{2}d_z\left(3u_z v_z - \mathbf{u} \bullet \mathbf{v}\right)$	0
	± 2	$u_\pm v_\pm$	$\dfrac{1}{2}u^\pm v^\pm$	$+\dfrac{1}{2}d_z\eta\left(u_y v_y - u_x v_x\right)$	$-\dfrac{1}{2}d_z\eta$

Table 1.1. Relationship between spherical and Cartesian spin and coupling operators. Here, $u^\pm = u_x \pm i\,u_y$, and $v^\pm = v_x \pm i\,v_y$, $d_q = R_{qq} - R_{iso}$ with $q = \{x,y,z\}$, $R_{xy} = -R_{yx}$, $R_{xz} = -R_{zx}$, $R_{yz} = -R_{zy}$, $\eta = (d_y - d_x)/d_z$.

l	m	T_{lm} (CSA)	T_{lm} (Dipolar)
0	0	$I_0 B_0$	0
1	0	0	0
	± 1	$\dfrac{1}{\sqrt{2}}\left(\pm I_\pm B_0\right)$	0
2	0	$\sqrt{\dfrac{2}{3}}I_0 B_0$	$\dfrac{1}{\sqrt{6}}\left(3I_0 S_0 - \mathbf{I} \bullet \mathbf{S}\right)$
	± 1	$\dfrac{1}{\sqrt{2}}I_\pm B_0$	$\dfrac{1}{\sqrt{2}}\left(I_\pm S_0 + I_0 S_\pm\right)$
	± 2	0	$I_\pm S_\pm$

Table 1.2. Explicit expressions of the CSA and dipolar spin-dependent operators in the laboratory frame.

nuclei also gives rise to a through space transfer of magnetization known as cross-relaxation. Proton-proton cross-relaxation, often referred to as the nuclear Overhausser effect (NOE), is the basis of most structure determination techniques by NMR. The heteronuclear NOE (hetNOE), cross-relaxation between two different nuclei such as proton to carbon, is an important additional parameter for the interpretation of relaxation in terms of dynamic parameters (see §1.2.3). Longitudinal and transverse auto relaxation is often the dominant relaxation mechanism for X-H spin systems, where X can be ^{13}C or ^{15}N, and will be discussed in detail in §1.2.2.

The description of nuclear shielding arises from the interaction between a spin ½ nucleus and the external magnetic field and is therefore conveniently represented as a second rank tensor.

$$\boldsymbol{\sigma} = \begin{bmatrix} \sigma_{XX} & \sigma_{XY} & \sigma_{XZ} \\ \sigma_{YX} & \sigma_{YY} & \sigma_{YZ} \\ \sigma_{ZX} & \sigma_{ZY} & \sigma_{ZZ} \end{bmatrix} = \mathfrak{R}^{-1} \begin{bmatrix} \sigma_{11} & \sigma_{12} & \sigma_{13} \\ \sigma_{21} & \sigma_{22} & \sigma_{23} \\ \sigma_{31} & \sigma_{32} & \sigma_{33} \end{bmatrix} \mathfrak{R} = \mathfrak{R}^{-1} \boldsymbol{\sigma}^{PAS} \mathfrak{R} \tag{1.10}$$

Unlike the dipolar interaction, chemical shielding is real and nonsymmetric, meaning that the nine parameters can take any arbitrary value. As mentioned above, rotating into the PAS of the second rank anisotropic part, it can be represented as a sum of its irreducible tensor components of rank zero, one, and two:

$$\boldsymbol{\sigma}^{PAS} = \boldsymbol{\sigma}^{(0)} + \boldsymbol{\sigma}^{(1)} + \boldsymbol{\sigma}^{(2)}$$

$$= \sigma_{iso} \begin{bmatrix} 1 & 0 & 0 \\ 0 & 1 & 0 \\ 0 & 0 & 1 \end{bmatrix} + \begin{bmatrix} 0 & \sigma_{12} & \sigma_{13} \\ -\sigma_{12} & 0 & \sigma_{23} \\ -\sigma_{13} & -\sigma_{23} & 0 \end{bmatrix} + \sigma_{zz} \begin{bmatrix} -\dfrac{1+\eta}{2} & 0 & 0 \\ 0 & -\dfrac{1-\eta}{2} & 0 \\ 0 & 0 & 1 \end{bmatrix}$$

$$\tag{1.11}$$

where the parameters σ_{iso} and the asymmetry parameter, η, are given by

$$\sigma_{iso} = (\sigma_{11} + \sigma_{22} + \sigma_{33})/3$$

$$\sigma_{33} \geq \sigma_{22} \geq \sigma_{11}$$

$$\eta = \frac{\sigma_{yy} - \sigma_{xx}}{\sigma_{zz}} \quad , \quad 0 \leq \eta \leq 1$$

$$|\sigma_{zz}| \geq |\sigma_{xx}| \geq |\sigma_{yy}|$$

(1.12)

It is worth noting that the choice of indices is intentional in an effort to easily differentiate between the arbitrary shielding tensor (capital subscripts), the shielding tensor in its PAS (Arabic numeral subscripts), and the anisotropic tensor (lowercase subscripts) which may or may not be in its PAS.

A frequently overlooked component of the chemical shielding tensor is the first rank, antisymmetric part. Antisymmetry primarily is found in nuclei with low point symmetry and has only been experimentally observed in highly ring-strained small molecules.[84,85] A handful of theoretical studies have been done on such molecules and show that the antisymmetry can be significant, although on the order of 5 to 25 ppm in magnitude for more common geometries. In general, antisymmetry is most likely to be found at nuclei that are known to have considerable axial asymmetry, η close to 1, although this not necessarily true as antisymmetry and axial asymmetry are not directly related. As will be discussed in §1.2.1, only spin operators of the form T_{10} contribute to frequency shifts, therefore the antisymmetric component rigorously does not give rise to shifts under solution conditions. The antisymmetric component of chemical shielding can, however, affect solid-state spectra, albeit under rare circumstances. It can be shown in a straight forward manner that the result of the shielding tensor is to induce an additional magnetic field on a nucleus:

$$\omega = -\gamma \, (1-\sigma) \, B_0$$

$$\omega = -\gamma \, B_0 + \gamma \, \sigma \, B_0$$

$$\omega = -\gamma \, B_0 + \gamma \, B_{ind}.$$

(1.13)

For antisymmetric shielding, which has only zero values along its diagonal, the result is to induce a magnetic field, $\sigma_{anti} \, B_0$, that is perpendicular to external field. The effective

Parameter	Name	Definition		Note
		Shielding Tensor	CSA Tensor	
δ	Largest Principle Value	$\sigma_{11} - \sigma_{iso}, \ |\sigma_{11}|>|\sigma_{33}|$ $\sigma_{33} - \sigma_{iso}, \ |\sigma_{11}|<|\sigma_{33}|$	σ_{zz}	Not to be confused with chemical shift
CSA, $\Delta\sigma$	Chemical Shielding Anisotropy	$\sigma_{11} - \dfrac{\sigma_{22}+\sigma_{33}}{2}, |\sigma_{11}|>|\sigma_{33}|$ $\sigma_{33} - \dfrac{\sigma_{22}+\sigma_{11}}{2}, |\sigma_{11}|<|\sigma_{33}|$ $\dfrac{3}{2}\delta$	$\sigma_{zz} - \dfrac{\sigma_{xx}+\sigma_{yy}}{2}$ $\dfrac{3}{2}\sigma_{zz}$	Axially symmetric tensor with $\eta = 0$
CSA$_a$, $\Delta\sigma_{eff}$	Chemical Shielding Anisotropy	$\Delta\sigma\left(1+\eta^2/3\right)^{1/2}$ $\left(\sigma_{11}^2 + \sigma_{22}^2 + \sigma_{33}^2 - \sigma_{11}\sigma_{22} - \sigma_{11}\sigma_{33} - \sigma_{22}\sigma_{33}\right)^{1/2}$	$\Delta\sigma\left(1+\eta^2/3\right)^{1/2}$ $\left[\dfrac{3}{2}\left(\sigma_{xx}^2 + \sigma_{yy}^2 + \sigma_{zz}^2\right)\right]^{1/2}$	Axially asymmetric tensor with $\eta \neq 0$ $|CSA_a| = \Delta\sigma_{eff}$
η	Axially Asymmetry	$\dfrac{\sigma_{22}-\sigma_{33}}{\sigma_{11}-\sigma_{iso}}, |\sigma_{11}|>|\sigma_{33}|$ $\dfrac{\sigma_{22}-\sigma_{11}}{\sigma_{33}-\sigma_{iso}}, |\sigma_{11}|<|\sigma_{33}|$	$\dfrac{\sigma_{yy}-\sigma_{xx}}{\sigma_{zz}}$	Range: 0 to 1 0: symmetric ($\sigma_{xx}=\sigma_{yy}$) 1: asymmetric ($\sigma_{xx,11} = -\sigma_{zz,33}$)
Ω	Span	$\sigma_{33} - \sigma_{11}$	$|\sigma_{zz} - \sigma_{xx}|$	
κ	Skew	$\dfrac{-3\left(\sigma_{22}-\sigma_{iso}\right)}{\Omega}$	$\dfrac{-3\sigma_{yy}}{\Omega}$	Range: -1 to 1 -1: symmetric about least shielded axis, σ_{11} 0: asymmetric ($\sigma_{xx,11} = -\sigma_{zz,33}$) 1: symmetrix about most shielded axis, σ_{33}

Table 1.3. Parameterization of the chemical shielding and CSA tensors.

field will therefore have a magnitude $\left(B_0^2 + B_{ind}^2\right)^{1/2}$ and result in a chemical shift change in the ^{13}C dimension of 0.75 Hz at 14.1 T and an antisymmetry magnitude of 100 ppm. Unless the antisymmetry is extremely large, it is all but undetectable in NMR spectra. This is not necessarily the case for true for spin relaxation and will be discussed further in §1.2.2.

The second rank part of the shielding tensor is (mathematically) symmetric and traceless and is often referred to as the chemical shielding anisotropy (CSA) tensor, although confusion between it and the full nonsymmetric shielding tensor is common. A number of parameterizations appear in the literature to describe the magnitude and axial symmetry of the CSA tensor principal values. The most common parameters are listed in Table 1.3. In tensor form the parameterization of chemical shift is very similar to shielding with the exceptions that $\delta_{11} \geq \delta_{22} \geq \delta_{33}$ and that the principal components of the chemical <u>shift</u> anisotropy tensor are only opposite in sign of the chemical <u>shielding</u> anisotropy tensor principal components, although both are commonly referred to as the CSA tensor. Often, the CSA tensor is assumed to be axially symmetric since this greatly simplifies the analysis of relaxation data and the significance of the interaction is usually small compared to the dipolar interaction. However, at high fields and for carbonyl and nucleobase carbons, the CSA can become the dominant contribution to relaxation and therefore axial asymmetry must be taken into account. In addition, the axial asymmetry is important for the analysis of RCSA measurements as differences between σ_{xx} and σ_{yy} can have a significant effect on the orientational dependence of the measurements. A variety of discrepancies in literature can appear. For instance, when axial symmetry is assumed, the largest principal value is not chosen when calculating $\Delta\sigma$ and η, or $\Delta\sigma$ are reported along with η. The latter is particularly prevalent and inappropriate for the description of axially asymmetric tensors since the parameter $\Delta\sigma$ reduces to $(3/2)\ \delta$. If either σ_{11} or σ_{33} are consistently used as the principal axis, then η can range from 0 to 3. The parameter CSA_a, which can be more directly related to the analysis of relaxation data of isotropically tumbling molecules, will in general be up to $(4/3)^{1/2}$ larger the $\Delta\sigma$ (or

twice as large if the wrong principle value is chosen). The span and skew parameters, Ω and κ, have a slightly simpler form than CSA$_a$ and η, but are not easily incorporated into the analysis of relaxation data and are more commonly found in solid state NMR literature. In order to be accurate and consistent with literature, only the parameters CSA$_a$ and η or the individual principal values themselves will be used throughout the rest of this text.

1.2.1 Residual Anisotropic Interactions

Weak fist order perturbations of the Zeeman Hamiltonian using the nuclear spin Hamiltonian in Equation 1.9 results in the resonance frequencies observed in NMR spectra. As a consequence, only components of the spin Hamiltonian that commute with the Zeeman Hamiltonian are preserved. The resulting simplified Hamiltonian therefore only contains terms where the spin operator is of the form T_{10}^{λ}:

$$
\begin{aligned}
\mathcal{H} &= C^{\lambda} \sum_{l=0}^{2} T_{10}^{\lambda} \sum_{k=-1}^{1} R_{lk}^{\lambda,PAS} \mathcal{D}_{k0}^{l}\left(\alpha^{\lambda},\beta^{\lambda},0\right) \\
&= C^{\lambda}\left[T_{00}^{\lambda} R_{00}^{\lambda,PAS} + T_{20}^{\lambda} \sum_{k=-2}^{2} R_{2k}^{\lambda,PAS} \mathcal{D}_{k0}^{2}\left(\alpha^{\lambda},\beta^{\lambda},0\right)\right] \\
&= C^{\lambda}\left[\begin{array}{l} T_{00}^{\lambda} R_{iso}^{\lambda} \\ + T_{20}^{\lambda}\sqrt{\dfrac{3}{2}}d_z^{\lambda}\left[\mathcal{D}_{00}^{2}\left(0,\beta^{\lambda},0\right) - \sqrt{\dfrac{1}{6}}\eta^{\lambda}\left(\mathcal{D}_{-20}^{2}\left(\alpha^{\lambda},\beta^{\lambda},0\right) + \mathcal{D}_{20}^{2}\left(\alpha^{\lambda},\beta^{\lambda},0\right)\right)\right] \end{array} \right]
\end{aligned}
\tag{1.14}
$$

In addition, since only the Wigner elements $\mathcal{D}_{k0}^{l}$ are retained, the Euler angle γ, which represents rotations about the z-axis of the laboratory frame, is unnecessary and therefore arbitrarily set to 0.

Since the isotropic component is invariant upon rotation, only the second rank terms of the nuclear spin Hamiltonian must be considered when describing RDCs and RCSAs. As stated above, the averaging of the Hamiltonian under solution conditions is easily accomplished through averaging of the orientationally dependent Wigner matrices

$$\mathcal{H} = C^\lambda \sum_{m=-2}^{2} (-1)^m T_{2m}^\lambda \sum_{k=-2}^{2} R_{2k}^{\lambda,PAS} \left\langle \mathcal{D}_{k-m}^2 \left(\alpha_{P\to L}^\lambda, \beta_{P\to L}^\lambda, \gamma_{P\to L}^\lambda \right) \right\rangle \tag{1.14}$$

which can be generally described by

$$\left\langle \mathcal{D}_{mn}^1 (\alpha,\beta,\gamma) \right\rangle = \int \mathcal{D}_{mn}^1 (\alpha,\beta,\gamma) \, p(\alpha,\beta,\gamma) \sin(\beta) \, d\alpha \, d\beta \, d\gamma$$

where $p(\alpha,\beta,\gamma)$ is the orientation probability distribution function that describes the orientation of the magnetic field relative to a fixed molecular frame. Under typical solution conditions, the orientation of molecules is isotropic, $p(\alpha,\beta,\gamma) = 1/(8\pi^2)$ and the average Wigner rotations equal zero, leaving only interactions with the $T_{00}^\lambda R_{iso}^\lambda$ terms, such as chemical shifts and scalar couplings $(C^\lambda T_{00}^\lambda R_{iso}^\lambda = \gamma B_0 I_Z \sigma_{iso}$ or $2\pi J_{iso} I_Z S_Z$, respectively). In general the orientation of the principal axis system with respect to the magnetic field will not be known (ie. $\alpha_{P\text{->}L}$, $\beta_{P\text{->}L}$, $\gamma_{P\text{-}L}$), so it is useful to relate it first to a molecule centered alignment frame (ie. $\alpha_{P\text{->}A}$, $\beta_{P\text{->}A}$, $\gamma_{P\text{-}A}$) and then represent the average over the molecular orientations as a single order parameter, S_j:

$$
\begin{aligned}
\mathcal{H} &= C^\lambda T_{20}^\lambda \sum_{j=-2}^{2} \sum_{k=-2}^{2} R_{2k}^{\lambda,PAS} \mathcal{D}_{kj}^2 \left(\alpha_{P\to A}^\lambda, \beta_{P\to A}^\lambda, \gamma_{P\to A}^\lambda \right) \left\langle \mathcal{D}_{j0}^2 \left(\alpha_{A\to L}^\lambda, \beta_{A\to L}^\lambda, 0 \right) \right\rangle \\
&= C^\lambda T_{20}^\lambda \sum_{j=-2}^{2} \sum_{k=-2}^{2} R_{2k}^{\lambda,PAS} \mathcal{D}_{kj}^2 \left(\alpha_{P\to A}^\lambda, \beta_{P\to A}^\lambda, \gamma_{P\to A}^\lambda \right) S_j^* \\
&= C^\lambda T_{20}^\lambda \sum_{j=-2}^{2} R_{2j}^\lambda S_j^*
\end{aligned}
\tag{1.15}
$$

The set of the spherical order parameters $S_j = (-1)^j S_{-j}^*$ are related to the real, traceless, and symmetric Saupe irreducible order parameters, S_{ij}:

$$
\begin{aligned}
S_0 &= S_{zz} \\
S_{\pm 1} &= \pm\sqrt{2/3} \left(S_{xz} \mp i S_{yz} \right) \\
S_{\pm 2} &= \sqrt{1/6} \left(S_{xx} - S_{yy} \right) \mp i\sqrt{2/3} S_{xy}
\end{aligned}
\tag{1.16}
$$

Combining Equations 1.15 and 1.16, we arrive at the final, general expression for the Hamiltonian under anisotropic conditions in Cartesian form is

$$\mathcal{H} = C^\lambda T_{20}^\lambda \sqrt{\frac{2}{3}} \sum_{i=\{x,y,z\}} \sum_{j=\{x,y,z\}} R_{ij}^\lambda S_{ij}$$

$$= C^\lambda T_{20}^\lambda \sqrt{\frac{3}{2}} d_z^\lambda S_{zz} \left\{ \begin{array}{l} \dfrac{3\cos^2\beta - 1}{2} + \dfrac{\eta^S}{2}\sin^2\beta\cos 2\gamma \\[2mm] -\dfrac{\eta^\lambda}{2}\left[\cos 2\alpha\sin^2\beta + \dfrac{\eta^S}{6}\left(\begin{array}{l} \cos 2\alpha(3+\cos 2\beta)\cos 2\gamma - \\ 4\cos\beta\sin 2\alpha\sin 2\gamma \end{array} \right) \right] \end{array} \right\} \qquad (1.17)$$

where $\eta^S = (S_{xx} - S_{yy})/S_{zz}$ and $S_{zz} \geq S_{yy} \geq S_{xx}$. Substituting in the parameters for C^λ, d_z^λ, η^λ, and incorporating the correct units, the dipolar coupling equation collapses to the familiar form

$$\begin{aligned} \mathcal{H} &= \pi D_{IS}(3I_z S_z - \mathbf{I} \bullet \mathbf{S}) \\ &= 2\pi D_{IS} I_z S_z, \text{ if } 2\pi D_{IS} << |\omega_I - \omega_S| \\ D_{IS} &= -\frac{\mu_0 h \gamma_I \gamma_S}{8\pi^3 r_{IS}^3} S_{zz} \left\{ \frac{3\cos^2\beta - 1}{2} + \frac{\eta^S}{2}\sin^2\beta\cos 2\gamma \right\} \end{aligned} \qquad (1.18)$$

Similarly, the result for chemical shielding is

$$\begin{aligned} \mathcal{H} &= -\gamma_I(1 - \sigma_{iso} - \sigma_{ani})I_z B_z \\ \sigma_{ani} &= \frac{2}{3} \sum_{i=\{x,y,z\}} \sum_{j=\{x,y,z\}} \sigma_{ij} S_{ij} \end{aligned} \qquad (1.19)$$

1.2.2 Spin Relaxation

During an NMR experiment, equilibrium magnetization is perturbed to produce transitions between energy states. Using density matrices, the populations of these energy levels fall on the diagonal whereas transitions between states are represented by the off-diagonal elements. Over time, the magnetization will return to thermal equilibrium and it is this fundamental process that is referred to as nuclear magnetic, or spin, relaxation. In other spectroscopies, this process can often be described by spontaneous or stimulated emission. The probability, W, of a transition from a high to low energy state is given by[80,86]

$$W = \frac{\mu_0 \gamma^2 \hbar \omega_0^3}{12\pi^2 c^3} \qquad (1.20)$$

where c is the speed of light. For a proton spin with a Larmor frequency as large as one GHz (23.5 Tesla), this probability amounts to only 4.6 x 10^{-21} s^{-1} and is therefore an inadequate mechanism for spin relaxation. Alternatively, fluctuating magnetic fields caused by a coupling between the nucleus and its surrounding environment, often called the lattice, can have a significant effect. Nonadiabatic energy processes, which exchange energy with the surroundings, result from fluctuations of local fields in the transverse plane and lead to relaxation of both diagonal and off-diagonal components of the density matrix. However, changes in local fields parallel to the static magnetic field do not require any exchange of magnetization. These adiabatic processes do not perturb the populations of the energy states and only off-diagonal components of the density matrix are reduced to zero. Consequently relaxation of magnetization parallel to the magnetic field is only caused by nonadiabatic processes, giving it the name of spin-lattice relaxation, whereas both adiabatic and nonadiabatic processes can cause relaxation of the transverse magnetization.

Like residual anisotropic interactions, spin relaxation is a semi-classical problem in which a quantum mechanical description is given to the spin dependent parts of the parts of the Hamiltonian and the remaining, orientationally dependent parts are treated classically. Any description of relaxation begins with the Liouville equation of motion of the density matrix

$$\frac{d\varrho(t)}{dt} = -i[\mathcal{H}_0 + \mathcal{H}_1(t), \varrho(t)] \qquad (1.21)$$

where square brackets represent the commutator relationship. Transformation into the interaction frame removes the dependence on $\mathcal{H}_0$ while keeping the time dependence associated with $\mathcal{H}_1$. Any arbitrary operator, X, can be transformed this way by

$$X^F = e^{i\mathcal{H}_0 t} X e^{-i\mathcal{H}_0 t} \qquad (1.22)$$

and the Liouville equation becomes

$$\frac{d\varrho^F(t)}{dt} = -i\left[\mathcal{H}_1^F(t), \varrho^F(t)\right] = -i\,\mathcal{L}_1^F(t)\varrho^F(t). \tag{1.23}$$

Use of the Liouvillian, $\mathcal{L}(t) = [\mathcal{H}(t), \ ]$, or commutation superoperator, helps to illustrate the solution to the equation of motion. Integration by consecutive approximations up to second order results in

$$\varrho^F(t) = \varrho^F(0) - i\int_0^t \mathcal{L}_1^F(t')\varrho^F(0)dt' - \int_0^t \mathcal{L}_1^F(t')dt' \int_0^{t'} \mathcal{L}_1^F(t'')\varrho^F(0)dt'' \tag{1.24}$$

after which, taking the derivative gives

$$\begin{aligned} \frac{d\varrho^F(t)}{dt} &= -i\,\mathcal{L}_1^F(t)\varrho^F(0) - \int_0^t \mathcal{L}_1^F(t)\mathcal{L}_1^F(t')\varrho^F(0)dt' \\ &= -i\left[\mathcal{H}_1^F(t), \varrho^F(0)\right] - \int_0^t \left[\mathcal{H}_1^F(t), \left[\mathcal{H}_1^F(t'), \varrho^F(0)\right]\right]dt' \\ &= -i\left\langle\left[\mathcal{H}_1^F(t), \varrho^F(0)\right]\right\rangle - \int_0^t \left\langle\left[\mathcal{H}_1^F(t), \left[\mathcal{H}_1^F(t'), \varrho^F(0)\right]\right]\right\rangle dt' \\ \frac{d\varrho^F(t)}{dt} &= -\int_0^\infty \left\langle\left[\mathcal{H}_1^F(t), \left[\mathcal{H}_1^F(t-\tau), \varrho^F(t)\right]\right]\right\rangle d\tau \end{aligned} \tag{1.25}$$

Observation of a signal is found by taking the average of the density matrix, indicated by angle brackets in line 3 of Equation 1.25. Since the average of the $\mathcal{H}_1(t)$ is zero, the first term is eliminated. Several assumptions are made to arrive at the master equation of motion in the fourth line, and the new variable $\tau = t - t'$ is introduced. First, the evolution of the density operator is assumed to be slow, allowing $\varrho(0)$ to be written as $\varrho(t)$. Second, one can extend the integration to positive infinity, as contributions to the integral for times $t \gg \tau_c$ are insignificant. Finally, the higher order expansion terms in Equation 1.24 are negligible. In general, this master equation is valid for weak perturbations, $\mathcal{H}_1$, such that $\sqrt{\mathcal{H}_1^2\tau_c^2} \ll 1$, where τ_c is the correlation time of the function.[80] For isotropic solutions, this is obtained from modeling the global rotational diffusion of the molecule and is typically on the order of several to tens of nanoseconds. These assumptions are discussed in detail by Abragam and in other texts.[79-81] One shortfall of the semi-classical treatment is its inability to describe the equilibrium state of the system. For this reason, $\varrho^F(t)$ is often replaced with $\varrho^F(t) - \varrho_0$, where ϱ_0 is the equilibrium density operator.

The operator form of the Hamiltonian in Equation 1.6 can now be incorporated into the master equation by giving time dependence to the spatial operators, R_{lm}. In principal,

the time dependence of the Hamiltonian can be introduced through either the spin dependent, T_{lm}, or spatial, R_{lm}, components. Since the spin dependent components are invariant upon rotation, only the time dependence of the spatial components will be considered here. For other relaxation mechanisms, such as spin rotation and scalar relaxation of the second kind, it can be more appropriate to apply the time dependence on the spin operators and is discussed in detail elsewhere.[81]

Relating the master equation back to the laboratory frame requires an understanding of the transformation properties of $\mathcal{H}_1(t)$. Following equation 1.22, the spin operators can be rewritten

$$T_{lm}^F = e^{i\mathcal{H}_0 t}T_{lm}e^{-i\mathcal{H}_0 t} = \sum_p T_{lm}^p e^{i\omega_m^p t} \tag{1.26}$$

where T_{lm}^p satisfies the relationship $[\mathcal{H}_0, T_{lm}^p] = \omega_m^p T_{lm}^p$ and $\omega_{-m}^p = -\omega_m^p$. The index p is used to distinguish spin operators of the same order, m, but with different eigenfrequencies, ω, such as for dipolar interactions between unlike spins. The resulting interaction frame Hamiltonian becomes

$$\mathcal{H}_1^F(t) = C^\lambda \sum_{l=1}^2 \sum_{m=-l}^1 (-1)^m T_{lm}^\lambda R_{l-m}^\lambda(t) = C^\lambda \sum_{l=1}^2 \sum_{m=-l}^1 \sum_p (-1)^m T_{lm}^p R_{l-m}^\lambda(t)e^{i\omega_m^p t} \tag{1.27}$$

and substituting this into the master equation gives us

$$\frac{d\varrho^F(t)}{dt} = -C^2 \sum_{l=1}^2 \sum_{m,m',p,p'} (-1)^{m+m'} e^{i(\omega_m^p + \omega_{m'}^{p'})t} \left[T_{lm'}^{p'}, \left[T_{lm}^p, \varrho^F(t) - \varrho_0 \right] \right]$$
$$\cdot \int_0^\infty \left\langle R_{l-m'}^\lambda(t) R_{l-m}^\lambda(t-\tau)e^{-i\omega_m^p t} \right\rangle d\tau \tag{1.28}$$

Two simplifications can be made immediately. First, the random processes of R_{lm} and $R_{lm'}$ are assumed to be independent so that terms with $m' \neq -m$ will be eliminated from the ensemble average. Second, nonsecular terms with $\left| \omega_m^p + \omega_{m'}^{p'} \right| \gg 0$ do not contribute significantly to the density matrix as the exponential factors oscillate rapidly and average to zero before relaxation can occur. This leaves only secular terms where p=p', assuming there are no degenerate eigenfrequencies, and results in

$$\frac{d\varrho^F(t)}{dt} = -C^2 \sum_{l=1}^{2} \sum_{m=-l}^{1} \sum_{p} \left[T_{lm}^P, \left[T_{l-m}^P, \varrho^F(t) - \varrho_0\right]\right]\int_0^\infty \left\langle R_{l-m}^\lambda(t)R_{lm}^\lambda(t-\tau)e^{-i\omega_m^P t}\right\rangle d\tau \qquad (1.29)$$

While the spin operator for the dipolar coupling arises from the combination of two nuclear spins, the chemical shielding is the combination of a nuclear spin and the components of the static magnetic field. For this reason, the two contributions to relaxation will need to be treated separately. The new T_{lm}^P and ω_m^P elements are collected in Table 1.4 for the dipolar and CSA interactions. In addition, the commutator properties of like spins (being of the same nucleus type) will have degenerate eigenfrequencies, leading to additional terms in Equation 1.29 and therefore different relaxation rates. For simplicity, only the case of unlike spins will be discussed here as the dominant relaxation mechanism of heteronuclei in biomolecules is often between the nucleus and its attached proton. These expressions can also be used for relaxation rates arising from several coupled carbon nuclei as long as their chemical shift difference is sufficiently large and the nuclei can be excited selectively.

l	m	p	T_{lm}^P (Dipolar)	T_{lm}^P (CSA)	ω_m^P
1	0	0	0	0	0
	± 1	0	0	$\pm\dfrac{1}{\sqrt{2}}B_0 S_\pm$	ω_S
2	0	0	$\sqrt{\dfrac{2}{3}}I_z S_z$	$\sqrt{\dfrac{2}{3}}B_0 S_z$	0
		-1	$\dfrac{1}{4}\sqrt{\dfrac{2}{3}}I_- S_+$	0	$\omega_S - \omega_I$
		1	$\dfrac{1}{4}\sqrt{\dfrac{2}{3}}I_+ S_-$	0	$\omega_I - \omega_S$
	± 1	0	$\mp\dfrac{1}{2}I_z S_\pm$	$\mp\dfrac{1}{2}B_0 S_\pm$	ω_S
		1	$\mp\dfrac{1}{2}I_\pm S_z$	0	ω_I
	± 2	0	$\dfrac{1}{2}I_\pm S_\pm$	0	$\omega_I + \omega_S$

Table 1.4. Expressions of the CSA and dipolar spin-dependent operators and eigenfrequencies.

The average spatial terms $\langle R_{1-m}(t)R_{1m}(t-\tau)\rangle$ are real, even-valued correlation functions describing the fluctuation of the nuclear interaction. These autocorrelation functions and their half-sided Fourier transforms, $f_{lm}(\tau)$ and $g_{lm}(\omega)$, respectively, are defined as:

$$f_{lm}(\tau) \equiv (-1)^{l+m} \langle R_{1-m}(t)R_{1m}(t-\tau)\rangle$$
$$g_{lm}(\tau) \equiv \int_0^\infty f_{lm}(\tau)e^{i\omega\tau}d\tau \qquad (1.30)$$

The imaginary part of the Fourier transform is odd with respect to ω and results in second order frequency shifts of the resonances called dynamic frequency shifts. These ultimately have the same form as the isotropic shifts and do not contribute to relaxation and can be safely neglected. The real part is symmetric with respect to ω, therefore $\omega_{-m}^P = -\omega_m^P = \omega_m^P$ and the simplification $\text{Re}[\,g_{lm}(\tau)\,] = g_l(\tau)$ can be made.

Any observable quantity, such as a relaxation rate, can be obtained by calculating the expectation value of the spin operator of interest.

$$\langle Q \rangle^F(t) = \text{Tr}[Q\varrho^F(t)]$$
$$\frac{d}{dt}\langle Q \rangle^F(t) = -C^2 \sum_{l=1}^{2} \sum_{m=-l}^{1} \sum_p (-1)^m g_{lm}(\omega)\left[T_{lm}^P, \left[T_{l-m}^P, Q^F(t) - Q_0\right]\right] \qquad (1.31)$$

For longitudinal dipolar relaxation of a two spin system, neglecting cross-correlation between opposing relaxation mechanisms,

$$\frac{d}{dt}\langle S_0 \rangle(t) = -\frac{C^2}{4}\left\{ \begin{array}{l} \left[2g_2(\omega_I + \omega_S) + g_2(\omega_S) + \dfrac{1}{3}g_2(\omega_S - \omega_I)\right]\langle S_0 \rangle \\[2mm] + \left[2g_2(\omega_I + \omega_S) - \dfrac{1}{3}g_2(\omega_S - \omega_I)\right]\langle I_0 \rangle \end{array} \right\} \qquad (1.32)$$

Note the second term depends on the magnetization of the second spin and is the source of heteronuclear cross-relaxation (NOE). By appropriately controlling the equilibrium magnetization of the two spins, the longitudinal auto- or cross-relaxation rates can be determined independently. Transverse dipolar relaxation can similarly be written

$$\frac{d}{dt}\langle S_\pm \rangle(t) = -\frac{C^2}{8}\left\{\left[2g_2(\omega_I + \omega_S) + g_2(\omega_S) + 2g_2(\omega_I) + \frac{1}{3}g_2(\omega_S - \omega_I) + \frac{4}{3}g_2(0)\right]\langle S_0\rangle\right\}$$

(1.33)

Cross-relaxation between I and S spins does not occur for transverse relaxation due to the secular approximation. The CSA contribution to longitudinal relaxation is

$$\frac{d}{dt}\langle S_0\rangle(t) = -C^2\left\{[g_1(\omega_S) + g_2(\omega_S)]\langle S_0\rangle\right\}$$

(1.34)

$$\frac{d}{dt}\langle S_\pm\rangle(t) = -\frac{C^2}{2}\left\{[g_1(\omega_S) + g_2(\omega_S) + g_2(0)]\langle S_0\rangle\right\}$$

(1.35)

Since chemical shielding is in general a nonsymmetric interaction, first rank terms, $g_1(\omega)$, can also result in relaxation.

Before the general equations for longitudinal and transverse relaxation can be used to calculate relaxation rates, the correlation functions and their Fourier transforms need to be known. The origin of most of the fluctuating magnetic fields in solution is the result of the overall tumbling of the molecule. Globular proteins can often be nearly spherical, resulting in simple expressions for rotational diffusion. However, the elongated structure of nucleic acids requires a thorough description of anisotropic rotational diffusion. This is traditionally accomplished through use of Debye's diffusion model to describe hindered molecular rotations in liquids.[87] A full discussion of the derivation is given elsewhere[81,88-91] and only the results of the derivation will be given here. The elements of R_{lm} can be represented in the same way as for residual anisotropic interactions, Table 1.1, only in the principal axis system for diffusion instead of alignment. The correlation function becomes

$$f_{lm}(\tau) = \sum_{m'=-l}^{l}\sum_{m''=-l}^{l}R_{lm'}^{PAS}R_{lm''}^{PAS*}\left\langle \mathcal{D}_{m'm}^{(l)}(t)\mathcal{D}_{m''m}^{(l)*}(t+\tau)\right\rangle$$

(1.36)

where $R_{lm}^* = (-1)^{l+m}R_{l-m}$. The average Wigner functions can be calculated with the aide of a Green's function to derive analytical expressions for $f_{lm}(\tau)$ and their Fourier transforms, $g_{lm}(\omega)$, for a completely asymmetric molecule.

$$f_{lm}(\tau) = \sum_{k=-l}^{l} c_{lk} e^{-\tau/\tau_{lk}}$$

$$g_1(\omega) = \sum_{k=-l}^{l} \frac{c_{lk}\tau_{lk}}{1+\omega^2\tau_{lk}^2}$$

(1.37)

The correlation times and coefficients are collected in Table 1.5. Simplification of these expressions occurs for a number of cases:

1. All antisymmetric contributions are eliminated due to symmetry or are negligible.

2. The diffusion tensor is a) axially symmetric, $D_r = 0$, $R = 1$, or b) isotropic, $D_a = 0$

3. The coupling tensor is axially symmetric, $D_r = 0$ (ie. dipolar)

4. Symmetry of the molecule adds degeneracy to one or more of the euler angles.

5. Extreme motional narrowing, $\omega^2\tau_{lk}^2 \ll 1$

Cases 4 and 5 are only relevant for small molecules. The assumption of symmetric CSA tensors is often used in the analysis of amide resonances in proteins. However, the nucleobase carbons are known to have highly asymmetric CSAs and this assumption is not valid for the study of carbon relaxation in RNA and DNA. Fortunately, the elongated nature of nucleic acids requires only an axially symmetric description of diffusion (case 2a).

In addition to overall rotational motion, the nuclear interactions can be influenced by internal motions. It was recognized in the first studies of large nucleic acids that the ability to observe signal was indicative of significant internal mobility since the expected transverse relaxation times for such large systems should be well over 100 Hz. Providing a detailed picture of these motions, unfortunately, is not a realistic possibility given the limited number of measurable experimental parameters. Fundamentally, recording an infinite number of relaxation experiments at different field strengths would allow one to map out the spectral density, and therefore the correlation function, that gives rise to the particular motion. However, it would still be difficult to form a complete picture as the correlation function and nuclear interactions are not necessarily sensitive to all motions. For these reasons, the best approach to adopt is one that can describe motions generally

l	k	τ_{lk}^{-1}	c_{lk}
1	-1	$2\,D_s + D_a\,(\tfrac{1}{3} + D_r)$	$\dfrac{2}{3}\left\{- R_{xy}^{\lambda}\sin\beta\cos\gamma - R_{xz}^{\lambda}(\cos\alpha\sin\gamma + \sin\alpha\cos\beta\cos\gamma) + R_{yz}^{\lambda}(-\sin\alpha\sin\gamma + \cos\alpha\cos\beta\cos\gamma)\right\}^2$
	0	$2\,D_s + D_a$	$\dfrac{2}{3}\left\{R_{xy}^{\lambda}\cos\beta - R_{xz}^{\lambda}\sin\alpha\sin\beta + R_{yz}^{\lambda}\cos\alpha\sin\beta\right\}^2$
	1	$2\,D_s + D_a\,(\tfrac{1}{3} - D_r)$	$\dfrac{2}{3}\left\{- R_{xy}^{\lambda}\sin\beta\sin\gamma + R_{xz}^{\lambda}(\cos\alpha\cos\gamma - \sin\alpha\cos\beta\sin\gamma) + R_{yz}^{\lambda}(\sin\alpha\cos\gamma + \cos\alpha\cos\beta\sin\gamma)\right\}^2$
2	-2	$6\,D_s + 2\,D_a$	$\dfrac{3d_{z,\lambda}^2}{10}\dfrac{1}{12}\left\{3\sin^2\beta\sin2\gamma - \eta_\lambda\left[\cos2\alpha\sin2\gamma(\cos^2\beta+1) + 2\sin2\alpha\cos2\gamma\cos\beta\right]\right\}^2$
	-1	$6\,D_s - D_a\,(1 - 3\,D_r)$	$\dfrac{3d_{z,\lambda}^2}{10}\dfrac{1}{12}\left\{3\sin2\beta\cos\gamma + \eta_\lambda\left[\cos2\alpha\sin2\beta\cos\gamma - 2\sin2\alpha\sin\beta\sin\gamma\right]\right\}^2$
	0	$6\,D_s - 2\,R\,D_a$	$\dfrac{3d_{z,\lambda}^2}{10}\dfrac{1}{8R(R+1)}\left\{\begin{array}{l}(R+1)\left(3\cos^2\beta-1-\eta_\lambda\sin^2\beta\cos2\alpha\right)\\ -\,D_r\left[3\sin^2\beta\cos2\gamma - \eta_\lambda\left(\cos2\alpha\cos2\gamma(\cos^2\beta+1)-2\sin2\alpha\sin2\gamma\cos\beta\right)\right]\end{array}\right\}^2$
	1	$6\,D_s - D_a\,(1 + 3\,D_r)$	$\dfrac{3d_{z,\lambda}^2}{10}\dfrac{1}{12}\left\{3\sin2\beta\sin\gamma + \eta_\lambda\left[\cos2\alpha\sin2\beta\sin\gamma + 2\sin2\alpha\sin\beta\cos\gamma\right]\right\}^2$
	2	$6\,D_s + 2\,R\,D_a$	$\dfrac{3d_{z,\lambda}^2}{10}\dfrac{1}{24R(R+1)}\left\{\begin{array}{l}-3D_r\left(3\cos^2\beta-1-\eta_\lambda\sin^2\beta\cos2\alpha\right)\\ +\,(R+1)\left[3\sin^2\beta\cos2\gamma - \eta_\lambda\left(\cos2\alpha\cos2\gamma(\cos^2\beta+1)-2\sin2\alpha\sin2\gamma\cos\beta\right)\right]\end{array}\right\}^2$

Table 1.5. Correlation times and coefficients for fully asymmetric global tumbling. $D_s = \tfrac{1}{3}(D_x + D_y + D_z)$, $D_a = D_z - \tfrac{1}{2}(D_x + D_y)$, $D_r = (D_y - D_x)/2D_a$, and $R = (1 + 3D_r)^{1/2}$. D_x, D_y, and D_z are the principle components of the symmetric diffusion tensor.

while avoiding over-interpretation of the data that could result from the insistence of a particular model. A simple description like this would address at least two properties of the motion, namely the amplitude and timescale of the motion. The most common approach in biomolecular NMR is to use the Model-Free formalism developed by Lipari and Szabo in the early 80s.[92] Here, the correlation functions is divided into two parts representing independent overall and internal motions

$$f_{lm}(t) = C(t) = C_O(t)C_I(t). \tag{1.38}$$

The internal correlation function can be approximated by a series of exponentials, with the most common, single-exponential function taking the form

$$C_I(t) \ = \ S^2 \ + \ (1\text{-}S^2) \ e^{-t/\tau_e} \tag{1.39}$$

where S is the generalized order parameter describing the restriction of the motion and τ_e is an effective correlation time that depends on both the local diffusive rates and spatial properties of the motion, thus complicating its interpretation. The parameter S^2 ranges from 0 to 1 for unrestricted isotropic internal motions to fully rigid, or no internal motion, respectively. Using the general expression for the overall motions in Equation 1.37, the Fourier transform of the correlation function is now given as

$$g_2(\omega) = \sum_{k=-2}^{2} c_k \left(\frac{S^2 \tau_k}{1+\omega^2\tau_k^2} + \frac{(1-S_F^2)\tau}{1+\omega^2\tau^2} \right) \tag{1.40}$$

where, $\tau^{-1} = \tau_k^{-1} + \tau_e^{-1}$ and $\tau_k = \tau_{2k}$ and $c_k = c_{2k}$. For convenience, the first rank components of diffusion are neglected. Although the separation of internal and overall motions is not rigorously true for molecules with anisotropic overall tumbling, Lipari and Szabo showed that the expressions are exact when $\omega^2\tau_e^2 \ll 1$, the motions do not modulate overall tumbling, and $\tau_e \ll \tau_m$.[92] For carbon dipolar interactions at 14.1 T, this amounts to τ_e of less than ~70 ps. For motions with $\omega^2\tau_e^2 \sim 1$ or higher, >210 ps for carbon at 14.1 T, the parameter errors are expected to be less than 25%, depending on the amplitude of the motion and the number of measurements. In situations where a single correlation time is not sufficient to fit the NMR data, an extension to the Model-Free formalism was

proposed by Clore et al. in which a second exponential is added to the internal correlation[93]

$$C_I(t) \;=\; S^2 \;+\; (1\text{-}S_F{}^2)\ e^{\text{-t/tf}} \;+\; (S_F{}^2\text{-}S^2)\ e^{\text{-t/ts}} \tag{1.41}$$

where $S^2 = S_F{}^2 S_S{}^2$ and S_F (τ_F) and S_S (τ_S) are the order parameters (effective correlation times) for the fast and slow motions, respectively. For the case of anisotropic overall diffusion the Fourier transform becomes

$$g_2(\omega) = \sum_{k=-2}^{2} c_k \left(\frac{S^2 \tau_k}{1+\omega^2 \tau_k^2} + \frac{(1-S_F^2)\tau_{k,F}}{1+\omega^2 \tau_{k,F}^2} + \frac{(S_F^2 - S^2)\tau_{k,S}}{1+\omega^2 \tau_{k,S}^2} \right) \tag{1.42}$$

where, $\tau_{k,q}{}^{-1} = \tau_k{}^{-1} + \tau_q{}^{-1}$ with q being either F or S.

All of the equations so far can be used to describe the relaxation contribution for a single mechanism whereas the total relaxation of a spin is the result of many interactions. The total relaxation rate for a carbon spin, for example, limiting ourselves to the CSA and dipolar interactions and neglecting first rank contributions to chemical shielding, can be written as the sum of all these contributions,[94,95]

$$\begin{aligned}
\frac{d(\Delta C_z(t))}{dt} &= -\left(\varrho_{C,CSA} + \sum_i \varrho_{CH_i} + \sum_j \varrho_{CC_j} \right)(\Delta C_z(t)) - \sum_i \sigma_{CH_i} \left(\Delta H_{i,z}(t) \right) \\
&\quad - \sum_j \sigma_{CC_j} \left(\Delta C_{j,z}(t) \right)
\end{aligned} \tag{1.43}$$

$$\frac{d(\Delta C_+(t))}{dt} = -\left(R_{2,CSA} + \sum_i R_{2,CH_i} + \sum_j R_{2,CC_j} \right)(\Delta C_+(t)) + R_{ex} \tag{1.44}$$

in which longitudinal dipolar auto- and cross-relaxation, ϱ and σ, and transverse relaxation, R_2, are given by

$$\varrho_{CX} = R_{1,CX} = \left(\mu_0 h \gamma_C \gamma_X / 8\pi^2 \right)^2 \left\{ 2g_2^{DD}(\omega_C + \omega_X) + \frac{1}{3}g_2^{DD}(\omega_C - \omega_X) + g_2^{DD}(\omega_C) \right\}$$

$$\sigma_{CX} = \left(\mu_0 h \gamma_C \gamma_X / 8\pi^2 \right)^2 \left\{ 2g_2^{DD}(\omega_C + \omega_X) - \frac{1}{3}g_2^{DD}(\omega_C - \omega_X) \right\}$$

$$R_{2,CX} = \frac{1}{2}\left(\mu_0 h \gamma_C \gamma_X / 8\pi^2\right)^2 \left\{ \begin{array}{l} 2g_2^{DD}(\omega_C + \omega_X) + 2g_2^{DD}(\omega_X) \\ + \frac{1}{3}g_2^{DD}(\omega_C - \omega_X) + g_2^{DD}(\omega_C) + \frac{4}{3}g_2^{DD}(0) \end{array} \right\}$$

$$\varrho_{CSA} = R_{1,CSA} = \omega_C^2 \left\{ g_2^{CSA}(\omega_C) \right\}$$

$$R_{2,CSA} = \frac{1}{2}\omega_C^2 \left\{ g_2^{CSA}(\omega_C) + \frac{4}{3}g_2^{CSA}(0) \right\}. \tag{1.45}$$

R_{ex} is the chemical exchange contribution to transverse relaxation. In principle, each of the relaxation rates listed in Equations 1.43 and 1.44 will be sensitive to different motional modes and would require separate order parameters. It is important to note that longitudinal carbon relaxation is also dependent on the magnetization state of neighboring carbon and proton spins through cross-relaxation, making it fundamentally a multi-exponential process. These cross-relaxation pathways can be controlled by eliminating any magnetization on neighboring spins before monitoring the decay of the carbon of interest. The initial decay of the magnetization will then be, to a good approximation, mono-exponential up to delays of $\sim 1/R_1$.[94]

A critical step in the analysis of relaxation data is the choice of "model" to accurately describe the underlying process. Here, "models" represent the particular set of adjustable parameters that are being determined during the analysis. These are outlined by d'Auvergne and Gooley as[96]

M0 = none,

M1 = S^2,

M2 = S^2, τ_e,

M3 = S^2, R_{ex},

M4 = S^2, τ_e, R_{ex},

M5 = S^2, S_F^2, τ_S,

M6 = S^2, τ_F, S_F^2, τ_S,

$M7 = S^2, S_F^2, \tau_S, R_{ex},$

$M8 = S^2, \tau_F, S_F^2, \tau_S, R_{ex},$

$M9 = R_{ex}.$

Here, R_{ex} is the contribution to transverse relaxation by chemical exchange. Order parameters that are not being varied in a given model are assumed to have a value of 1 while correlation times or exchange contributions excluded from the fitting are set to 0. Models 1 through 5 are the standard single field models first used by Clore, et al.[97]

The choice of model, in some sense, is an application of Occam's razor and is a balance between the accuracy and precision of the resulting parameters. Perhaps intuitively, using more parameters to fit the data will result in less precision, whereas under-fitting will add a bias and be less accurate. Given the interrelatedness of the model free parameters, how this bias will manifest is difficult to predict. In addition to the internal motional parameters, the choice of the global diffusion model, whether isotropic, anisotropic, or fully asymmetric, can have a dramatic effect on the results. A number of methods have been proposed for this selection process including hypothesis testing[98], Bayesian methods[99], Akaike's Information Criteria (AIC), bootstrap, and cross-validation.[100] In hypothesis testing, models are tested in a step-wise manner using χ^2 and F-statistics, incrementally increasing in complexity. While hypothesis testing is most widely used in analyzing relaxation data of proteins and nucleic acids, arguments have been made against its use due to its inability to test non-nested models and tendency to under-fit the data.[99-102] In bootstrap, simulated data is generated using the experimental uncertainties of the input data. These new data are minimized and the mean value of the χ^2 statistic is then used for the model selection. The cross-validation test iteratively removes a single measurement and then minimizes parameters using the remaining data to predict the removed datum. The χ^2 between the measured and predicted values is the cross-validation criterion. Bootstrap and cross-validation have the opposite problem in that they tend to be overly optimistic, slightly over-fitting the data, although they outperform hypothesis testing. In addition, cross validation requires more than

three independent measurements are made, which is what is typically measured at a single field strength. Most of the above methods require numerous simulations to arrive at significance parameters or repetitive analysis of the data after removing some of the input before a model selection can be made. AIC and Bayesian Information Criteria (BIC), developed from differing fields of statistics, are closely related to the χ^2 parameter,

$$AIC = \chi^2 + 2p$$

$$BIC = \chi^2 + p \ln M \tag{1.46}$$

where p is the number of floating model free parameters and M is the number of independent measurements, which is easily calculated during the fitting procedure and makes model selection much faster. The best model is chosen as the one with the lowest AIC or BIC value. They do not rely on subjective parameters like the significance level, and have been found to be more accurate and precise than hypothesis testing.[100,103] After a model is chosen additional criteria may be applied, such as model elimination[104] or a final quality check of the model's ability to satisfactorily describe the data[103], followed by Monte Carlo simulations to estimate parameter errors.

With a means of discussing internal motions, we can now address one final issue regarding shielding antisymmetry. Using the expressions for relaxation given in Table 1.5 and Equations 1.34 and 1.35, it can be concluded the antisymmetric component of chemical shielding will not significantly contribute to the transverse relaxation since the second rank component has a zero frequency term which dominates the relaxation of biomolecules with $\omega^2 \tau_c^2 > 1$. Longitudinal relaxation does not have any zero frequency component, so the effect of antisymmetry can be more profound. Using an isotropic diffusion model, the symmetric and antisymmetric contributions to R_1 can be written

$$R_1 = \omega^2 \left(\frac{2}{3} A\sigma^2 \frac{\tau_1}{1+\omega^2\tau_1^2} + \frac{2}{15} CSAa^2 \frac{\tau_2}{1+\omega^2\tau_2^2} \right)$$

$$= \omega^2 \left(\frac{2}{3} A\sigma^2 \frac{3\tau_c}{1+\omega^2\left(3\tau_c^2\right)} + \frac{2}{15} CSAa^2 \frac{\tau_c}{1+\omega^2\tau_c^2} \right) \qquad (1.47)$$

$$= 2\omega^2 \left(A\sigma^2 J(3\omega) + \frac{1}{15} CSAa^2 J(\omega) \right)$$

where the relationship $\tau_1 = 3\tau_2 = 3\tau_c$ for the different correlation times of the first and second rank components of the diffusion tensor, $A\sigma = (\sigma_{12}^2 + \sigma_{13}^2 + \sigma_{23}^2)^{1/2}$, and the spectral density function $J(\omega)$ is a simplification of the $g_2(\omega)$ given in Equation 1.37 where $c_k = 1/5$ and $\tau_k = \tau_c$. It can be seen that the antisymmetric component can have up to 15 times the contribution that an anisotropic component of similar magnitude would have. However, in practice, the antisymmetry is expected to be at most 5-25 ppm, or 5-15%, of the CSA magnitude. For a rigid biomolecule at 14.1 T, this would amount to less than 5% of the longitudinal relaxation rate. However, fast internal motions can exacerbate the affect that antisymmetry has on longitudinal relaxation. A simple illustration of this effect can be obtained by using the model free formalism in place of the $J(\omega)$. Antisymmetry contributions calculated in Figure 1.4 are calculated for a correlation time of 20 ns at 14.1 T, a carbon CSAa of 135 ppm and $A\sigma$ of 25 ppm. As it can be seen, even low amplitude motions on the order of 200 ps can have significant antisymmetry contributions in such a scenario, and larger for highly mobile regions, such as partially unfolded motifs in
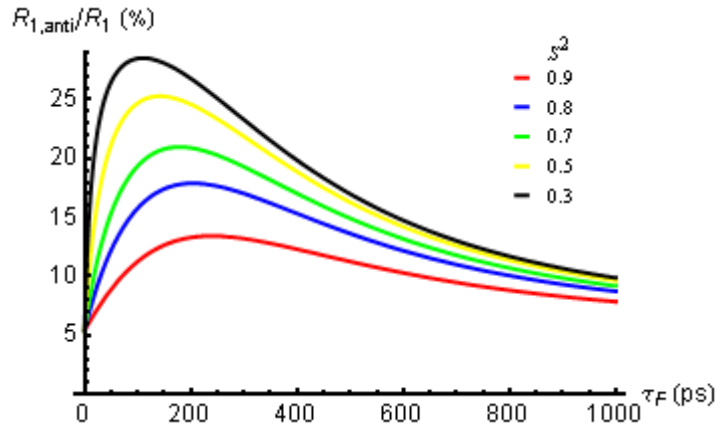
Figure 1.4. Antisymmetric contribution to R_1 modeled with fast internal motions.

proteins and nucleic acids. Ultimately, the consequence of this effect is to modulate the expected internal correlation time of the fast motions which contribute most significantly to R_1 and NOE measurements. Clearly, a better understanding of the magnitude of the antisymmetry of commonly studied nuclei would be beneficial for the study of heteronuclear longitudinal relaxation rates.

1.2.3 Chemical Exchange

Chemical reactions and conformational changes that affect the molecular environment around a nucleus and occur slower than overall tumbling can be studied in a different way by NMR spectroscopy. These changes often have the effect of modulating the chemical shift as it exchanges between various chemically distinct states. This phenomenon can be described by simple kinetic schemes. For the simple case of 2-site exchange this would be written[79]

$$A \underset{k_{21}}{\overset{k_{12}}{\longleftrightarrow}} B \tag{1.48}$$

in which exchange between states A and B are governed by unimolecular or pseudo-first-order rate constants k_{ij}. This allows the kinetic rate laws for the system to be written

$$\frac{d}{dt}\begin{pmatrix}[A](t)\\[B](t)\end{pmatrix}=\begin{pmatrix}-k_{12} & k_{21}\\ k_{12} & -k_{21}\end{pmatrix}\begin{pmatrix}[A](t)\\[B](t)\end{pmatrix} \tag{1.49}$$

which has the known solution

$$\begin{pmatrix}[A](t)\\[B](t)\end{pmatrix}=\begin{pmatrix}\dfrac{k_{12}e^{-(k_{12}+k_{21})t}+k_{21}}{k_{12}+k_{21}} & -\dfrac{k_{21}(e^{-(k_{12}+k_{21})t}-1)}{k_{12}+k_{21}}\\ -\dfrac{k_{12}(e^{-(k_{12}+k_{21})t}-1)}{k_{12}+k_{21}} & \dfrac{k_{21}e^{-(k_{12}+k_{21})t}+k_{12}}{k_{12}+k_{21}}\end{pmatrix}\begin{pmatrix}[A]_0\\[B]_0\end{pmatrix}. \tag{1.50}$$

This can be generalized for N-site exchange in matrix form as

$$\frac{d\mathbf{A}(t)}{dt}=\mathbf{K}\mathbf{A}(t)$$
$$\mathbf{A}(t)=e^{\mathbf{K}t}\mathbf{A}_0=\mathbf{U}^{-1}e^{\mathbf{D}t}\mathbf{U}\mathbf{A}_0 \tag{1.51}$$

where $\mathbf{A}(t)$ and $\mathbf{A}_0$ are Nx1 vectors containing the time dependence and initial

concentrations of the exchanging states, $\mathbf{K}$ is an NxN kinetic rate matrix with $K_{ij} = k_{ji}$ for $i \neq j$ and diagonal elements

$$K_{ii} = -\sum_{\substack{j=1 \\ j \neq i}}^{N} k_{ij} \, , \tag{1.52}$$

$\mathbf{U}$ is a unitary transformation matrix, $\mathbf{D}$ is a diagonal matrix, and $\mathbf{D} = \mathbf{URU}^{-1}$. For application to NMR, magnetization is proportional to the concentration of the given nuclear spin and the kinetic rate laws are incorporated into the magnetization evolution according to the Bloch-McConnell equations.[105] In the absence of applied radiofrequency fields, longitudinal and transverse relaxation are described by

$$\begin{aligned}
\frac{d\mathbf{M}_z(t)}{dt} &= (-\mathbf{R} + \mathbf{K})\Delta\mathbf{M}_z(t) \\
\frac{d\mathbf{M}^+(t)}{dt} &= (i\mathbf{\Omega} - \mathbf{R} + \mathbf{K})\mathbf{M}^+(t)
\end{aligned} \tag{1.53}$$

where $\Delta\mathbf{M}_z = \mathbf{M}_z(t) - \mathbf{M}_0$, $\mathbf{M}_0$ represents the equilibrium longitudinal magnetization, $\mathbf{\Omega}$ are the chemical offsets of the different states with $\Omega_{ij} = \delta_{ij}\,\Omega_j$, and $\mathbf{R}$ contains the intrinsic relaxation rates of the states with $R_{ij} = \delta_{ij}\,R_j$, and δ is the Kronecker delta function. When the initial magnetization is excited non-selectively so that the spin states are proportional to the equilibrium populations, then chemical exchange does not affect the longitudinal relaxation rates. Processes of this nature are typically monitored with so-called Z-exchange experiments with lifetimes on the order of 10^{-1} - 10^{-2} s^{-1} range, and typically do not cause any noticeable effect in standard biomolecular NMR experiments.[25,26] Transverse relaxation, on the other hand, is very sensitive to chemical exchange on the microsecond to millisecond timescale and can be observed as increased linewidths and/or multiple resonances in NMR spectra. Figure 1.5 illustrates these effects and was obtained by taking the Fourier transform of $\{M_{1,+}(t) + M_{2,+}(t)\}$ from the solution to Equation 1.53. The broadening of resonances is most pronounced for intermediate exchange, when $k_{ex} = k_{12} + k_{21} \approx \Delta\omega$, even for small populations of the minor state. On the other hand, it can be difficult to distinguish resonances in fast exchange from those in slow exchange and low populated minor states such that the minor state is

hidden within the noise of standard experiments. Instead, direct measurement of transverse relaxation rates is required and will be discussed further in §1.3.2 and §1.3.3.
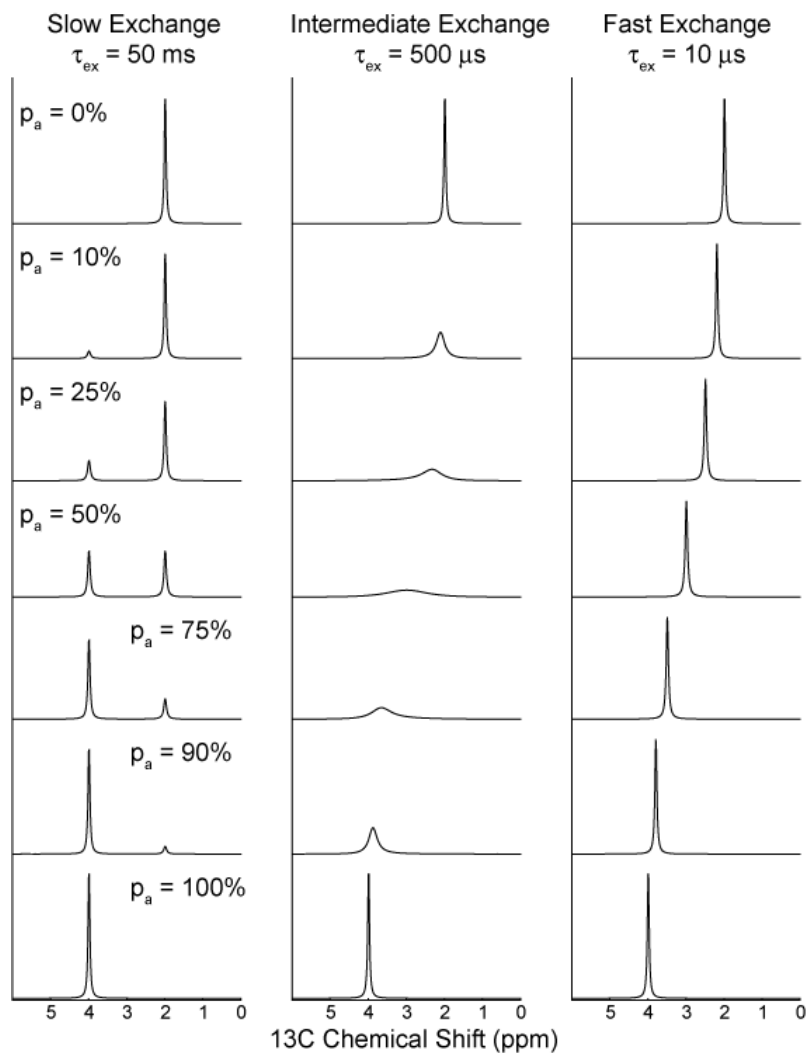
Figure 1.5. The effect of chemical exchange on ^{13}C resonances frequencies and linewidths. Parameters used for the simulation were $\omega_C/2\pi$ = 150.9 MHz, $\Delta\omega$ = 2 ppm = 1896.3 s^{-1}, $M_{0,A}$ = p_A, $M_{0,B}$ = p_B, and $R_{2,A}$ = $R_{2,B}$ = 25.0 s^{-1}. Populations p_A = 1 - p_B are shown in the left panel while timescales of the motion, $1/\tau_{ex}$ = k_{ex} = k_{12} + k_{21}, are shown at the top of the figure.

1.3 Measurements

1.3.1 RDCs and RCSAs

The measurement of residual dipolar couplings (RDCs) or residual chemical shift anisotropies (RCSAs) requires running high resolution experiments to record either scalar couplings or chemical shifts with high accuracy. These experiments are then repeated under any number of partial alignment conditions. A lot of development in accurately measuring scalar couplings has been pursued in order to achieve higher quality biomolecular structures by NMR. They have the added benefit that they can be used to record accurate chemical shifts simultaneously and will therefore be the current focus. Scalar couplings are commonly measured in one of two principle ways: through frequency-based measurement of splittings in the direct or indirect dimension of a multidimensional experiment, or through intensity-based experiments such as quantitative J correlation experiments.[106,107] The latter is accomplished through the measurement of peak intensity rations of in-phase and anti-phase signals or the J-modulated pulse sequences which monitor the evolutions of the scalar coupling in much the same way a relaxation experiment is recorded (see § 1.3.2). All of these are subject to a number of relaxation effects and require careful pulse sequence development and choice of spin system to avoid systematic errors in the measurements. The main disadvantage of frequency-based techniques is inaccuracy in the frequencies themselves, which are subject artificial shifts in peak maxima from differential line broadening or partial cancellation of overlapping signals. Quantitative J experiments are affected by differences in the relaxation rates of the different peaks being monitored.[108] J-modulated experiments are less susceptible to these errors by monitoring only a single spin operator during a constant time delay. All types of measurements are affected to some degree by cross-correlated relaxation and dynamic frequency shifts, although the contribution is small compared to magnitude of the one-bond scalar and to a large degree canceled when measuring dipolar couplings.

The simplest measurements are of one bond NH or CH scalar couplings which can be achieved by recording HSQC or HMQC experiments with heteronuclear decoupling turned off during acquisition. This has three main disadvantages: a decrease in sensitivity as the signal is cut effectively in half, an increase in spectral overlap as the number of peaks is doubled, and the evolution of undesired H-X multi-bond couplings. Multibond couplings are frequently smaller than the linewidth of the signals in biomacromolecules and result in an overall decrease in sensitivity and resolution. Proton-proton couplings in particular can have a detrimental effect on the quality of spectra recorded in aligned solutions. While the scalar coupling may be small, proton-proton distances of 2.5 Å, can easily leading to dipolar couplings up to 15 Hz. Large multibond heteronuclear couplings, such as the $^2J_{C2N1}$, $^2J_{C2N3}$, and $^2J_{C8N7}$ couplings in purines (~10-12 Hz)[109], could be used as additional targets for RDC measurements. However, these will also decrease sensitivity and resolution and increase spectral overlap.

Fortunately, most of these issues can be overcome using TROSY-based and higher dimensionality experiments which record peaks of the one bond scalar coupling in separate experiments. While this requires the acquisition of at least two experiments instead of a single experiment, congestion in the spectrum is reduced as each experiment contains only one peak per residue. In addition, couplings measured in the indirect dimension (^{13}C or ^{15}N) are less sensitive to multibond RDCs with hydrogens as the heteronuclear gyromagnetic ratios are considerably smaller, with couplings to protons > 2.5 Å away of less than 3 Hz. Homonuclear carbon-carbon couplings can often be eliminated using selective pulses or constant-time detection of the indirect dimension. A number of such techniques have been developed for measurement of RDCs in nucleic acids.[110-114] The most accurate frequency-based experiments are E.COSY-type experiments which can easily measure small multi-bond couplings (<10 Hz).[115] The small unresolved couplings are recorded in one dimension from the relative difference of two components of a larger splitting that has been resolved in a second dimension of a multidimensional experiment. Examples of this approach proposed by Bax and

coworkers as 3-dimensional experiments are capable of resolving 5 couplings in HCCH spin systems in a single experiment[116] (such as H1'-C1'-C2'-H2' in the ribose: $^1J_{C1'H1'}$, $^1J_{C2'H2'}$, $^2J_{C1'H2'}$, $^2J_{C2'H1'}$, $^3J_{H1'H2'}$) or 8 couplings in methine-methylene pairs[117] (such as the C4'-C5' pair). Unfortunately, these experiments which not likely applicable to large nucleic acids, where spectral congestion and peak broadening from increased relaxation rates becomes a significant hindrance. Additional experiments for measuring one- and two-bond couplings in nucleic acids have been the subject of several reviews.[118-120]

In 1995, researchers in the Prestegard group were the first to measured RDCs in a biomolecule[121] by following the magnetic field dependence of scalar couplings of the paramagnetic protein, cyanometmyoglobin. They recognized that these residual dipolar interaction would prove to be a powerful tool in refining larger protein structures. The key development in 1997 by Bax and coworkers was the use of liquid crystalline media to orient their biomolecular samples in the magnetic field.[22,23] Since that time, numerous alignment media have been developed to achieve a variety of alignment orientations and different sample conditions, such as temperature and pH.[118-120,122] A common alignment media used for the study of nucleic acids are bacteriophages. Pf1 filamentous phage are 1-2 μm in length and about 6 nm in diameter and is composed of several thousand proteins coated on a core of single-stranded circular DNA.[123] Highly anisometric particles like Pf1 phage undergo spontaneous phase transitions from isotropic to chiral nematic phases above a certain critical concentration.[124,125] Below this concentration, the phase transition can be induced by the external magnetic field in what is known as a paranematic phase. For Pf1, the concentrations over which it will align in the magnetic field from several to tens of mg/mL and becomes mostly field independent at concentrations above 16 mg/mL. Another popular alignment medium for biomolecular studies are liquid crystalline bicelles, often composed of a mixture of dimyristoyl phosphatidylcholine (DMPC) and dihexanoyl phosphatidylcholine (DHPC) for magnetic resonance studies.[126] Here, the term 'bicelle' is used loosely to represent the mixture of long- and short-chain phospholipids for reasons that will be made clear shortly. Bicelles take on a variety of interesting morphologies depending on the lipid

concentrations, temperature, and any doping agents, and are thought to be an ideal medium for studying membrane associated proteins.[126-129] In lipid ratios of about 3:1 DMPC:DHPC, total lipid concentration of ~8-30 wt%, and temperatures less than 25 °C, bicelles are isotropic and take the form of the common visualization of disk-shaped micelles, for which the term 'bicelle' was coined, that have a width of roughly 5 nm and a diameter of 20-50 nm. Above this temperature they undergo a phase transition to a chiral nematic phase that aligns in an external magnetic field. The exact nature of this phase has been somewhat controversial with suggestions from NMR studies of being disk-shaped[23], to small-angle neutron scattering (SANS) studies suggesting 'swiss cheese'-like perforated lamellar sheets.[130] More recently, it has rather definitively been shown by SANS, polarized light microscopy, and cryo-transmission electron microscopy that the phase is best described as being made of worm-like micelles that are again 5-10 nm wide but 10s of μm in length, much like Pf1 phage mentioned above.[131,132] Negative anisotropy of the magnetic susceptibility gives rise to the magnetic alignment observed by NMR.[133,134] At temperatures above 50°C, the bicelle mixture forms multi-lamellar vesicles. Because of its temperature induced phase transition to a magnetically aligned phase, it is ideal for the measurement of RDCs and RCSAs in biomolecules as both isotropic and aligned experiments can be measured from a single sample. The temperature dependence of heteronuclear chemical shifts is to a good approximation linear over the range of temperatures and this will be demonstrated in Chapter 2.

1.3.2 Spin Relaxation - R_1, R_2, and het-NOE

In order to extract accurate dynamical information from spin relaxation measurements, simple isolated spin systems are preferable. Proton spins are convoluted by the abundance of other neighboring protons and are not often interpreted in terms of ps-ns dynamics, although sophisticated experiments have been developed for measuring μs-ms chemical exchange.[135-138] The sensitivity of heteronuclear NMR experiments is enhanced by a factor of $(\gamma_H/\gamma_S)^{5/2}$ when magnetization begins and ends on

a proton, as compared to direct excitation and detection of the S spin magnetization, where S is either ^{13}C or ^{15}N. This results in up to a 32 (316) fold enhancement for carbons (nitrogens). Heteronuclei are considerably less sensitive to long range proton interactions and can largely be described by their dipolar interaction with their directly attached proton and chemical shift anisotropy. This is particularly true for nitrogen spin, which are routine used in the description of protein dynamics and have been the subject of many reviews.[83,139,140] Unfortunately, imino nitrogens in nucleic acids are only observable when protected from exchange with water, such as in canonical Watson-crick helices. This provides at most one spin system for every base pair in the RNA/DNA. The non-exchangeable carbon spins are a much more abundant source of dynamic information but this leads to significant additional complications. CC scalar couplings range from 8-12 Hz, for 3-4 bond couplings in the aromatic ring, to over 80 Hz for directly bonded carbons.[109] Preventing the evolution of these couplings and accounting for their additional contributions to relaxation is non-trivial and a primary focus of Chapter 3 and will be discussed only briefly here.

The basic heteronuclear longitudinal or transverse relaxation experiment consists of i) preparation of the pure S spin magnetization, of the form S_z or $S_{x/y}$ respectively, ii) a relaxation block, iii) chemical shift encoding, iv) transfer back to a proton, and v) detection. The heteronuclear NOE experiment differs from this basic procedure and is discussed below. Preparation of S magnetization is commonly accomplished using Insensitive Nucleus Enhanced Polarization Transfer (INEPT) elements. During the relaxation block, the spin is allowed to decay for a time T while carefully controlled to prevent unwanted cross- or cross-correlated relaxation mechanisms from contributing. Afterwards, the indirect dimension is encoded with the chemical shift of the heteronuclear spin. For carbon spins in uniformly labeled samples, it is often necessary to include some form of homonuclear decoupling, either through constant-time evolution or application of selective pulses, to remove $^nJ_{CC}$ couplings from the indirect dimension. A refocused-INEPT or Spin State Selective Coherence Transfer (S^{3}CT)[141] is then used to return magnetization to the directly attached hydrogen before detection.

Using these affords the preservation of equivalent pathways (PEP)[142,143] phase cycling schemes and, in the case of S[3]CT, TROSY sensitivity enhancements. Appropriate broadband decoupling is applied during detection of the proton signal, if TROSY detection is not used. While the purpose of this is to eliminate the large scalar coupling to the directly bonded heteronucleus, some carbon spins in the aromatic rings have large $^2J_{HN}$ couplings (10-15 Hz) that can give rise to observable couplings in the direct dimension if additional decoupling is not applied to the nitrogen spins.

The critical elements that will govern the decay of the signal are the preparation and relaxation blocks. As discussed previously, longitudinal magnetization is dependent on the initial magnetization of neighboring carbon and proton spins. During the relaxation delay, proton cross-relaxation and CH-dipole/CSA cross-correlated relaxation are effectively suppressed with a train of hard 180° pulses or broadband decoupling. Homonuclear interactions are not so easily controlled during the relaxation delay without affecting the spin of interest so selective excitation is necessary during the initial INEPT elements and equilibrium carbon magnetization should be destroyed prior to the first proton 90° pulse.[94] The former prevents buildup of magnetization on neighboring protonated carbons (i.e. C1'/C2' in the ribose or C5/C6 in pyrimidines) while the latter suppresses cross-relaxation to quaternary carbons in the aromatic rings. Alternatively, in small biomolecules, $\tau_c <$ ~5 ns, the auto- and cross-relaxation rates are nearly equal and opposite, thus non-selective excitation during the preparation block would cancel the CC interactions leaving the interpretation to a good approximation dependent only on CH-dipole and CSA relaxation mechanisms. Long range carbon interactions, such as those with quaternary carbons, are negligible in small nucleic acids. The systematic error in this approximation grows to over 100% for molecules with global tumbling times of 17 ns.[95,144] The relaxation of magnetization anti-parallel to the static magnetic field as carbon/nitrogen magnetization returns to equilibrium during the relaxation block is governed by a three-parameter exponential decay, $H_z(t) = H_z(\infty) + H_z(0)\exp(-R_1 t)$ and is dependent on the initial proton magnetization. Accurate measurements of R_1 can be difficult and time consuming as this requires delays of several to tens of seconds

between scans to return proton magnetization to its equilibrium state.[145] By applying a phase cycle that alternates the phase of carbon/nitrogen magnetization before the relaxation block with a simultaneous inversion of the receiver phase, the requirement for equilibrium conditions is removed and relaxation can be accurately measured with short (1-2 sec) pre-delays and rates can be determined from intensity fits to two parameter exponential decays, $I(t) = I_0 \exp(-R_1 T)$.[146]

Transverse relaxation is often measured using Carr-Purcell-Meiboom-Gill (CPMG) or rotating-frame ($R_{1\rho}$) relaxation techniques. CPMG experiments maintain transverse magnetization by applying a train of 180° refocusing pulses on the carbon/nitrogen channel during the relaxation block, whereas application of a continuous wave rf field, or spinlock, is used in $R_{1\rho}$ studies. While CPMG experiments are routinely applied in the study of protein dynamics, the abundant scalar coupling networks makes them less amenable for studies of nucleic acids. Even the nitrogen spins have scalar couplings on the order of ~7 Hz to their hydrogen bond partners[70] and can cause significant artifacts in CPMG experiments.[147-149] Using low power refocusing pulses to prevent J_{NN} coupling evolution during the relaxation delay can suppress this effect but in turn can lead to off-resonance effects.[150] Methods have been developed to suppress or correct for these errors[151-153] and have been an important spin probe for large RNAs.[15,154-157] $R_{1\rho}$ techniques are arguably better suited for the study of nucleic acids. Generally, the spinlock will not be on resonance with most spins in multidimensional experiments and the magnetization will have an effective tilt angle of $\theta = \mathrm{atan}(\omega_1/\Omega)$, where ω_1 is the spinlock power, Ω is the offset of the spin from the spinlock frequency. The relaxation rate therefore has contributions from both R_1 and R_2 and is calculated as

$$R_{1\rho} = R_1 \cos^2\theta + R_2 \sin^2\theta. \tag{1.54}$$

Adiabatic passages are often used to align spins along their effective tilt angle, otherwise sensitivity can be lost for nuclei that are considerably off resonance from the spinlock due to B_1 field inhomogeneity.[158] In order to extract the transverse relaxation rate, accurate spinlock powers are necessary. These can be determined by monitoring

intensities of 2D spectra with and without the adiabatic passages or measuring one bond scalar couplings in the presence of weak continuous wave decoupling and relating them to their offset from the spinlock field.[19] Alternatively, the spinlock power can be directly obtained from a 2D B_1 nutation experiment, although rf field inhomogeneity causes small differences between the average and most-probable values.[159] Hartman-Hahn interactions between homonuclear scalar coupled spins can be reduced, often to less that 1‰, by appropriately choosing spinlock powers and offsets that minimize the function[160]

$$A_{HAHA} = \left(1 + \left(\frac{\omega_{eff,I} - \omega_{eff,S}}{J_{IS}(1 + \cos(\theta_I - \theta_S))/2} \right)^2 \right)^{-1} \tag{1.55}$$

where $\omega_{eff,X} = (\omega_1^2 + \Omega_X^2)^{1/2}$ and J_{IS} is the scalar coupling constant between spins I and S. For high power spinlocks ($\omega_1/2\pi > 1000$ Hz), the effects of CH-dipole/CSA cross-correlated relaxation and J_{CH} evolution are efficiently suppressed by two proton 180° pulses placed at times T/4 and 3T/4 during the spinlock.[161,162] Cross-correlations between CC-dipole/CSA or CC-dipole/CH-dipole are small, owing to the small gyromagnetic ratios of heteronuclei and non-ideal tilt angles between the various interactions, and are reviewed by Kumar et al.[163] Since there is an R_1 contribution to the relaxation rate, the phase cycling scheme used in longitudinal relaxation is also required.

In contrast to longitudinal and transverse relaxation techniques, heteronuclear NOE experiments are used to measure the ratio of intensities of spectra recorded with and without proton saturation in order to determine the proton cross-relaxation rate, σ. In the presence of proton saturation, the signal intensity of an isolated spin system is 'enhanced' by the factor

$$NOE = 1 + \gamma_H/\gamma_S \, \sigma/R_1 \, . \tag{1.56}$$

For nitrogens, γ_N is negative and results in a signal decrease in the saturation experiment. The carbon spins, unfortunately, are rarely isolated and the magnetization from the protons will bleed into neighboring spins and throughout the ring. It was shown that for two neighboring singly protonated carbons, the NOE will have be[94]

$$NOE = 1 + \frac{\gamma_H}{\gamma_C} \frac{\dfrac{\sigma_{C1H1}}{R_{1,C1}} - \dfrac{\sigma_{C1C2}}{R_{1,C1}} \dfrac{\sigma_{C2H2}}{R_{1,C2}}}{1 - \dfrac{\sigma_{C1C2}^2}{R_{1,C1}R_{1,C2}}} \qquad (1.57)$$

where σ_{XY} is the cross-relaxation rate between spin X and Y, and $R_{1,X}$ is the auto-relaxation rate for spin X. Three new relaxation rates enter into the equation and the effect of homonuclear cross-relaxation (σ_{C1C2}) will begin to dominate in larger systems. For molecules with tumbling times of 18 ns, the difference between equations 1.56 and 1.57 is more than 30%. In addition, the delay between successive scans should be about 4-5 times the length of the proton T_1 ($1/R_1$) which, as mentioned earlier, can result in very long delays. These issues make the NOE measurement largely unreliable for most spins in uniformly labeled nucleic acids, except for imino nitrogens and purine C2 and C8 spins.

1.3.3 Chemical Exchange - $R_{1\varrho}$ and $R_{2,CPMG}$

The techniques used for measuring transverse relaxation described in §1.3.2 can also be used to monitor chemical exchange. During the relaxation block, the effect of chemical exchange is suppressed by the different methods of keeping magnetization along the transverse plane. In the CPMG experiment, tighter spacing between the carbon 180° pulses refocuses the magnetization of the different spin states faster than they can exchange and results in suppression of the exchange process. By monitoring the effective relaxation rate as a function of the spacing between refocusing pulses, important kinetic parameters can be determined about the conformational change or chemical reaction taking place. If the CPMG train is defined as (δ - 180° - δ)$_N$ and exchange is fast, the effective relaxation rate is described by[16,18,19]

$$R_{2,eff} = \frac{1}{2}\left(R_{2,A} + R_{2,B} + k_{ex} - \frac{1}{2\delta}\operatorname{arccos} h(D_+ \cosh\eta_+ - D_- \cosh\eta_-)\right) \qquad (1.58)$$

where

$$D_\pm = \frac{1}{2}\left(\frac{\psi + 2\Delta\omega^2\omega_S^2}{\sqrt{\psi^2 + \zeta^2}} \pm 1\right)$$

$$\eta_\pm = \delta\sqrt{2}\sqrt{\sqrt{\psi^2 + \zeta^2} \pm \psi}$$

$$\psi = \left(R_{2,A} - R_{2,B} - p_A k_{ex} + p_B k_{ex}\right)^2 - \Delta\omega^2\omega_S^2 + 4p_A p_B k_{ex}^2$$

$$\zeta = 2\Delta\omega\,\omega_S\left(R_{2,A} - R_{2,B} - p_A k_{ex} + p_B k_{ex}\right)$$

(1.59)

and $\Delta\omega = \Omega_B - \Omega_A$ is the chemical shift difference between states A and B, p_A and p_B are the populations, $R_{2,A}$ and $R_{2,B}$ are the intrinsic relaxation rates, and ω_S is the Larmor frequency for the heteronucleus. However, as was mentioned above, CPMG experiments are not ideal for highly coupled networks such as those found in nucleic acids. Further details about the measurement of chemical exchange using CPMG techniques can be found in a number of reviews.[19,164,165]

Since 1970, it has been recognized that chemical exchange can be detected by monitoring the effective relaxation rate of a nucleus by varying the amplitude of a spinlock field.[17] However, only recently have expressions been developed that describe exchange outside of this fast exchange limit.[166-171] Primarily this has been due to the high lower limit of usable spinlock powers ($\omega_1/2\pi \approx 1000$ Hz) that would suppress exchange events slower than 300 µs almost completely. Below this spinlock power, conventional decoupling techniques would fail to suppress scalar coupling evolution and off-resonance effects and lead to oscillatory behavior of the magnetization decay.[161,162] Fortunately, new techniques have emerged that can allow the use of spinlocks as low as 25 Hz without distortion of the relaxation decay.[162,172-174] For fast exchange, the effect on the $R_{1\varrho}$ rate is simply

$$R_{1\varrho} = R_{1\varrho,\infty} + \sin^2\theta\frac{\Phi_{ex}k_{ex}}{k_{ex}^2 + \omega_{eff}^2}$$

(1.60)

where $\omega_{eff} = (\omega_1^2 + \Omega^2)^{1/2}$ is the effective spinlock strength of the nucleus at the population weighted average resonance offset from the spinlock frequency, $\Omega = p_A\Omega_A + p_B\Omega_B$, $R_{1\varrho,\infty}$ is the intrinsic rate given by Equation 1.54, and $\Phi_{ex} = p_A p_B \Delta\omega^2$ is used as a single fitting parameter. General expression for $R_{1\varrho}$ that are valid for all time scales can be found from

approximate solutions to the Bloch-McConnell equation of motion or the stochastic Liouville equation for a two spin system. The most accurate of these solutions uses Laguerre's method of polynomial root finding to arrive at[170]

$$R_{1\varrho} = R_{1\varrho,\infty} + \frac{\sin^2\theta p_A p_B \Delta\omega^2 k_{ex}}{\dfrac{\omega_A^2\omega_B^2}{\omega_{eff}^2} + k_{ex}^2 - \sin^2\theta p_A p_B \Delta\omega^2\left(1 + \dfrac{2k_{ex}^2\left(p_A\omega_A^2 + p_B\omega_B^2\right)}{\omega_A^2\omega_B^2 + \omega_{eff}^2 k_{ex}^2}\right)}$$

(1.61)

with additional parameters representing the effective spinlock power at each spin state. Despite the apparent complexity, this expression has only three unknown parameters, p_B, $\Delta\omega$, and k_{ex}. This is in effect an extension of an earlier result that were most accurate when the populations of the two states where highly skewed[171]

$$R_{1\varrho} = R_{1\varrho,\infty} + \frac{\sin^2\theta p_A p_B \Delta\omega^2 k_{ex}}{\dfrac{\omega_A^2\omega_B^2}{\omega_{eff}^2} + k_{ex}^2} \approx R_{1\varrho,\infty} + \frac{\sin^2\theta p_A p_B \Delta\omega^2 k_{ex}}{\Omega_B^2 + \omega_1^2 + k_{ex}^2}.$$

(1.62)

The second relationship helps to illustrate the effect of offset dependence of the spinlock as well as the power dependence. In particular, the effect of chemical exchange is at a maximum when the spinlock is on resonance with the minor state ($\Omega_B = 0$). Additional expressions have also been derived that have improved accuracy for the special cases of $p_A = p_B$ and the spinlock being placed at the average resonance frequency of the two states, $(\Omega_A + \Omega_B)/2$.

1.4 References

1. Williamson, J.R. Biophysical studies of bacterial ribosome assembly. *Current Opinion In Structural Biology* **18**, 299-304 (2008).

2. Al-Hashimi, H.M. & Walter, N.G. RNA dynamics: it is about time. *Current Opinion In Structural Biology* **18**, 321-329 (2008).

3. Jardetzky, O. NMR-Studies Of Macromolecular Dynamics. *Accounts Of Chemical Research* **14**, 291-298 (1981).

4. Weber, A.L. & Orgel, L.E. Formation Of Dipeptides From Amino-Acids And The 2'(3')-Glycyl Ester Of An Adenylate. *Journal Of Molecular Evolution* **13**, 185-191 (1979).

5. Leroy, J.L., Charretier, E., Kochoyan, M. & Gueron, M. Evidence From Base-Pair Kinetics For 2 Types Of Adenine Tract Structures In Solution - Their Relation To Dna Curvature. *Biochemistry* **27**, 8894-8898 (1988).

6. Yang, W. Structure and mechanism for DNA lesion recognition. *Cell Research* **18**, 184-197 (2008).

7. Kim, J.N. & Breaker, R.R. Purine sensing by riboswitches. *Biology Of The Cell* **100**, 1-11 (2008).

8. Gilbert, S.D., Stoddard, C.D., Wise, S.J. & Batey, R.T. Thermodynamic and kinetic characterization of ligand binding to the purine riboswitch aptamer domain. *Journal Of Molecular Biology* **359**, 754-768 (2006).

9. Muesing, M.A., Smith, D.H. & Capon, D.J. Regulation Of Messenger-Rna Accumulation By A Human-Immunodeficiency-Virus Transactivator Protein. *Cell* **48**, 691-701 (1987).

10. Puglisi, J.D., Tan, R.Y., Calnan, B.J., Frankel, A.D. & Williamson, J.R. Conformation Of The Tar Rna-Arginine Complex By Nmr-Spectroscopy. *Science* **257**, 76-80 (1992).

11. Long, K.S. & Crothers, D.M. Characterization of the solution conformations of unbound and Tat peptide-bound forms of HIV-1 TAR RNA. *Biochemistry* **38**, 10059-10069 (1999).

12. Jones, K.A. Taking a new TAK on Tat transactivation. *Genes & Development* **11**, 2593-2599 (1997).

13. Majello, B., Napolitano, G., Giordano, A. & Lania, L. Transcriptional regulation by targeted recruitment of cyclin-dependent CDK9 kinase in vivo. *Oncogene* **18**, 4598-4605 (1999).

14. Bloembergen, N. Spin Relaxation Processes In A 2-Proton System. *Physical Review* **104**, 1542-1547 (1956).

15. Zhang, Q., Sun, X.Y., Watt, E.D. & Al-Hashimi, H.M. Resolving the motional modes that code for RNA adaptation. *Science* **311**, 653-656 (2006).

16. Carver, J.P. & Richards, R.E. General 2-Site Solution For Chemical Exchange Produced Dependence Of T2 Upon Carr-Purcell Pulse Separation. *Journal Of Magnetic Resonance* **6**, 89-& (1972).

17. Deverell, C., Morgan, R.E. & Strange, J.H. Studies Of Chemical Exchange By Nuclear Magnetic Relaxation In Rotating Frame. *Molecular Physics* **18**, 553-& (1970).

18. Davis, D.G., Perlman, M.E. & London, R.E. Direct Measurements Of The Dissociation-Rate Constant For Inhibitor-Enzyme Complexes Via The T-1-Rho And T-2 (Cpmg) Methods. *Journal Of Magnetic Resonance Series B* **104**, 266-275 (1994).

19. Palmer, A.G., Kroenke, C.D. & Loria, J.P. Nuclear magnetic resonance methods for quantifying microsecond-to-millisecond motions in biological macromolecules. *Methods in Enzymology* **339**, 204-238 (2001).

20. Cornilescu, G., Marquardt, J.L., Ottiger, M. & Bax, A. Validation of protein structure from anisotropic carbonyl chemical shifts in a dilute liquid crystalline phase. *Journal Of The American Chemical Society* **120**, 6836-6837 (1998).

21. Ottiger, M., Tjandra, N. & Bax, A. Magnetic field dependent amide N-15 chemical shifts in a protein-DNA complex resulting from magnetic ordering in solution. *Journal Of The American Chemical Society* **119**, 9825-9830 (1997).

22. Tjandra, N. & Bax, A. Direct measurement of distances and angles in biomolecules by NMR in a dilute liquid crystalline medium (vol 278, pg 1111, 1997). *Science* **278**, 1697-1697 (1997).

23. Tjandra, N. & Bax, A. Direct measurement of distances and angles in biomolecules by NMR in a dilute liquid crystalline medium. *Science* **278**, 1111-1114 (1997).

24. Tolman, J.R., Al-Hashimi, H.M., Kay, L.E. & Prestegard, J.H. Structural and dynamic analysis of residual dipolar coupling data for proteins. *Journal Of The American Chemical Society* **123**, 1416-1424 (2001).

25. Sahu, D., Clore, G.M. & Iwahara, J. TROSY-based z-exchange spectroscopy: Application to the determination of the activation energy for intermolecular protein translocation between specific sites on different DNA molecules. *Journal Of The American Chemical Society* **129**, 13232-13237 (2007).

26. Farrow, N.A., Zhang, O.W., Formankay, J.D. & Kay, L.E. A Heteronuclear Correlation Experiment For Simultaneous Determination Of N-15 Longitudinal Decay And Chemical-Exchange Rates Of Systems In Slow Equilibrium. *Journal Of Biomolecular Nmr* **4**, 727-734 (1994).

27. Shajani, Z. & Varani, G. NMR studies of dynamics in RNA and DNA by C-13 relaxation. *Biopolymers* **86**, 348-359 (2007).

28. Duchardt, E. & Schwalbe, H. Residue specific ribose and nucleobase dynamics of the cUUCGg RNA tetraloop motif by NMR C-13 relaxation. *Journal Of Biomolecular Nmr* **32**, 295-308 (2005).

29. Shajani, Z. & Varani, G. C-13 NMR relaxation studies of RNA base and ribose nuclei reveal a complex pattern of motions in the RNA binding site for human U1A protein. *Journal Of Molecular Biology* **349**, 699-715 (2005).

30. Showalter, S.A. & Hall, K.B. Isotropic reorientational eigenmode dynamics complements NMR relaxation measurements for RNA. in *Nuclear Magnetic Resonance Of Biological Macromolecules, Part C*, Vol. 394 465-480 (2005).

31. Showalter, S.A., Baker, N.A., Tang, C.G. & Hall, K. Iron responsive element RNA flexibility described by NMR and isotropic reorientational eigenmode dynamics. *Journal Of Biomolecular Nmr* **32**, 179-193 (2005).

32. Bloch, F., Hansen, W.W. & Packard, M. Nuclear Induction. *Physical Review* **69**, 127-127 (1946).

33. Purcell, E.M., Torrey, H.C. & Pound, R.V. Resonance Absorption By Nuclear Magnetic Moments In A Solid. *Physical Review* **69**, 37-38 (1946).

34. Bloch, F., Hansen, W.W. & Packard, M. The Nuclear Induction Experiment. *Physical Review* **70**, 474-485 (1946).

35. Bloch, F. Nuclear Induction. *Physical Review* **70**, 460-474 (1946).

36. Franklin, R.E. & Gosling, R.G. Molecular Configuration In Sodium Thymonucleate. *Nature* **171**, 740-741 (1953).

37. Wilkins, M.H.F., Stokes, A.R. & Wilson, H.R. Molecular Structure Of Deoxypentose Nucleic Acids. *Nature* **171**, 738-740 (1953).

38. Watson, J.D. & Crick, F.H.C. Genetical Implications Of The Structure Of Deoxyribonucleic Acid. *Nature* **171**, 964-967 (1953).

39. Watson, J.D. & Crick, F.H.C. Molecular Structure Of Nucleic Acids - A Structure For Deoxyribose Nucleic Acid. *Nature* **171**, 737-738 (1953).

40. McDonald, C.C., Phillips, W.D. & Penman, S. Nucleic Acids - Nuclear Magnetic Resonance Study. *Science* **144**, 1234-& (1964).

41. McTague, J.P., Ross, V. & Gibbs, J.H. Nuclear Magnetic Resonance Study Of Synthetic Polynucleotides And Transfer Rna. *Biopolymers* **2**, 163-173 (1964).

42. Ernst, R.R. Sensitivity Enhancement In Magnetic Resonance.I. Analysis Of Method Of Time Averaging. *Review Of Scientific Instruments* **36**, 1689-& (1965).

43. Ernst, R.R. & Anderson, W.A. Sensitivity Enhancement In Magnetic Resonance.2. Investigation Of Intermediate Passage Conditions. *Review Of Scientific Instruments* **36**, 1696-& (1965).

44. Kearns, D.R., Patel, D.J. & Shulman, R.G. High Resolution Nuclear Magnetic Resonance Studies Of Hydrogen Bonded Protons Of Transfer Rna In Water. *Nature* **229**, 338-& (1971).

45. Reid, B.R. & Hurd, R.E. Application Of High-Resolution Nuclear Magnetic-Resonance Spectroscopy In Study Of Base-Pairing And Solution Structure Of Transfer-Rna. *Accounts Of Chemical Research* **10**, 396-402 (1977).

46. Patel, D.J. High-Resolution Nmr-Studies Of Structure And Dynamics Of Transfer-Rna In Solution. *Annual Review Of Physical Chemistry* **29**, 337-362 (1978).

47. Schimmel, P.R. & Redfield, A.G. Transfer-Rna In Solution - Selected Topics. *Annual Review Of Biophysics And Bioengineering* **9**, 181-221 (1980).

48. Reid, B.R. Nmr-Studies On Rna Structure And Dynamics. *Annual Review Of Biochemistry* **50**, 969-996 (1981).

49. Gueron, M. P-31 Magnetic Resonance Of Purified Transfer Rna. *Febs Letters* **19**, 264-& (1971).

50. Gueron, M. & Shulman, R.G. P-31 Magnetic-Resonance Of Transfer-Rna. *Proceedings Of The National Academy Of Sciences Of The United States Of America* **72**, 3482-3485 (1975).

51. Bolton, P.H. & James, T.L. Molecular Motions In Rna And Dna Investigated By P-31 And C-13 Nmr Relaxation. *Journal Of Physical Chemistry* **83**, 3359-3366 (1979).

52. Horowitz, J., Ofengand, J., Daniel, W.E. & Cohn, M. F-19 Nuclear Magnetic-Resonance Of 5-Fluorouridine-Substituted Transfer-Rna1val From Escherichia-Coli. *Journal Of Biological Chemistry* **252**, 4418-4420 (1977).

53. Marshall, A.G. & Smith, J.L. Nuclear Spin-Labeled Nucleic-Acids.1. F-19 Nuclear Magnetic-Resonance Of Escherichia-Coli 5-Fluorouracil-5s-Rna. *Journal Of The American Chemical Society* **99**, 635-636 (1977).

54. Morris, G.A. & Freeman, R. Enhancement Of Nuclear Magnetic-Resonance Signals By Polarization Transfer. *Journal Of The American Chemical Society* **101**, 760-762 (1979).

55. Bodenhausen, G. & Ruben, D.J. Natural Abundance N-15 Nmr By Enhanced Heteronuclear Spectroscopy. *Chemical Physics Letters* **69**, 185-189 (1980).

56. Gust, D., Moon, R.B. & Roberts, J.D. Applications Of Natural-Abundance Nitrogen-15 Nuclear Magnetic-Resonance To Large Biochemically Important Molecules. *Proceedings Of The National Academy Of Sciences Of The United States Of America* **72**, 4696-4700 (1975).

57. Lapidot, A. & Irving, C.S. Dynamic Structure Of Whole Cells Probed By Nuclear Overhauser Enhanced N-15 Nuclear Magnetic-Resonance Spectroscopy. *Proceedings Of The National Academy Of Sciences Of The United States Of America* **74**, 1988-1992 (1977).

58. James, T.L., James, J.L. & Lapidot, A. Structural And Dynamic Information About Double-Stranded Dna From N-15 Nmr-Spectroscopy. *Journal Of The American Chemical Society* **103**, 6748-6750 (1981).

59. Lipari, G. & Szabo, A. Nuclear Magnetic-Resonance Relaxation In Nucleic-Acid Fragments - Models For Internal Motion. *Biochemistry* **20**, 6250-6256 (1981).

60. Olsen, J.I. et al. C-13 Nmr Relaxation Studies Of Pre-Melt Structural Dynamics In [4-C-13-Labeled Uracil] Labeled Escherichia-Coli Transfer Rna1val. *Nucleic Acids Research* **10**, 4449-4464 (1982).

61. Schweizer, M.P., Hamill, W.D., Walkiw, I.J., Horton, W.J. & Grant, D.M. C-13 Nmr-Studies On [4-C-14] Uracil Labeled Escherichia-Coli Transfer Rna-Ival. *Nucleic Acids Research* **8**, 2075-2083 (1980).

62. Tompson, J.G. & Agris, P.F. Production Of Specific Site Probes Of Transfer-Rna Structure By Enrichment With C-13 At Particular Locations. *Nucleic Acids Research* **7**, 765-779 (1979).

63. Agris, P.F., Fujiwara, F.G., Schmidt, C.F. & Loeppky, R.N. Utilization Of An Escherichia-Coli Mutant For C-13 Enrichment Of Transfer-Rna For Nmr-Studies. *Nucleic Acids Research* **2**, 1503-1512 (1975).

64. Schmidt, P.G., Playl, T. & Agris, P.F. Internal Dynamics Of Transfer Ribonucleic-Acid Determined By Nuclear Magnetic-Resonance Of C-13-Enriched Ribose C-1. *Biochemistry* **22**, 1408-1415 (1983).

65. Nikonowicz, E.P. & Pardi, A. 3-Dimensional Heteronuclear Nmr-Studies Of Rna. *Nature* **355**, 184-186 (1992).

66. Nikonowicz, E.P. et al. Preparation Of C-13 And N-15 Labeled Rnas For Heteronuclear Multidimensional Nmr-Studies. *Nucleic Acids Research* **20**, 4507-4513 (1992).

67. Batey, R.T., Inada, M., Kujawinski, E., Puglisi, J.D. & Williamson, J.R. Preparation Of Isotopically Labeled Ribonucleotides For Multidimensional Nmr-Spectroscopy Of Rna. *Nucleic Acids Research* **20**, 4515-4523 (1992).

68. King, G.C., Harper, J.W. & Xi, Z.J. Isotope labeling for C-13 relaxation measurements on RNA. in *Nuclear Magnetic Resonance And Nucleic Acids*, Vol. 261 436-450 (1995).

69. Pervushin, K., Riek, R., Wider, G. & Wüthrich, K. Attenuated T-2 relaxation by mutual cancellation of dipole-dipole coupling and chemical shift anisotropy indicates an avenue to NMR structures of very large biological macromolecules in solution. *Proceedings Of The National Academy Of Sciences Of The United States Of America* **94**, 12366-12371 (1997).

70. Dingley, A.J. & Grzesiek, S. Direct observation of hydrogen bonds in nucleic acid base pairs by internucleotide (2)J(NN) couplings. *Journal Of The American Chemical Society* **120**, 8293-8297 (1998).

71. Theimer, C.A. & Feigon, J. Structure and function of telomerase RNA. *Current Opinion In Structural Biology* **16**, 307-318 (2006).

72. da Silva, M.W. NMR methods for studying quadruplex nucleic acids. *Methods* **43**, 264-277 (2007).

73. Hall, K.B. & Tang, C.G. C-13 relaxation and dynamics of the purine bases in the iron responsive element RNA hairpin. *Biochemistry* **37**, 9323-9332 (1998).

74. Laing, L.G. & Hall, K.B. A model of the iron responsive element RNA hairpin loop structure determined from NMR and thermodynamic data. *Biochemistry* **35**, 13586-13596 (1996).

75. Hoogstraten, C.G., Wank, J.R. & Pardi, A. Active site dynamics in the lead-dependent ribozyme. *Biochemistry* **39**, 9951-9958 (2000).

76. Legault, P., Hoogstraten, C.G., Metlitzky, E. & Pardi, A. Order, dynamics and metal-binding in the lead-dependent ribozyme. *Journal Of Molecular Biology* **284**, 325-335 (1998).

77. Hoogstraten, C.G., Legault, P. & Pardi, A. NMR solution structure of the lead-dependent ribozyme: Evidence for dynamics in RNA catalysis. *Journal Of Molecular Biology* **284**, 337-350 (1998).

78. Schwalbe, H., Buck, J., Furtig, B., Noeske, J. & Wohnert, J. Structures of RNA switches: Insight into molecular recognition and tertiary structure. *Angewandte Chemie-International Edition* **46**, 1212-1219 (2007).

79. Cavanagh, J., Fairbrother, W.J., Palmer, A.G., Rance, M. & Skelton, N.J. *Protein NMR Spectroscopy Principles and Practice*, 885 (Elsevier Academic Press, Burlington, MA, 2007).

80. Abragam, A. *Principles of Nuclear Magnetism*, 599 (Oxford University Press, Inc, New York, NY, 2002).

81. Spiess, H.W. Rotation of Molecules and Nuclear Spin Relaxation. *NMR - Basic Principles and Progress* **15**, 55-214 (1978).

82. Prestegard, J.H., Al-Hashimi, H.M. & Tolman, J.R. NMR structures of biomolecules using field oriented media and residual dipolar couplings. *Quarterly Reviews Of Biophysics* **33**, 371-424 (2000).

83. Korzhnev, D.M., Billeter, M., Arseniev, A.S. & Orekhov, V.Y. NMR studies of Brownian tumbling and internal motions in proteins. *Progress In Nuclear Magnetic Resonance Spectroscopy* **38**, 197-266 (2001).

84. Frank A. L. Anet, D.J.O.L. The shielding tensor. Part I: Understanding its symmetry properties. *Concepts in Magnetic Resonance* **3**, 193-214 (1991).

85. Frank A. L. Anet, D.J.O.l. The shielding tensor part II: Understanding its strange effects on relaxation. *Concepts in Magnetic Resonance* **4**, 35-52 (1992).

86. Hoult, D.I. & Ginsberg, N.S. The quantum origins of the free induction decay signal and spin noise. *Journal Of Magnetic Resonance* **148**, 182-199 (2001).

87. Debye, P. *Polare Molekeln*, (S. Hirzel, Leipzig, 1929).

88. Favro, L.D. Theory Of The Rotational Brownian Motion Of A Free Rigid Body. *Physical Review* **119**, 53-62 (1960).

89. Perrin, F. The Brownien movement of an ellipsoide. - The dielectric dispersion of ellipsoidal molecules. *Journal De Physique Et Le Radium* **5**, 497-511 (1934).

90. Huntress, W.T. *Advances in Magnetic Resonance*, **4**, 1 (Academic Press, New York, NY, 1970).

91. Versmold, H. Time Correlation Functions For Internal And Anisotropic Rotational Motion Of Molecules. *Zeitschrift Fur Naturforschung Part A-Astrophysik Physik Und Physikalische Chemie* **A 25**, 367-& (1970).

92. Lipari, G. & Szabo, A. Model-Free Approach To The Interpretation Of Nuclear Magnetic-Resonance Relaxation In Macromolecules.1. Theory And Range Of Validity. *Journal Of The American Chemical Society* **104**, 4546-4559 (1982).

93. Clore, G.M. et al. Deviations From The Simple 2-Parameter Model-Free Approach To The Interpretation Of N-15 Nuclear Magnetic-Relaxation Of Proteins. *Journal Of The American Chemical Society* **112**, 4989-4991 (1990).

94. Yamazaki, T., Muhandiram, R. & Kay, L.E. Nmr Experiments For The Measurement Of Carbon Relaxation Properties In Highly Enriched, Uniformly C-13,N-15-Labeled Proteins - Application To C-13(Alpha) Carbons. *Journal Of The American Chemical Society* **116**, 8266-8278 (1994).

95. Boisbouvier, J., Wu, Z.R., Ono, A., Kainosho, M. & Bax, A. Rotational diffusion tensor of nucleic acids from C-13 NMR relaxation. *Journal Of Biomolecular Nmr* **27**, 133-142 (2003).

96. d'Auvergne, E.J. & Gooley, P.R. Set theory formulation of the model-free problem and the diffusion seeded model-free paradigm. *Molecular Biosystems* **3**, 483-494 (2007).

97. Clore, G.M., Driscoll, P.C., Wingfield, P.T. & Gronenborn, A.M. Analysis Of The Backbone Dynamics Of Interleukin-1-Beta Using 2-Dimensional Inverse Detected Heteronuclear N-15-H-1 Nmr-Spectroscopy. *Biochemistry* **29**, 7387-7401 (1990).

98. Mandel, A.M., Akke, M. & Palmer, A.G. Backbone Dynamics Of Escherichia-Coli Ribonuclease Hi - Correlations With Structure And Function In An Active Enzyme. *Journal Of Molecular Biology* **246**, 144-163 (1995).

99. Andrec, M., Montelione, G.T. & Levy, R.M. Estimation of dynamic parameters from NMR relaxation data using the Lipari-Szabo model-free approach and Bayesian statistical methods. *Journal Of Magnetic Resonance* **139**, 408-421 (1999).

100. d'Auvergne, E.J. & Gooley, P.R. The use of model selection in the model-free analysis of protein dynamics. *Journal Of Biomolecular Nmr* **25**, 25-39 (2003).

101. Korzhnev, D.M., Orekhov, V.Y. & Arseniev, A.S. Model-free approach beyond the borders of its applicability. *Journal Of Magnetic Resonance* **127**, 184-191 (1997).

102. Jin, D.Q., Andrec, M., Montelione, G.T. & Levy, R.M. Propagation of experimental uncertainties using the Lipari-Szabo model-free analysis of protein dynamics. *Journal Of Biomolecular Nmr* **12**, 471-492 (1998).

103. Chen, J.H., Brooks, C.L. & Wright, P.E. Model-free analysis of protein dynamics: assessment of accuracy and model selection protocols based on molecular dynamics simulation. *Journal Of Biomolecular Nmr* **29**, 243-257 (2004).

104. d'Auvergne, E.J. & Gooley, P.R. Model-free model elimination: A new step in the model-free dynamic analysis of NMR relaxation data. *Journal Of Biomolecular Nmr* **35**, 117-135 (2006).

105. McConnell, H.M. Reaction Rates By Nuclear Magnetic Resonance. *Journal Of Chemical Physics* **28**, 430-431 (1958).

106. Bax, A. et al. Measurement Of Homonuclear And Heteronuclear J-Couplings From Quantitative J-Correlation. in *Nuclear Magnetic Resonance, Pt C*, Vol. 239 79-105 (1994).

107. de Alba, E. & Tjandra, N. Interference between cross-correlated relaxation and the measurement of scalar and dipolar couplings by quantitative J. *Journal Of Biomolecular Nmr* **35**, 1-16 (2006).

108. Tolman, J.R. & Prestegard, J.H. A quantitative J-correlation experiment for the accurate measurement of one-bond amide N-15-H-1 couplings in proteins. *Journal Of Magnetic Resonance Series B* **112**, 245-252 (1996).

109. Fiala, R., Munzarova, M.L. & Sklenar, V. Experiments for correlating quaternary carbons in RNA bases. *Journal Of Biomolecular Nmr* **29**, 477-490 (2004).

110. Yan, J.L., Corpora, T., Pradhan, P. & Bushweller, J.H. MQ-HCN-based pulse sequences for the measurement of (13)C1 '-(1)H1 ', (13)C1 '-N-15, (1)H1 '-N-15, (13)C1 '-(13)C2 ', (1)H1 '-(13)C2 ', (13)C6/8-(1)H6/8, (13)C6/8-N-15, (1)H6/8-N-15, (13)C6-(13)C5, (1)H6-(13)C5 dipolar couplings in C-13, N-15-labeled DNA (and RNA). *Journal Of Biomolecular Nmr* **22**, 9-20 (2002).

111. Boisbouvier, J., Bryce, D.L., O'Neil-Cabello, E., Nikonowicz, E.P. & Bax, A. Resolution-optimized NMR measurement of D-1(CH), D-1(CH) and D-2(CH) residual dipolar couplings in nucleic acid bases. *Journal Of Biomolecular Nmr* **30**, 287-301 (2004).

112. Jaroniec, C.P., Boisbouvier, J., Tworowska, I., Nikonowicz, E.P. & Bax, A. Accurate measurement of N-15-C-13 residual dipolar couplings in nucleic acids. *Journal Of Biomolecular Nmr* **31**, 231-241 (2005).

113. Zidek, L., Wu, H.H., Feigon, J. & Sklenar, V. Measurement of small scalar and dipolar couplings in purine and pyrimidine bases. *Journal Of Biomolecular Nmr* **21**, 153-160 (2001).

114. Vallurupalli, P. & Moore, P.B. Measurement of H2 '-C2 ' and H3 '-C3 ' dipolar couplings in RNA molecules. *Journal Of Biomolecular Nmr* **24**, 63-66 (2002).

115. Griesinger, C., Sorensen, O.W. & Ernst, R.R. Correlation Of Connected Transitions By Two-Dimensional Nmr-Spectroscopy. *Journal Of Chemical Physics* **85**, 6837-6852 (1986).

116. O'Neil-Cabello, E., Bryce, D.L., Nikonowicz, E.P. & Bax, A. Measurement of five dipolar couplings from a single 3D NMR multiplet applied to the study of RNA dynamics. *Journal Of The American Chemical Society* **126**, 66-67 (2004).

117. Miclet, E., Boisbouvier, J. & Bax, A. Measurement of eight scalar and dipolar couplings for methine-methylene pairs in proteins and nucleic acids. *Journal Of Biomolecular Nmr* **31**, 201-216 (2005).

118. Bailor, M.H. et al. Characterizing the relative orientation and dynamics of RNA A-form helices using NMR residual dipolar couplings. *Nature Protocols* **2**, 1536-1546 (2007).

119. Prestegard, J.H., Bougault, C.M. & Kishore, A.I. Residual dipolar couplings in structure determination of biomolecules. *Chemical Reviews* **104**, 3519-3540 (2004).

120. Tolman, J.R. & Ruan, K. NMR residual dipolar couplings as probes of biomolecular dynamics. *Chemical Reviews* **106**, 1720-1736 (2006).

121. Tolman, J.R., Flanagan, J.M., Kennedy, M.A. & Prestegard, J.H. Nuclear Magnetic Dipole Interactions In Field-Oriented Proteins - Information For Structure Determination In Solution. *Proceedings Of The National Academy Of Sciences Of The United States Of America* **92**, 9279-9283 (1995).

122. Ruan, K. & Tolman, J.R. Composite alignment media for the measurement of independent sets of NMR residual dipolar couplings. *Journal Of The American Chemical Society* **127**, 15032-15033 (2005).

123. Gonzalez, A., Nave, C. & Marvin, D.A. Pf1 Filamentous Bacteriophage - Refinement Of A Molecular-Model By Simulated Annealing Using 3.3-Angstrom Resolution X-Ray Fiber Diffraction Data. *Acta Crystallographica Section D-Biological Crystallography* **51**, 792-804 (1995).

124. Onsager, L. The Effects Of Shape On The Interaction Of Colloidal Particles. *Annals Of The New York Academy Of Sciences* **51**, 627-659 (1949).

125. Zweckstetter, M. & Bax, A. Characterization of molecular alignment in aqueous suspensions of Pf1 bacteriophage. *Journal Of Biomolecular Nmr* **20**, 365-377 (2001).

126. Katsaras, J., Harroun, T.A., Pencer, J. & Nieh, M.P. "Bicellar" lipid mixtures as used in biochemical and biophysical studies. *Naturwissenschaften* **92**, 355-366 (2005).

127. Losonczi, J.A. & Prestegard, J.H. Improved dilute bicelle solutions for high-resolution NMR of biological macromolecules. *Journal Of Biomolecular Nmr* **12**, 447-451 (1998).

128. Ottiger, M. & Bax, A. Bicelle-based liquid crystals for NMR-measurement of dipolar couplings at acidic and basic pH values. *Journal Of Biomolecular Nmr* **13**, 187-191 (1999).

129. Li, X.X. & Goodson, B.M. Effects of small neutral molecules on phospholipid bicelle ordering. *Langmuir* **20**, 8437-8441 (2004).

130. Nieh, M.P., Glinka, C.J., Krueger, S., Prosser, R.S. & Katsaras, J. SANS study on the effect of lanthanide ions and charged lipids on the morphology of phospholipid mixtures. *Biophysical Journal* **82**, 2487-2498 (2002).

131. Nieh, M.P. et al. Magnetically alignable phase of phospholipid "Bicelle" mixtures is a chiral nematic made up of wormlike micelles. *Langmuir* **20**, 7893-7897 (2004).

132. Harroun, T.A. et al. Comprehensive examination of mesophases formed by DMPC and DHPC mixtures. *Langmuir* **21**, 5356-5361 (2005).

133. Hare, B.J., Prestegard, J.H. & Engelman, D.M. Small angle x-ray scattering studies of magnetically oriented lipid bilayers. *Biophysical Journal* **69**, 1891-1896 (1995).

134. Katsaras, J. et al. Rarely observed phase transitions in a novel lyotropic liquid crystal system. *Physical Review Letters* **78**, 899-902 (1997).

135. Lundstrom, P. & Akke, M. Off-resonance rotating-frame amide proton spin relaxation experiments measuring microsecond chemical exchange in proteins. *Journal Of Biomolecular Nmr* **32**, 163-173 (2005).

136. Ishima, R. & Torchia, D.A. Extending the range of amide proton relaxation dispersion experiments in proteins using a constant-time relaxation-compensated CPMG approach. *Journal Of Biomolecular Nmr* **25**, 243-248 (2003).

137. Tugarinov, V. & Kay, L.E. Separating degenerate H-1 transitions in methyl group probes for single-quantum H-1-CPMG relaxation dispersion NMR spectroscopy. *Journal Of The American Chemical Society* **129**, 9514-9521 (2007).

138. Eichmuller, C. & Skrynnikov, N.R. A new amide proton R-1 rho experiment permits accurate characterization of microsecond time-scale conformational exchange. *Journal Of Biomolecular Nmr* **32**, 281-293 (2005).

139. Palmer, A.G. NMR characterization of the dynamics of biomacromolecules. *Chemical Reviews* **104**, 3623-3640 (2004).

140. Jarymowycz, V.A. & Stone, M.J. Fast time scale dynamics of protein backbones: NMR relaxation methods, applications, and functional consequences. *Chemical Reviews* **106**, 1624-1671 (2006).

141. Sorensen, M.D., Meissner, A. & Sorensen, O.W. Spin-state-selective coherence transfer via intermediate states of two-spin coherence in IS spin systems: Application to E.COSY-type measurement of J coupling constants. *Journal Of Biomolecular Nmr* **10**, 181-186 (1997).

142. Palmer, A.G., Cavanagh, J., Wright, P.E. & Rance, M. Sensitivity Improvement In Proton-Detected 2-Dimensional Heteronuclear Correlation Nmr-Spectroscopy. *Journal Of Magnetic Resonance* **93**, 151-170 (1991).

143. Cavanagh, J., Palmer, A.G., Wright, P.E. & Rance, M. Sensitivity Improvement In Proton-Detected 2-Dimensional Heteronuclear Relay Spectroscopy. *Journal Of Magnetic Resonance* **91**, 429-436 (1991).

144. Johnson, J.E., Julien, K.R. & Hoogstraten, C.G. Alternate-site isotopic labeling of ribonucleotides for NMR studies of ribose conformational dynamics in RNA. *Journal Of Biomolecular Nmr* **35**, 261-274 (2006).

145. Ying, J.F., Grishaev, A.E. & Bax, A. Carbon-13 chemical shift anisotropy in DNA bases from field dependence of solution NMR relaxation rates. *Magnetic Resonance In Chemistry* **44**, 302-310 (2006).

146. Sklenar, V., Torchia, D. & Bax, A. Measurement Of C-13 Longitudinal Relaxation Using H-1 Detection. *Journal Of Magnetic Resonance* **73**, 375-379 (1987).

147. Ishima, R., Baber, J., Louis, J.M. & Torchia, D.A. Carbonyl carbon transverse relaxation dispersion measurements and ms-mu s timescale motion in a protein hydrogen bond network. *Journal Of Biomolecular Nmr* **29**, 187-198 (2004).

148. Mulder, F.A.A. & Akke, M. Carbonyl C-13 transverse relaxation measurements to sample protein backbone dynamics. *Magnetic Resonance In Chemistry* **41**, 853-865 (2003).

149. Lundstom, P., Hansen, D.F. & Kay, L.E. Measurement of carbonyl chemical shifts of excited protein states by relaxation dispersion NMR spectroscopy: comparison

between uniformly and selectively C-13 labeled samples. *Journal Of Biomolecular Nmr* **42**, 35-47 (2008).

150. Korzhnev, D.M., Tischenko, E.V. & Arseniev, A.S. Off-resonance effects in N-15 T-2 CPMG measurements. *Journal Of Biomolecular Nmr* **17**, 231-237 (2000).

151. Yip, G.N.B. & Zuiderweg, E.R.P. A phase cycle scheme that significantly suppresses offset-dependent artifacts in the R-2-CPMG N-15 relaxation experiment. *Journal Of Magnetic Resonance* **171**, 25-36 (2004).

152. Zweckstetter, M. & Holak, T.A. An adiabatic multiple spin-echo pulse sequence: Removal of systematic errors due to pulse imperfections and off-resonance effects. *Journal Of Magnetic Resonance* **133**, 134-147 (1998).

153. Long, D., Liu, M.L. & Yang, D.W. Accurately probing slow motions on millisecond timescales with a robust NMR relaxation experiment. *Journal Of The American Chemical Society* **130**, 2432-2433 (2008).

154. Sun, X.Y., Zhang, Q. & Al-Hashimi, H.M. Resolving fast and slow motions in the internal loop containing stem-loop 1 of HIV-1 that are modulated by Mg2+ binding: role in the kissing-duplex structural transition. *Nucleic Acids Research* **35**, 1698-1713 (2007).

155. Getz, M.M., Andrews, A.J., Fierke, C.A. & Al-Hashimi, H.M. Structural plasticity and Mg2+ binding properties of RNase PP4 from combined analysis of NMR residual dipolar couplings and motionally decoupled spin relaxation. *Rna-A Publication Of The Rna Society* **13**, 251-266 (2007).

156. Akke, M., Fiala, R., Jiang, F., Patel, D. & Palmer, A.G. Base dynamics in a UUCG tetraloop RNA hairpin characterized by N-15 spin relaxation: Correlations with structure and stability. *Rna-A Publication Of The Rna Society* **3**, 702-709 (1997).

157. D'Souza, V., Dey, A., Habib, D. & Summers, M.F. NMR structure of the 101-nucleotide core encapsidation signal of the Moloney murine leukemia virus. *Journal Of Molecular Biology* **337**, 427-442 (2004).

158. Mulder, F.A.A., de Graaf, R.A., Kaptein, R. & Boelens, R. An off-resonance rotating frame relaxation experiment for the investigation of macromolecular dynamics using adiabatic rotations. *Journal Of Magnetic Resonance* **131**, 351-357 (1998).

159. Guenneugues, M., Berthault, P. & Desvaux, H. A method for determining B-1 field inhomogeneity. Are the biases assumed in heteronuclear relaxation experiments usually underestimated? *Journal Of Magnetic Resonance* **136**, 118-126 (1999).

160. Bax, A. & Davis, D.G. Practical Aspects Of Two-Dimensional Transverse Noe Spectroscopy. *Journal Of Magnetic Resonance* **63**, 207-213 (1985).

161. Korzhnev, D.M., Skrynnikov, N.R., Millet, O., Torchia, D.A. & Kay, L.E. An NMR experiment for the accurate measurement of heteronuclear spin-lock relaxation rates. *Journal Of The American Chemical Society* **124**, 10743-10753 (2002).

162. Massi, F., Johnson, E., Wang, C.Y., Rance, M. & Palmer, A.G. NMR R-1 rho rotating-frame relaxation with weak radio frequency fields. *Journal Of The American Chemical Society* **126**, 2247-2256 (2004).

163. Kumar, A., Grace, R.C.R. & Madhu, P.K. Cross-correlations in NMR. *Progress In Nuclear Magnetic Resonance Spectroscopy* **37**, 191-319 (2000).

164. Palmer, A.G., Grey, M.J. & Wang, C.Y. Solution NMR spin relaxation methods for characterizing chemical exchange in high-molecular-weight systems. in *Nuclear Magnetic Resonance Of Biological Macromolecules, Part C*, Vol. 394 430-465 (2005).

165. Korzhnev, D.M. & Kay, L.E. Probing invisible, low-populated states of protein molecules by relaxation dispersion NMR spectroscopy: An application to protein folding. *Accounts Of Chemical Research* **41**, 442-451 (2008).

166. Palmer, A.G. & Massi, F. Characterization of the dynamics of biomacromolecules using rotating-frame spin relaxation NMR spectroscopy. *Chemical Reviews* **106**, 1700-1719 (2006).

167. Trott, O. & Palmer, A.G. Theoretical study of R-1p rotating-frame and R-2 free-precession relaxation in the presence of n-site chemical exchange. *Journal Of Magnetic Resonance* **170**, 104-112 (2004).

168. Trott, O., Abergel, D. & Palmer, A.G. An average-magnetization analysis of R-1 rho relaxation outside of the fast exchange. *Molecular Physics* **101**, 753-763 (2003).

169. Abergel, D. & Palmer, A.G. On the use of the stochastic Liouville equation in nuclear magnetic resonance: Application to R-1 rho relaxation in the presence of exchange. *Concepts In Magnetic Resonance Part A* **19A**, 134-148 (2003).

170. Miloushev, V.Z. & Palmer, A.G. R-1p relaxation for two-site chemical exchange: General approximations and some exact solutions. *Journal Of Magnetic Resonance* **177**, 221-227 (2005).

171. Trott, O. & Palmer, A.G. R-1 rho relaxation outside of the fast-exchange limit. *Journal Of Magnetic Resonance* **154**, 157-160 (2002).

172. Korzhnev, D.M., Orekhov, V.Y. & Kay, L.E. Off-resonance R1(p) NMR studies of exchange dynamics in proteins with low spin-lock fields: An application to a fyn SH3 domain. *Journal Of The American Chemical Society* **127**, 713-721 (2005).

173. Pelupessy, P., Chiarparin, E. & Bodenhausen, G. Excitation of selected proton signals in NMR of isotopically labeled macromolecules. *Journal Of Magnetic Resonance* **138**, 178-181 (1999).

174. Pelupessy, P. & Chiarparin, E. Hartmann-Hahn polarization transfer in liquids: An ideal tool for selective experiments. *Concepts In Magnetic Resonance* **12**, 103-124 (2000).

Chapter 2. Insight into the CSA Tensors of Nucleobase Carbons in RNA Polynucleotides from Solution Measurements of RCSAs

2.1 Introduction

Circulation of current within electronic clouds of molecules gives rise to a local magnetic field at nuclei of interest that fluctuates as molecules tumble relative to the applied magnetic field. The orientational dependence of this local field can be mathematically described by five elements of a 2nd rank chemical shift anisotropy (CSA) tensor. Knowledge of CSA tensors is required to account for CSA relaxation mechanisms. This proves to be important for a range of biomolecular NMR applications including the interpretation of spin relaxation data in terms of angular constraints[1-4] and dynamical parameters[5,6] and in analyzing TROSY effects[7]. Knowledge of CSA tensors is also necessary for structure determination by solid-state NMR[8-10] and for interpreting spectra of partially oriented samples in which anisotropic chemical shift interactions no longer average to zero[11-15].

Of particular interest in nucleic acids are the CSAs of the nucleobase carbons adenine C2, pyrimidine C5 and C6, and purine C8 (Figure 2.1A). These C–H carbons are essential spins for probing the fast dynamics of nucleic acids by spin relaxation measurements[16-21]. Unlike amide nitrogens in proteins, imino ^{15}N relaxation data is only available for half the residues in nucleic acids (guanine and uridine/thymine) and seldom for flexible sites of interest due to rapid exchange of imino protons with solvent[22]. The large CSA of these aromatic carbons together with the often highly anisotropic tumbling of nucleic acids makes knowledge of all five CSA tensor elements crucial for these studies especially when working at higher magnetic fields.
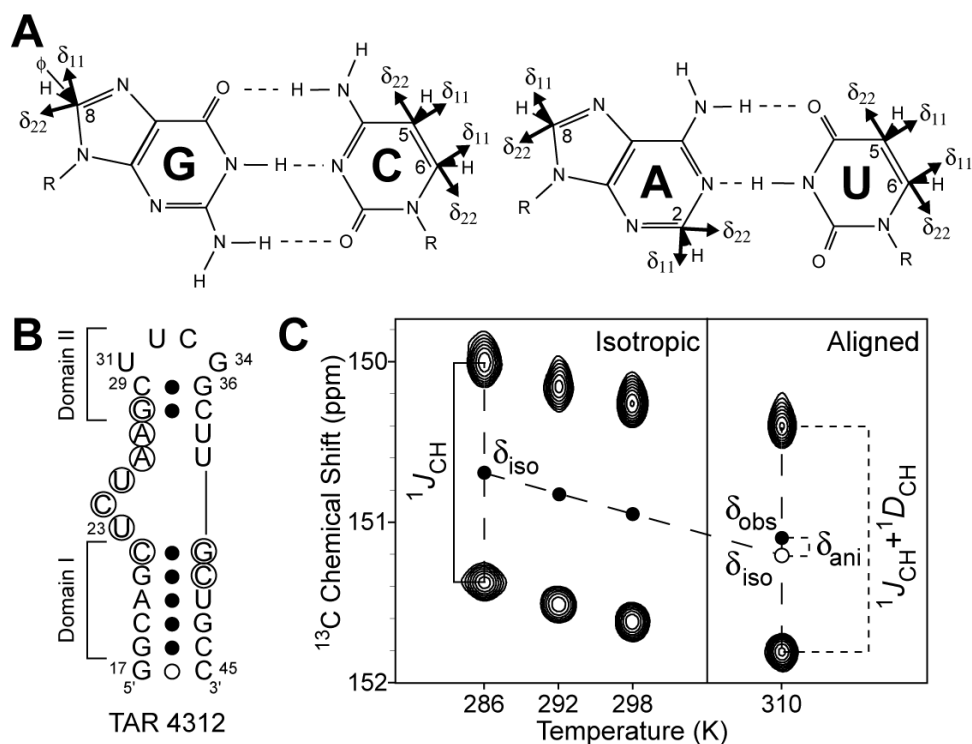
Figure 2.1. Simultaneous measurements of nucleobase RDCs and RCSAs in TAR4312 RNA. (A) Watson-Crick base-pairs showing the nucleobase carbons targeted for RCSA measurements along with the definition of the angle Φ (shown as positive values) used in Table 2.1 to define the orientation of the δ_{11}/δ_{22} CSA principal axes. (B) Secondary structure of TAR4312 in which A22-U40, G26-C39 and the CUGGGA hairpin loop in wt-TAR are replaced with C22-G40, A26-U39, and a UUCG loop, respectively. Filled circles denote Watson-Crick hydrogen bonding as inferred from a J_{NN}-COSY experiment[23]. Residues that experience the largest bicelle-induced perturbations in isotropic ^{13}C chemical shifts are circled. (C) Measurements of base RDCs ($^{1}D_{CH}$) and RCSAs (δ_{ani}) using C2 in A26 as an example. Uniformly ^{15}N/^{13}C-labeled TAR4312 was prepared by in vitro transcription. NMR samples contained ~0.5 mM RNA, 15 mM sodium phosphate pH 6.4, 0.1 mM EDTA, and 25 mM NaCl in D_2O. NMR experiments were carried out on a Bruker AMX 600 MHz spectrometer equipped with a cryogenic probe.

To date, only one solid-state NMR study of RNA mononucleotide powders has reported experimental values for the principal components of the nucleobase carbon CSAs (Table 2.1, SS)[24]. However, the CSA orientations were obtained using density functional theory (DFT) calculations on simplified mononucleotides. To our knowledge, no experimental data has been obtained so far that reports on the orientation of the carbon nucleobase CSAs. Two other nucleobase carbon CSA sets derived by DFT calculations on simplified mononucleotides and which include both principal values and orientations have also been reported in the literature (Table 2.1, DFT1[25] and DFT2[26]). Though widely used in the analysis of ^{13}C relaxation data, the validity of these

mononucleotide CSAs in the context of RNA polynucleotides under solution conditions remains to be established. This is important given the well-known dependence of CSAs on intermolecular interactions[25,27,28] and involvement of nucleobases in hydrogen-bonding and stacking interactions. Indeed, a recent ^{13}C relaxation study of RNA dynamics alludes to potential deviations from the mononucleotide CSAs. In particular, difficulties were encountered when using the SS CSAs in analyzing ^{13}C relaxation data measured at high (17.6 T) but not low (11.7 T) magnetic fields[21]. Furthermore, the discrepancies in the reported CSA magnitudes (CSAa = $(3/2 \cdot (\delta_{11}^2 + \delta_{22}^2 + \delta_{33}^2))^{1/2}$, where δ_{ii} are the principal values of the traceless CSA tensor) for purine C8 and pyrimidine C6 are sufficiently large to impart undesirable uncertainty in the dynamical interpretation of relaxation data (Table 2.1).

Here, we have measured the manifestation of nucleobase carbon CSAs as residual perturbations in chemical shifts that can be observed when a weak degree of RNA alignment is imposed[13-15,29-31]. Such residual chemical shift anisotropies (RCSAs) have previously been used to determine CSA tensors for carbonyl carbons, amide nitrogens, and amide protons in proteins[13,29] and more recently for sugar carbons in A-form RNA helices[15]. Since RCSAs depend on the orientation of CSA tensors relative to the order tensor governing alignment, they also provide long-range orientational constraints[14,32] for structure determination, much like residual dipolar couplings (RDCs)[33,34]. Having an abundance of such long-range constraints is particularly important for structure determination of extended and proton deficient nucleic acids.

Atom (#)	Source	δ_{11} (ppm)	δ_{22} (ppm)	δ_{33} (ppm)	ϕ (deg)	CSA$_a$ (ppm)	rmsd (Hz)	Q (%)
A C2 (1)	SS	84.7	3.6	-88.3	-3.0	149.9	1.8 (1.4)	44 (36)
	DFT1	84.0	1.0	-85.0	-3.8	146.4	1.6 (1.2)	40 (31)
	DFT2	82.1	1.8	-83.9	-3.6	143.8	1.6 (1.2)	41 (32)
C C5 (4)	SS	80.1	-1.2	-78.9	-11.0	137.7	1.6 (1.4)	43 (38)
	DFT1	82.0	-11.0	-71.0	-9.6	133.5	1.9 (1.7)	55 (49)
	DFT2	80.6	-11.2	-69.4	-8.9	131.0	1.9 (1.8)	56 (53)
	RCSA	107.4 ± 21.4	-18.0 ± 24.2	-89.4 ± 7.5	38.2 ± 13.3	172.6 ± 21.2	0.6	14
	Calc-4	± 20.3	± 19.0	± 7.4	(-90 – 90)	± 17.7	--	--
U C5 (2)	DFT1	80.3	-7.6	-72.7	10.7	133.0	1.7 (1.6)	51 (48)
	DFT2	76.5	-7.0	-69.5	10.6	126.9	2.0 (1.9)	63 (60)
C C6 (2)	SS	98.4	9.1	-107.5	31.0	178.8	0.9 (1.0)	19 (22)
	DFT1	94.0	-7.0	-87.0	19.8	157.1	1.4 (0.9)	34 (22)
	DFT2	98.3	14.2	-112.5	26.9	183.9	1.4 (1.4)	30 (30)
U C6 (2)	DFT1	102.7	-14.4	-88.3	19.3	166.8	0.6 (0.2)	14 (5)
	DFT2	105.4	1.8	-107.2	28.3	184.1	1.3 (1.3)	30 (30)
A C8 (1)	SS	78.3	-1.6	-76.7	-27.0	134.3	0.5 (0.2)	14 (6)
	DFT1	71.3	-13.6	-57.7	-21.2	113.6	0.1 (0.1)	3 (3)
	DFT2	72.5	-3.5	-69.0	-29.4	122.8	0.1 (0.2)	3 (6)
G C8 (5)	SS	76.0	3.0	-79.0	-28.0	134.3	1.7 (1.4)	48 (40)
	DFT1	71.7	-15.4	-56.3	-21.6	113.2	1.4 (1.2)	49 (42)
	DFT2	73.1	-9.8	-63.3	-30.4	119.0	1.5 (1.2)	49 (39)
	RCSA	97.8 ± 11.8	-37.1 ± 12.2	-60.7 ± 4.0	-1.8 ± 6.9	148.1 ± 12.8	0.6	16
	Calc-5	± 16.9	± 19.3	± 6.9	(-90 – 90)	± 14.7	--	--

Table 2.1. Analysis of nucleobase carbon CSAs using RCSAs measured in TAR4312. The number of RCSAs measured is shown in parenthesis next to the residue/carbon type. CSA parameters are from solid state NMR (SS)[24], DFT calculations (DFT1, DFT2)[25,26], RCSA derived values (RCSA), and the standard deviations obtained when using synthetic RCSAs (Calc). The root-mean-square-deviation (rmsd) and quality factor (Q)[15,35] are calculated between measured and back-calculated RCSAs RDC-validated domain structures. The best-fit results (rmsd and Q-factor) following ±5%, ±0.1, and ca. 6° variations in the order tensor GDO[36], order tensor asymmetry η, and orientation of individual bases are shown in parenthesis. For the single adenine C2 and C8 RCSA, only the difference between the measured and predicted values was used to compute rmsd and Q.

2.2 Results and Discussion

Our study was carried out on a uniformly $^{13}C/^{15}N$ labeled mutant of the transactivation response element (TAR4312) RNA (Figure 2.1B) which was partially aligned using a 5% (w/v) DHPC:DMPC (3:1) bicelle medium[33,37] that forms an aligned liquid crystalline phase at temperatures above 298 K. At or below room temperature the bicelles form an isotropic phase, allowing the measurement of the isotropic chemical shifts, their temperature dependences, and scalar couplings. One bond C–H splittings and 13C chemical shifts were measured simultaneously from the difference and average frequency respectively of the upfield and down field components of the $\{^{13}C\}$–^1H doublet (Figure 2.1C). These components were measured in separate sub-spectra using 2D ^{13}C–^1H S_3CT HSQC experiments[38,39]. The RDCs were computed from the difference in C–H splittings measured in aligned (T = 310 K) and isotropic (T = 292 K) phases (Figure 2.1C). Due to the temperature dependence of isotropic chemical shifts (δ_{iso}), the RCSAs could not simply be computed from the difference in chemical shifts measured at 298 K and 310 K. Rather, the value of δ_{iso} at 310 K ($\delta_{iso,bicelle}^{310K}$) was determined by linearly extrapolating δ_{iso} measured in the isotropic phase at 286 K, 292 K and 298 K to 310 K (Figure 2.1C and Figure 2.2A). This approach was previously used to measure RCSAs in the protein ubiquitin[13]. The chemical shifts measured in the aligned phase ($\delta_{obs,bicelles}^{310K}$ = $\delta_{iso,bicelle}^{310K}$ + δ_{ani}^{310K}) were also corrected to account for changes in the lock frequency due to quadrupolar ^2H splittings (7.6 Hz). The RCSAs were then computed by subtracting $\delta_{iso,bicelle}^{310K}$ from $\delta_{obs,bicelles}^{310K}$. The RDCs and RCSAs measured in TAR4312 are listed in Table 2.2.
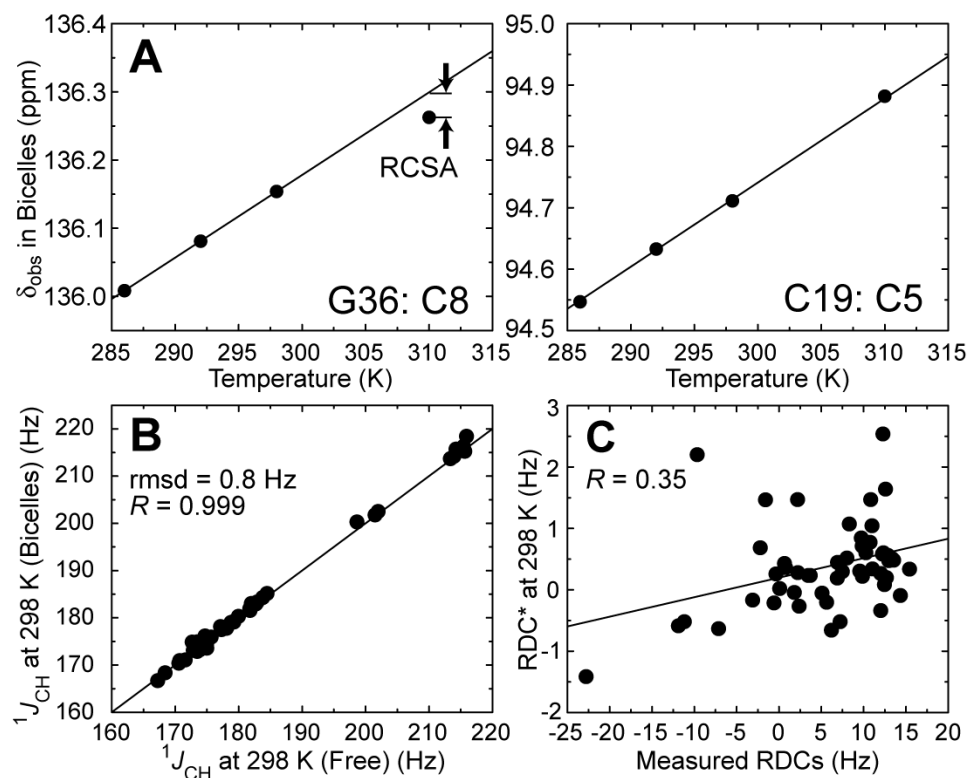
Figure 2.2. Measurement of nucleobase RCSAs in TAR4312 weakly aligned in a bicelle medium. (A) Measurement of RCSAs in bicelles using a linear extrapolation of the temperature dependence of isotropic ^{13}C chemical shifts. Shown are two examples from domains I and II. (B, C) Lack of TAR4312 alignment in bicelles at ≤310 K. (B) Correlation plot between one bond C–H splittings measured at 298 K in the presence and absence of bicelles. (C) Correlation plot between measured RDCs (RDC = 310 – 298 K) and "would be RDCs" (RDC* = 298 K in bicelles – 298 K without bicelles).

Besides assuming a linear temperature dependence for δ_{iso} over 286–310 K, which was observed for all carbons examined (e.g. Figure 2.2A), the latter approach for measuring RCSAs assumes no TAR4312 alignment at T ≤ 298 K. Any unaccounted for residual TAR4312 alignment would lead to underestimation of the RCSAs and ultimately their associated CSAs. Negligible TAR4312 alignment at ≤ 298 K was confirmed based on a number of observations. First, no quadrupolar ^2H splittings were observed at ≤ 298 K. Second, the differences between C–H splittings measured in the presence and absence of bicelles at 298 K (root-mean-square-deviation, rmsd = 0.8 Hz, Figure 2.2B) are within the estimated measurement uncertainty (0.9 Hz, see legend of Table 2.2). Finally, a poor correlation (R = 0.35) is observed between the measured RDCs and "would be RDCs" at 298 K (Figure 2.2C).
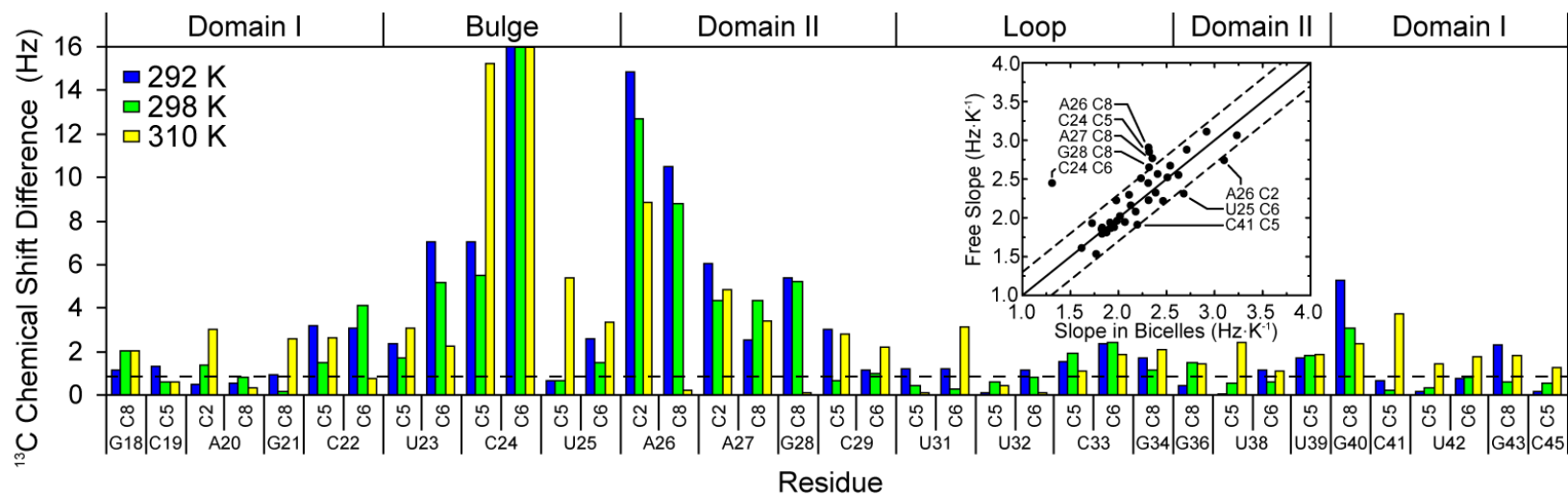
Figure 2.3. Residue specific bicelle-induced perturbations in isotropic ^{13}C chemical shifts in TAR4312. Shown are the differences between C2 (adenine), C5 (pyrimidine), C6 (pyrimidine) and C8 (purine) chemical shifts measured in the presence and absence of bicelles at T = 292 K, 298 K, and 310 K. (Inset) Corresponding slopes of the ^{13}C chemical shift versus temperature.

Residue	Atom / Vector	RCSA (Hz)	RDC (Hz)
G18	C8 / C8-H8	4.1±0.8	-1.4±1.4
C19	C5 / C5-H5	0.8±0.8	-9.2±1.4
A20	C2 / C2-H2	-2.5±0.8	13.6±1.4
A20	C8 / C8-H8	-3.6±0.8	13.5±1.4
G21	C8 / C8-H8	-3.5±0.8	11.6±1.4
C22	C5 / C5-H5	-4.9±0.8	12.7±1.4
C22	C6 / C6-H6	-5.1±0.8	2.3±1.4
G28	-- / C1'-H1'	--	-14.9±1.4
G28	C8 / C8-H8	-3.2±0.8	13.5±1.4
C29	C5 / C5-H5	-6.4±0.8	12.8±1.4
C29	C6 / C6-H6	-7.4±0.8	11.7±1.4
U31	-- / C1'-H1'	--	-0.2±1.4
U31	C5 / C5-H5	-7.6±0.8	13.7±1.4
U31	C6 / C6-H6	-7.4±0.8	11.9±1.4
U32	-- / C1'-H1'	--	4.6±1.4
C33	-- / C1'-H1'	--	-0.4±1.4
G34	-- / C1'-H1'	--	7.5±1.4
G34	C8 / C8-H8	-6.9±0.8	9.0±1.4
G36	C8 / C8-H8	-5.5±0.8	13.2±1.4
C37	-- / C1'-H1'	--	3.2±1.4
G40	C8 / C8-H8	-2.1±0.8	3.6±1.4
C41	C5 / C5-H5	-5.9±0.8	7.5±1.4
U42	C5 / C5-H5	-3.1±0.8	1.2±1.4
U42	C6 / C6-H6	-4.7±0.8	13.5±1.4
G43	C8 / C8-H8	-5.6±0.8	16.7±1.4
C44	-- / C1'-H1'	--	14.5±1.4

Table 2.2. RDCs and RCSAs in TAR4312 measured at a ^{1}H spectrometer frequency of 600 MHz. The RDC measurement uncertainty was obtained by multiplying the observed rmsd between splittings measured at 292 and 298 K (0.9 Hz) by $2^{1/2}$. The RCSA measurement uncertainty was obtained by propagating the errors in $\delta_{obs,bicelle}^{310K}$ and $\delta_{iso,bicelle}^{310K}$. The $\delta_{obs,bicelle}^{310K}$ uncertainty (0.3 Hz) was obtained from the rms of residuals in the three point linear-fit of δ_{iso} versus temperature (Figure 2.2A). The $\delta_{iso,bicelle}^{310K}$ uncertainty was obtained using the following procedure. Perfect synthetic data corresponding to δ_{iso} at 286 K, 292 K, and 298 K was generated. Each data point was then perturbed by an amount chosen randomly from a Gaussian distribution centered at zero with the standard deviation set to the rms in the three-point residuals. Linear extrapolation of the resulting data set to 310 K was then used to compute an error in $\delta_{iso,bicelle}^{310K}$. The error was obtained from the standard deviation in $\delta_{iso,bicelle}^{310K}$ following thousands of such runs (0.7 Hz).

As shown in Figure 2.3, we observed significant bicelle-induced perturbations in δ_{iso} (rmsd = 8.4 / 7.2 / 5.5 Hz at 292, 298, 310 K) which precluded measurements of RCSAs as the difference between chemical shifts observed in the presence and absence of bicelles.

The latter approach was previously used to measure ^{31}P RCSAs in DNA[14] and 13C RCSAs in RNA[15] but using the Pf1-phage[40,41]. The bicelle-induced perturbations in TAR4312 are particularly pronounced for structurally unstable regions (Figure 2.1B, circled residues) including the bulge (U23, C24, and U25) and two neighboring adenines in domain II (A26 and A27) that, based on J_{NN}-COSY experiments,[23] are not involved in A-U Watson-Crick hydrogen bonding (data not shown). Interestingly, these residues also have carbon chemical shifts that have markedly different temperature dependencies in the presence and absence of bicelles (Figure 2.3, inset). These perturbations likely arise from changes in the structural dynamics of TAR4312 due to transient contacts with the bicelles. Similar perturbations have been reported for fraying terminal residues in a duplex RNA in Pf1-phage[15]. These results underscore the importance of accommodating ordering media induced changes in δ_{iso} when measuring RCSAs and suggest that the bicelle medium can affect the conformational dynamics of flexible RNAs.

The RCSA (δ_{ani}) measured for a carbon nucleus k depends on the magnitude and orientation of the kth CSA tensor (δ_{ij}^{k}) relative to the order tensor (S_{ij}) governing alignment[42]:

$$\delta_{ani}(k) = \left(\delta_{obs} - \delta_{iso}\right) = \frac{2}{3} \sum_{ij=\{x,y,z\}} S_{ij}\delta_{ij}^{k} \qquad . \qquad [2.1]$$

To interpret RCSAs using Equation [2.1], we first used RDCs to validate domain structures for TAR4312 and determine their order tensors. The domain structures comprised idealized A-form helices and a previous X-ray structure[43] of the U31U32C33G34 tetraloop (Figure 2.1B). The local structure of these domains has previously been validated using RDCs measured in free TAR[44] and for TAR bound to three (in the case of domain I) and four (in the case of domain II) distinct ligands that bind to the bulge and neighboring residues without affecting the remaining local helical structure[45-47]. The 108 RDCs belonging to TAR residues that coincide with those of

TAR4312 fit (using SVD[42]) the above domain structures with an overall rmsd (normalized to reflect the TAR4312 degree of order) of 1.5 Hz (Figure 2.4A). Values are back-calculated using best-fit order tensors determined independently for each domain using the assumed model domain structures and a modified version of ORDERTEN_SVD[42]. Only RDCs belonging to TAR residues that coincide with those of TAR4312 were included in the fit. As shown in Figure 2.4B, the agreement between the RDCs measured in TAR4312 and these model structures is equally good with the overall rmsd in the SVD fit[42] (1.5 Hz) being approximately equal to the estimated RDC measurement uncertainty (1.4 Hz, see legend of Table 2.2). A total 13/13 RDCs in domains I/II with condition numbers of 3.7/2.6 were used in the latter SVD fit. The idealized A-form helices were generated using Insight II (Molecular Simulations, Inc.) with propeller twist angles set to -15°[48].

Next, we examined the agreement between the measured RCSAs and values back-calculated using Equation 1, the RDC-validated domain structures, RDC-derived domain-specific order tensors and each of the DFT1, DFT2 and SS nucleobase carbon CSAs. The analysis that follows assumed uniform CSAs from site to site and that internal motions uniformly scale all of the measured RDCs (and derived order tensors) and RCSAs by a similar amount. Furthermore, the bond lengths reported by Cornell et. al.[49] ($r_{CH(base)}$ = 1.08 Å and $r_{CH(ribose)}$ = 1.09 Å) were assumed in the RDC-determination of the order tensors. Any systematic under-/over-estimation of these bond lengths will lead to under-/over-estimation of the degree of order and hence predicted RCSAs. It should be noted at the outset that most of the DFT1, DFT2 and SS CSA tensor elements are in very good agreement with one another especially the orientations (Table 2.1). In all cases, the most shielded component (δ_{33}) is oriented perfectly along the base normal and the least shielded component (δ_{11}) close to coincident ($\Phi < 30°$) with the corresponding C–H bond (Table 2.1). However, for a subset of carbons, particularly pyrimidine C6 and purine C8, large differences in the principal values are observed leading to differences in CSAa as large as 27 ppm.
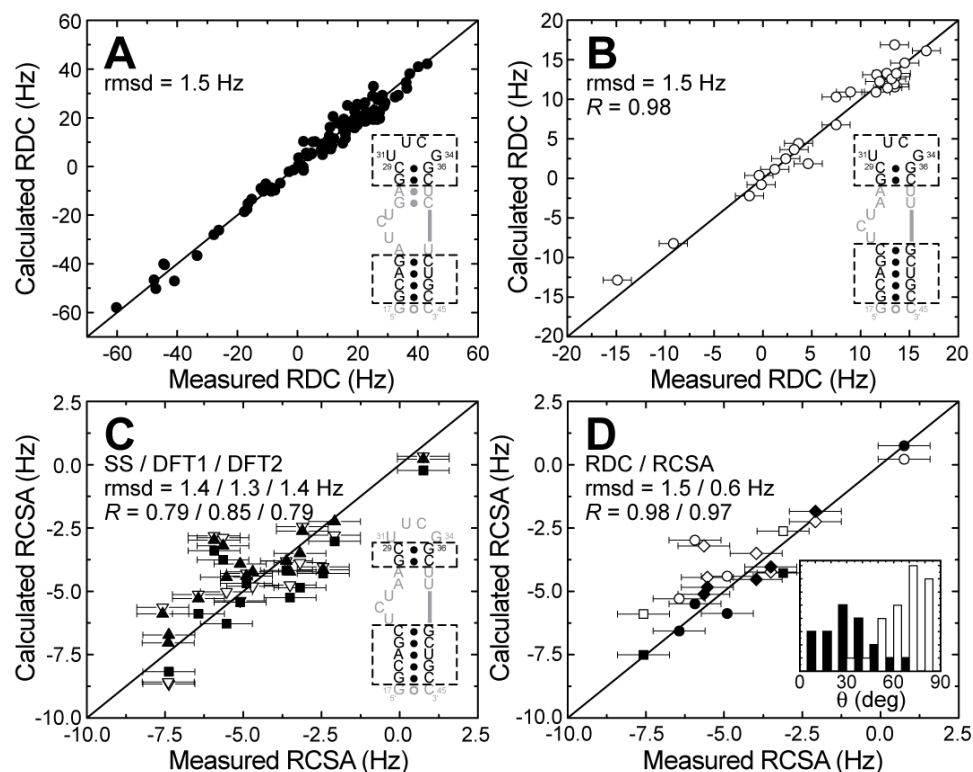
Figure 2.4. Evaluating nucleobase CSA tensors using RCSAs. (A, B) RDC-based validation of model structures for the two TAR4312 domains comprising idealized A-form helices for hydrogen bonded Watson-Crick residues and an X-ray structure[43] for the UUCG tetraloop. (C) Correlation plot between measured RCSAs and values back-calculated using the RDC-derived order tensor, and SS (filled squares), DFT1 (filled triangles), and DFT2 (open triangles) CSAs. (D) Same as in (B) for cytosine C5 (filled circles) and guanine C8 (filled diamonds) when using the RCSA-fitted CSAs. The correlation of uridine C5 RCSAs when assuming the RCSA-derived cytosine C5 CSA is shown with filled squares. Agreement with DFT1 is shown using open symbols. (Inset) The angle (θ) between the principal axis of the order tensor (S_{zz}) and C–H RDC vectors (in white) or δ_{33} CSA axis (in black) in TAR4312.

Shown in Figure 2.4C are correlation plots showing the RCSAs measured in Watson-Crick base-pairs and values back-calculated using the mononucleotide CSAs. Similar overall agreement is observed for the three CSA sets with the best agreement observed for DFT1 and SS followed by DFT2. Similar agreement was observed when combining the RDCs and RCSAs in the SVD fit ($\text{rmsd}_{RDC}(Hz)/\text{rmsd}_{RCSA}(Hz)$= 1.5/1.3, 1.5/1.2, 1.4/1.4 for SS, DFT1 and DFT2, data not shown). Although the observed agreement (rmsd = 1.3 – 1.4 Hz) is favorable considering that the differences between measured and predicted RCSAs are almost an order of magnitude smaller than the

predicted RCSA range (ca. -10 – 10 Hz), the differences remain higher than the estimated RCSA measurement uncertainty (0.8 Hz, see legend of Table 2.2).

Shown in Table 2.1 is the rmsd and quality factor (Q)[15,35] describing the level of agreement between the measured and predicted RCSAs for individual carbon types. We focus on cytosine C5 and guanine C8 for which more than two RCSA measurements were available (Table 2.1). Poor agreement is observed for these carbons with all three mononucleotide CSAs (Q > 40%). This is the case even after allowing the input order tensor parameters to vary within their experimental uncertainty (±5% and ±0.1 variations in the generalized degree of order, GDO[36], and asymmetry η, respectively) and allowing the orientation of individual nucleobases to vary randomly by ca. 6° (Table 2.1, shown in parentheses). The latter was used to account for structural noise and was accomplished by applying random Euler rotations independently to each base. This suggests that some of the scatter in Figure 2.4B is due to deviations from the assumed mononucleotide guanine C8 and cytosine C5 CSAs. Indeed, better agreement is observed when excluding the latter RCSAs from the fit of Figure 2.4C (rmsd (Hz)/R = 1.2/ 0.95; 1.1 / 0.88; and 1.2/0.96 for SS, DFT1, and DFT2, respectively).

To this end, we carried out an exhaustive three-parameter (δ_{11}, δ_{22} and Φ) grid search to see if we could find CSA tensors that fit the cytosine C5 and guanine C8 RCSAs to within experimental uncertainty. In both cases, the δ_{33} orientation (two parameters) was assumed normal to the base plane. CSA tensors were accepted if they reproduced (using Equation 1 and the RDC-derived order tensors) the measured RCSAs to within a cut-off that includes the uncertainty in the measured RCSA (0.8 Hz) and RDC-derived order tensor (±5% and ±0.1 variations in GDO and η, respectively). These calculations were repeated millions of times each time following application of ca. 6° random Gaussian perturbations in the orientation of each base to account for structural noise. The average and standard deviations in the CSA parameters over the accepted solutions are listed in Table 2.1 ("RCSA"). For both cytosine C5 and guanine C8, CSA parameters could be obtained that reproduce all measured RCSAs to within

experimental precision (rmsd < 0.8 Hz, Q < 20%, Figure 2.4C and Table 2.1). Differences are however observed between the RCSA-derived principal values and Φ angles and the corresponding mononucleotide values (Table 2.1). We avoid interpreting the differences in Φ since simulations using synthetic C5 and C8 RCSAs show this angle to be intrinsically difficult to define on the basis of the RCSAs measured in TAR4312 (Table 2.1, Calc-4 and Calc-5). This is in part due to placement of the δ_{11} direction close to within the axially symmetric $S_{xx} - S_{yy}$ plane of the order tensor. Nevertheless, we note that the deviations in Φ from the corresponding mononucleotide values are larger for cytosine C5 (~50°) compared to guanine C8 (~24°).

In contrast to Φ, simulations employing synthetic data show that the cytosine C5 and guanine C8 CSA principal values can be defined to a useful level of precision (~±16 ppm) using the measured RCSAs (Table 2.1, Calc-4 and Calc-5, respectively). The mean cytosine C5 CSA magnitude obtained using the RCSA grid search (CSAa = 173 ± 21 ppm) is significantly higher than all of the values reported for mononucleotides (131 – 138 ppm). In contrast, the RCSA-derived CSAa value for guanine C8 (148 ± 13 ppm) is only slightly higher than the mononucleotide values and within experimental uncertainty equal to that of SS (134 ppm).

A number of factors suggest that the observed differences between the mononucleotide C5 CSAa values and that derived here using RCSAs reflect genuine differences in C5 electron density in the mononucleotide and polynucleotide base. First, we note that the RCSA-derived CSA parameters for cytosine C5 leads to a better fit between the measured and back-calculated uridine C5 RCSAs (Figure 2.4C). The rmsd decreases from 1.6 Hz to 0.6 Hz and the Q-factor from 48% to 14%. It is also noteworthy that the larger RCSA-derived C5 CSAa value is comparable to that reported for pyrimidine C6 by SS and DFT2 (179 – 184 ppm). Unlike C5, a good fit is observed between the four measured C6 RCSAs and the SS and DFT2 CSAs (Table 2.1). Our results therefore suggest that the pyrimidine C5 and C6 have similar CSAa values. Second, it is noteworthy that previous DFT calculations have shown that the CSA

principal values of cytosine C5 are particularly sensitive to intermolecular interactions [24]. Finally, the larger cytosine C5 CSAa value obtained here may explain some of the anomalously high order parameters (S2 ~ 1) recently obtained for a number of C5 sites in RNA Watson-Crick base pairs.[21] These large order parameters could have arisen from use of what would have been an underestimated SS input CSAa value in analyzing the C5 relaxation data.[21]

Recently, two additional studies have sought to shed light on the nucleobase carbon CSA tensors.[50,51] Bax and coworkers followed a similar strategy to the one proposed and measured RCSAs of the nucleobase carbons of an A-form RNA and a B-form DNA. In addition to this, however, they measured cross-correlated relaxation rates between the ^{13}C CSA and CH dipolar interactions, which is dependent on the angles between the principle components of the two interactions. This effectively provides an additional restraint on the angle ϕ within the base plane, which we were unable to refine. They were able to obtain highly accurate values for all of the protonated base carbons and arrived at CSAa values of 144 ± 1 ppm and 133 ± 1 ppm cytosine C5 and guanine C8, respectively. In the other study, Brumovska et al.[51] investigated the effect that the glycosidic bond angle, χ, has on the CSA tensors using DFT calculations and an Iglo II basis set. In their work, they found similar CSAa values of 140.4 ppm and 127.7 ppm. They note however, that their particular technique underestimates the magnitude by about 4 ppm. While the values from these two studies are considerably lower than those determined from TAR4312, both note the significant effect that the CH bond length has on measured CSA tensors and would lead to an overestimation of about 7% when using bond lengths of 1.08 and 1.09 Å for nucleobase and ribose bonds, respectively. Correcting for this, our values for cytidine and guanine become 161 ± 20 and 138.5 ± 12 ppm and are in very good agreement with both studies. Interestingly, Brumovska et al. also note that the pyrimidine C6 and purine C8 nuclei are highly sensitive to rotations about the glycosidic bond, whereas quaternary carbons C4 and C5 in purines are generally insensitive and are potentially a better choice as a structural restraint.

In contrast to most spin relaxation measurements, which depend quadratically on CSAa, RCSAs scale linearly with the CSA principal values. While this makes RCSA-based definition of the CSA tensor more difficult, it also means that the structural interpretation of RCSAs can tolerate a greater deal of CSA uncertainty. Indeed, SS, DFT1 and DFT2 CSAs all yield an overall RCSA fit to the TAR4312 structure (rmsd < 1.4 Hz, Figure 2.4C) that is approximately an order of magnitude smaller than the predicted RCSA range (-10 – 10 Hz). This suggests that all of the measured RCSAs, including adenine C2 and C8, can be translated into useful "loose" structural constraints even after accommodating some uncertainty in the CSAs. Such uncertainty would also take into account potential site-specific variations in the CSA. What makes nucleobase RCSAs particularly attractive structural parameters is that they provide constraints on the δ_{33} principal direction which is oriented normal to the base along a direction seldom sampled directly by RDC interaction vectors, as shown in the inset of Figure 2.4C for TAR4312.

To illustrate the utility of RCSAs as structural constraints, we examined the range of cytosine and guanine base orientations that are allowed by RDC and RDC+RCSA measurements. For each case, a domain-specific order tensor was derived using RDCs excluding values belonging to the residue examined. Next, all allowed base orientations were interrogated for their ability to back calculate RDCs or both RDC+RCSAs. Base orientations were accepted if the differences between the measured and predicted RDCs (or both RDCs and RCSAs) were smaller than a specified cut-off comprising errors in the measurement (1.4 Hz and 0.8 Hz for RDCs and RCSAs, respectively), order tensor (±5%and ±0.1 variations in GDO and η, respectively), and CSA tensor (±10%, ±0.15, and ±20° variations in CSAa, η, and Φ, respectively). The input CSA parameters were centered around the RCSA-derived values (RCSA, Table 2.1) but their uncertainty leads to CSAa values that span those of DFT1, DFT2, and SS. Similar results were also obtained when centering the CSA parameters around the DFT1 or SS values (data not shown). As shown in Figure 2.5A, a single C8–H8 RDC only partially restricts the allowed orientations of the G36 nucleobase. This is because in addition to the taco-

shaped continuous distribution of orientations[52], rotations about the C8–H8 RDC bond vector itself are allowed leading to poor definition of the orientation normal to the base plane. Including an orthogonal constraint from a single C8 RCSA measurement greatly helps reduce the allowed orientations even after allowing for the aforementioned CSA uncertainty. As would be expected, the orientational solutions cluster closely around the poles of the map and hence orientation of the base in the RDC-validated A-form structure. For C22, the addition of a single C5 RCSA to two RDCs also substantially restricts the allowed continuous orientational solutions (Figure 2.5B). Similar results were obtained for all other C2, C5, C6 and C8 RCSAs when using any of the mononucleotide CSAs and similar CSA uncertainty (data not shown).
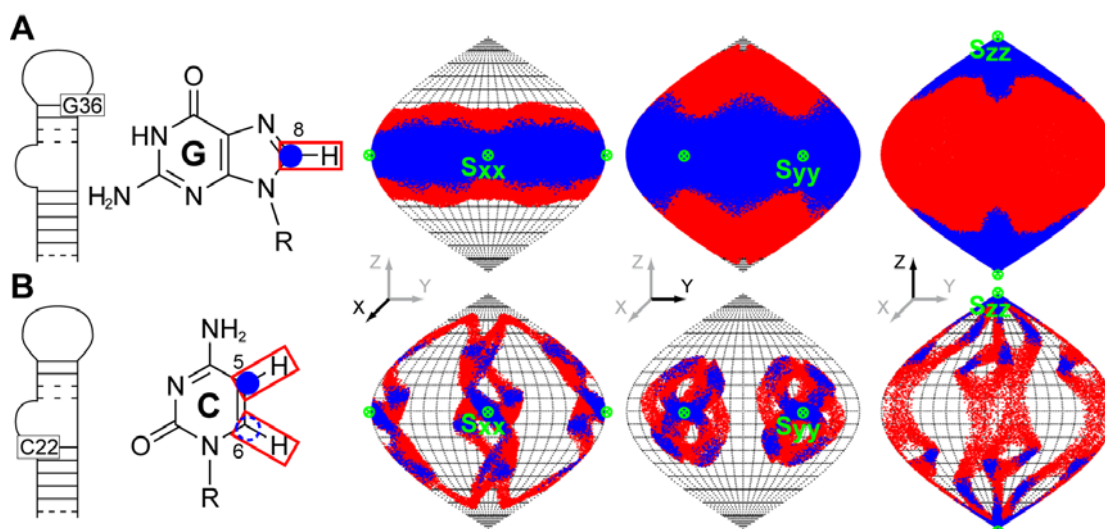
Figure 2.5. Long-range constraints on the orientation of nucleobases from ^{13}C RCSAs. Sauson-Flamsteed projection maps showing the RDC (in red) and RDC+RCSA (in blue) allowed base orientations for (A) G36 (one RDC and one RCSA) and (B) C22 (two RDCs and one RCSA). The base orientations are depicted relative to the order tensor PAS (S_{xx}, S_{yy}, S_{zz}) derived for TAR4312 using RDCs (poles of map, depicted in green). Clustering of solutions around the poles of the map implies agreement with the RDC validated A-form structures. The reduction in the spread of RDC solutions (in red) upon inclusion of RCSAs (in blue) reflects how much better base orientations can be defined by RCSAs even in the presence of ~10-20% CSA uncertainty (see main text).

2.3 Conclusion

The RCSAs measured in TAR4312 argue that the CSA magnitude (CSAa) of cytosine C5 in A-form RNA under solution NMR conditions is larger than that previously reported for mononucleotides. In contrast, the RCSAs largely support the validity of the mononucleotide guanine C8 CSAa value reported by solid-state NMR. Even after allowing for substantial uncertainty in the CSAs (ca. 10 – 20%), the RCSAs could be translated into useful long-range base-centered orientational constraints. This is in part because RCSAs provide constraints on directions orthogonal to the base plane that are seldom sampled directly by RDC vectors. Such constraints can in principle be obtained from additional measurements of other nucleobase one bond and two bond RDCs[53-55]. However, at the available magnetic field strengths, the field dependent RCSAs are between 4 to 15 times larger in magnitude and can be measured using sensitive NMR experiments that do not require resolution of small multiplet components. This will prove to be an advantage when studying larger RNAs.

2.4 References

1. Reif, B., Hennig, M. & Griesinger, C. Direct measurement of angles between bond vectors in high- resolution NMR. *Science* **276**, 1230-1233 (1997).

2. Chiarparin, E., Pelupessy, P., Ghose, R. & Bodenhausen, G. Relative orientation of (CH alpha)-H-alpha-bond vectors of successive residues in proteins through cross-correlated relaxation in NMR. *Journal Of The American Chemical Society* **122**, 1758-1761 (2000).

3. Schwalbe, H. et al. Cross-correlated relaxation for measurement of angles between tensorial interactions. *Methods Enzymol* **338**, 35-81. (2001).

4. Duchardt, E. et al. Determination of the glycosidic bond angle chi in RNA from cross-correlated relaxation of CH dipolar coupling and N chemical shift anisotropy. *J. Am. Chem. Soc* **126**, 1962-1970 (2004).

5. Fushman, D., Xu, R. & Cowburn, D. Direct determination of changes of interdomain orientation on ligation: Use of the orientational dependence of N-15 NMR relaxation in Abl SH(32). *Biochemistry* **38**, 10225-10230 (1999).

6. Kroenke, C.D., Rance, M. & Palmer, A.G. Variability of the N-15 chemical shift anisotropy in Escherichia coli ribonuclease H in solution. *Journal Of The American Chemical Society* **121**, 10119-10125 (1999).

7. Pervushin, K., Riek, R., Wider, G. & Wuthrich, K. Attenuated T-2 relaxation by mutual cancellation of dipole- dipole coupling and chemical shift anisotropy indicates an avenue to NMR structures of very large biological macromolecules in solution. *Proceedings of the National Academy of Sciences of the United States of America* **94**, 12366-12371 (1997).

8. Feng, X. et al. Direct determination of a peptide torsional angle psi by double-quantum solid-state NMR. *Journal Of The American Chemical Society* **119**, 12006-12007 (1997).

9. Fu, R.Q. & Cross, T.A. Solid-state nuclear magnetic resonance investigation of protein and polypeptide structure. *Annual Review Of Biophysics And Biomolecular Structure* **28**, 235-268 (1999).

10. Opella, S.J. & Marassi, F.M. Structure determination of membrane proteins by NMR spectroscopy. *Chem Rev* **104**, 3587-606 (2004).

11. Sanders, C.R., Hare, B.J., Howard, K.P. & Prestegard, J.H. Magnetically-Oriented Phospholipid Micelles As a Tool For the Study of Membrane-Associated Molecules. *Progress in Nuclear Magnetic Resonance Spectroscopy* **26**, 421-444 (1994).

12. Ramamoorthy, A. & Opella, S.J. Two-dimensional chemical shift/heteronuclear dipolar coupling spectra obtained with polarization inversion spin exchange at the magic angle and magic-angle sample spinning (PISEMAMAS). *Solid State Nucl Magn Reson* **4**, 387-92 (1995).

13. Cornilescu, G. & Bax, A. Measurement of proton, nitrogen, and carbonyl chemical shielding anisotropies in a protein dissolved in a dilute liquid crystalline phase. *Journal Of The American Chemical Society* **122**, 10143-10154 (2000).

14. Wu, Z.R., Tjandra, N. & Bax, A. P-31 chemical shift anisotropy as an aid in determining nucleic acid structure in liquid crystals. *Journal of the American Chemical Society* **123**, 3617-3618 (2001).

15. Bryce, D.L., Grishaev, A. & Bax, A. Measurement of ribose carbon chemical shift tensors for A-form RNA by liquid crystal NMR spectroscopy. *J Am Chem Soc* **127**, 7387-96 (2005).

16. Williamson, J.R. & Boxer, S.G. Multinuclear NMR studies of DNA hairpins. 1. Structure and dynamics of d(CGCGTTGTTCGCG). *Biochemistry* **28**, 2819-31. (1989).

17. Kojima, C., Ono, A., Kainosho, M. & James, T.L. DNA duplex dynamics: NMR relaxation studies of a decamer with uniformly 13C-labeled purine nucleotides. *J Magn Reson* **135**, 310-33. (1998).

18. Hall, K.B. & Tang, C.G. C-13 relaxation and dynamics of the purine bases in the iron responsive element RNA hairpin. *Biochemistry* **37**, 9323-9332 (1998).

19. Ravindranathan, S., Kim, C.H. & Bodenhausen, G. Cross correlations between 13C-1H dipolar interactions and 15N chemical shift anisotropy in nucleic acids. *J Biomol NMR* **27**, 365-75 (2003).

20. Duchardt, E. & Schwalbe, H. Residue Specific Ribose and Nucleobase Dynamics of the cUUCGg RNA Tetraloop Motif by NMR 13C Relaxation. *Journal of Biomolecular Nmr* **32**, 295-308 (2005).

21. Shajani, Z. & Varani, G. 13C NMR relaxation studies of RNA base and ribose nuclei reveal a complex pattern of motions in the RNA binding site for human U1A protein. *J Mol Biol* **349**, 699-715 (2005).

22. Akke, M., Fiala, R., Jiang, F., Patel, D. & Palmer, A.G. Base dynamics in a UUCG tetraloop RNA hairpin characterized by N-15 spin relaxation: Correlations with structure and stability. *RNA* **3**, 702-709 (1997).

23. Dingley, A.J. & Grzesiek, S. Direct observation of hydrogen bonds in nucleic acid base pairs by internucleotide (2)J(NN) couplings. *Journal of the American Chemical Society* **120**, 8293-8297 (1998).

24. Stueber, D. & Grant, D.M. 13C and (15)N chemical shift tensors in adenosine, guanosine dihydrate, 2'-deoxythymidine, and cytidine. *J Am Chem Soc* **124**, 10539-51. (2002).

25. Sitkoff, D. & Case, D.A. Theories of chemical shift anisotropies in proteins and nucleic acids. *Progress in NMR Spec.* **32**, 165-190 (1998).

26. Fiala, R., Czernek, J. & Sklenar, V. Transverse relaxation optimized triple-resonance NMR experiments for nucleic acids. *Journal of Biomolecular Nmr* **16**, 291-302 (2000).

27. Czernek, J., Fiala, R. & Sklenar, V. Hydrogen bonding effects on the N-15 and H-1 shielding tensors in nucleic acid base pairs. *Journal of Magnetic Resonance* **145**, 142-146 (2000).

28. Poon, A., Birn, J. & Ramamoorthy, A. How does an amide-N-15 chemical shift tensor vary in peptides? *Journal Of Physical Chemistry B* **108**, 16577-16585 (2004).

29. Boyd, J. & Redfield, C. Characterization of N-15 chemical shift anisotropy from orientation-dependent changes to N-15 chemical shifts in dilute bicelle solutions. *Journal Of The American Chemical Society* **121**, 7441-7442 (1999).

30. Lipsitz, R.S. & Tjandra, N. 15N chemical shift anisotropy in protein structure refinement and comparison with NH residual dipolar couplings. *J Magn Reson* **164**, 171-6 (2003).

31. Kurita, J., Shimahara, H., Utsunomiya-Tate, N. & Tate, S. Measurement of 15N chemical shift anisotropy in a protein dissolved in a dilute liquid crystalline medium with the application of magic angle sample spinning. *J Magn Reson* **163**, 163-73 (2003).

32. Lipsitz, R.S. & Tjandra, N. Carbonyl CSA restraints from solution NMR for protein structure refinement. *J Am Chem Soc* **123**, 11065-6 (2001).

33. Tjandra, N. & Bax, A. Direct measurement of distances and angles in biomolecules by NMR in a dilute liquid crystalline medium. *Science* **278**, 1111-1114 (1997).

34. Tolman, J.R., Flanagan, J.M., Kennedy, M.A. & Prestegard, J.H. Nuclear Magnetic Dipole Interactions in Field-Oriented Proteins - Information For Structure Determination in Solution. *Proceedings of the National Academy of Sciences of the United States of America* **92**, 9279-9283 (1995).

35. Clore, G.M. & Garrett, D.S. R-factor, free R, and complete cross-validation for dipolar coupling refinement of NMR structures. *Journal of the American Chemical Society* **121**, 9008-9012 (1999).

36. Tolman, J.R., Al-Hashimi, H.M., Kay, L.E. & Prestegard, J.H. Structural and dynamic analysis of residual dipolar coupling data for proteins. *Journal of the American Chemical Society* **123**, 1416-1424 (2001).

37. Ram, P. & Prestegard, J.H. Magnetic-Field Induced Ordering of Bile-Salt Phospholipid Micelles - New Media For Nmr Structural Investigations. *Biochimica Et Biophysica Acta* **940**, 289-294 (1988).

38. Meissner, A., Duus, J.O. & Sorensen, O.W. Spin-state-selective excitation. Application for E.COSY-type measurement of J(HH) coupling constants. *Journal of Magnetic Resonance* **128**, 92-97 (1997).

39. Meissner, A. & Sorensen, O.W. The role of coherence transfer efficiency in design of TROSY- type multidimensional NMR experiments. *Journal of Magnetic Resonance* **139**, 439-442 (1999).

40. Hansen, M.R., Mueller, L. & Pardi, A. Tunable alignment of macromolecules by filamentous phage yields dipolar coupling interactions. *Nature Structural Biology* **5**, 1065-1074 (1998).

41. Clore, G.M., Starich, M.R. & Gronenborn, A.M. Measurement of residual dipolar couplings of macromolecules aligned in the nematic phase of a colloidal suspension of rod- shaped viruses. *Journal of the American Chemical Society* **120**, 10571-10572 (1998).

42. Losonczi, J.A., Andrec, M., Fischer, M.W.F. & Prestegard, J.H. Order matrix analysis of residual dipolar couplings using singular value decomposition. *Journal of Magnetic Resonance* **138**, 334-342 (1999).

43. Ennifar, E. et al. The crystal structure of UUCG tetraloop. *Journal of Molecular Biology* **304**, 35-42 (2000).

44. Al-Hashimi, H.M. et al. Concerted motions in HIV-1 TAR RNA may allow access to bound state conformations: RNA dynamics from NMR residual dipolar couplings. *J Mol Biol* **315**, 95-102. (2002).

45. Al-Hashimi, H.M., Pitt, S.W., Majumdar, A., Xu, W. & Patel, D.J. Mg2+-induced variations in the conformation and dynamics of HIV-1 TAR RNA probed using NMR residual dipolar couplings. *J Mol Biol* **329**, 867-73. (2003).

46. Pitt, S.W., Majumdar, A., Serganov, A., Patel, D.J. & Al-Hashimi, H.M. Argininamide binding arrests global motions in HIV-1 TAR RNA: comparison with Mg2+-induced conformational stabilization. *J Mol Biol* **338**, 7-16. (2004).

47. Pitt, S.W., Zhang, Q., Patel, D.J. & Al-Hashimi, H.M. Evidence that electrostatic interactions dictate the ligand-induced arrest of RNA global flexibility. *Angew Chem Int Ed Engl* **44**, 3412-5 (2005).

48. Lavery, R. & Zakrzewska, K. Base and base pair morphologies, helical parameters, and definitions. in *Oxford Handbook of Nucleic Acid Structure* (ed. Neidle, S.) 39-76 (Oxford University Press, New York, 1999).

49. Cornell, W.D. et al. A 2nd Generation Force-Field For The Simulation Of Proteins, Nucleic-Acids, And Organic-Molecules. *Journal Of The American Chemical Society* **117**, 5179-5197 (1995).

50. Ying, J.F., Grishaev, A., Bryce, D.L. & Bax, A. Chemical shift tensors of protonated base carbons in helical RNA and DNA from NMR relaxation and liquid crystal measurements. *Journal Of The American Chemical Society* **128**, 11443-11454 (2006).

51. Brumovska, E. et al. Effect of local sugar and base geometry on C-13 and N-15 magnetic shielding anisotropy in DNA nucleosides. *Journal Of Biomolecular Nmr* **42**, 209-223 (2008).

52. Ramirez, B.E. & Bax, A. Modulation of the alignment tensor of macromolecules dissolved in a dilute liquid crystalline medium. *Journal of the American Chemical Society* **120**, 9106-9107 (1998).

53. Zidek, L., Wu, H., Feigon, J. & Sklenar, V. Measurement of small scalar and dipolar couplings in purine and pyrimidine bases. *J Biomol NMR* **21**, 153-60. (2001).

54. Jaroniec, C.P., Boisbouvier, J., Tworowska, I., Nikonowicz, E.P. & Bax, A. Accurate measurement of 15N-13C residual dipolar couplings in nucleic acids. *J Biomol NMR* **31**, 231-41 (2005).

55. Yan, J., Corpora, T., Pradhan, P. & Bushweller, J.H. MQ-hCN-based pulse sequences for the measurement of 13C1'-1H1', 13C1'-15N, 1H1'-15N, 13C1'-13C2', 1H1'-13C2',13C6/8-1H6/8, 13C6/8-15N, 1H6/8-15N, 13C6-13C5, 1H6-13C5 dipolar couplings in 13C, 15N-labeled DNA (and RNA). *J Biomol NMR* **22**, 9-20 (2002).

Chapter 3. Dynamics of Large Elongated RNA by NMR Carbon Relaxation

3.1 Introduction

Many regulatory RNAs undergo large conformational transitions that are essential for executing their functions.[1-3] Step-wise changes in RNA conformation induced by sequential protein recognition events allow complex ribonucleoproteins, such as the ribosome and spliceosome, to assemble in a hierarchically ordered manner.[4] Riboswitches control gene expression by undergoing large changes in secondary and tertiary structure in response to recognition of metabolite molecules.[5,6] The global conformation of ribozymes change during their catalytic cycles in order to satisfy the diverse structural requirements associated with substrate binding, catalysis, and product release.[7,8] Although it is clear that many RNA structures must change in a specific manner in order to carry out their functions, the mechanism by which these conformational changes occur is not fully understood. Recent studies suggest that the inherent dynamical properties of RNA structure play an important role in directing these conformational transitions.[9,10]

Nuclear magnetic resonance (NMR) spectroscopy is a powerful technique for characterizing the dynamical properties of biomolecules, uniquely providing site-resolved dynamical information over a broad range (ps-s) of timescales.[10-13] The most commonly used approach to obtaining dynamical information involves analyzing transverse (R_2) and longitudinal (R_1) relaxation rates together with heteronuclear Overhausser enhancements (NOEs) using the model free formalism[14] to obtain information regarding internal fluctuations occurring at sub-nanosecond timescales. Though this approach is now widely used in NMR studies of protein dynamics using backbone amide nitrogens as relaxation probes, a number of factors continue to

complicate applications to nucleic acids. The scarcity of suitable imino nitrogen probes has made it crucial to resort to other relaxation probes, including deuterium[15] or more commonly the protonated carbons.[13,16-22] However, carbon spins pose unique challenges in both measurement and data interpretation due to presence of C-C interactions and sizeable asymmetric chemical shift anisotropy (CSA) tensors. Perhaps an even greater problem that has surfaced only more recently is that globally flexible RNAs can violate the "decoupling approximation" which is invoked in the model free formalism which assumes that internal and overall motions are not correlated to one another.[14] This violation occurs because helices can move collectively at timescales approaching that of overall molecular tumbling (τ_m). These motions can also lead to substantial deformations in the RNA and cause spatially coupled changes in overall reorientation.[23-28] Such motional couplings can add an intractable layer of complexity to the analysis of relaxation data.

Recently, we reported a domain-elongation strategy for decoupling internal motions in RNA from overall diffusion as a prerequisite for quantitatively interpreting relaxation data.[25] Here, a terminal RNA helix is elongated using a stretch of twenty-two NMR-invisible Watson-Crick base-pairs in an otherwise uniformly $^{13}C/^{15}N$ labeled RNA. In addition to decoupling collective movements of helices from overall reorientation, elongation reduces the overall tumbling rate, thus broadening the timescale sensitivity of the relaxation data. Measurement of imino nitrogen relaxation data in elongated RNAs (E-RNA) has allowed resolution of collective helix motions in a variety of structural contexts that otherwise evade detection in non-elongated RNA owing to couplings with overall reorientation.[23,25,26] So far, the limited number of available imino nitrogen probes have not allowed for a comprehensive site-specific characterization of dynamics, particularly in the functionally important non-helical regions. Nevertheless, qualitative analysis of resonance intensities suggests the presence of near τ_m local motions that also evade detection in non-elongated RNAs. .[23-26]

There have been significant advances in applying carbon relaxation in studies of dynamics in relatively small nucleic acids that tumble nearly isotropically (D_{ratio} < 2.0).[13,19,20,27,29] The CSA tensors for the protonated carbons[30-32] have also recently been determined in solution using residual CSA (RCSA) and spin relaxation measurements thus resolving a great source of uncertainty in dynamical interpretation of the relaxation data. However, the need to decouple internal from overall motions via domain-elongation results in a significant increase in molecular weight and anisotropy of the RNA which in turn introduces a number of new challenges. First, the increase in the carbon transverse relaxation rates can make accurate measurement of relaxation data difficult. Second, homonuclear carbon relaxation contributions increase dramatically[18,22,33] and can no longer be ignored. Third, the significant increase in structural anisotropy of E-RNA renders relaxation data strongly dependent on the orientation of the non-collinear C-H, C-C and asymmetric CSA interactions relative to the principal axis (D_{zz}) of overall rotational diffusion.
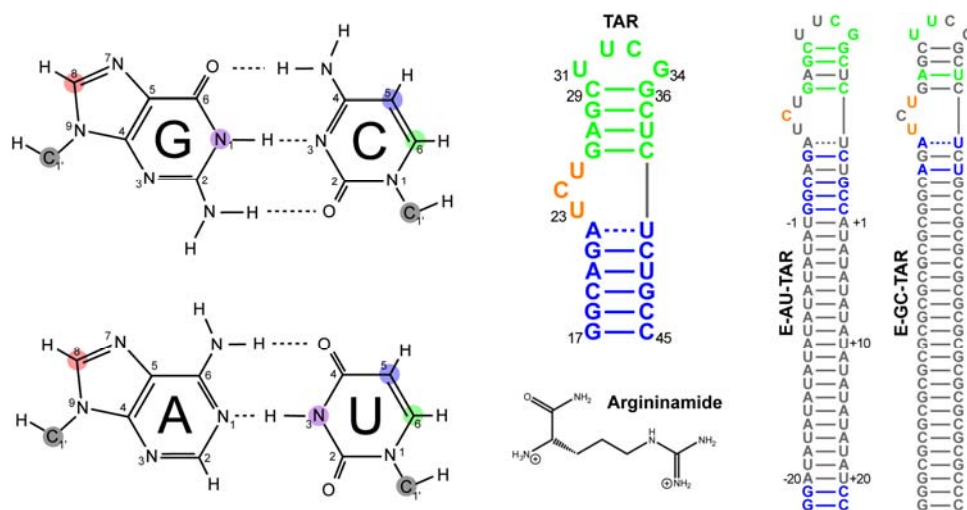
Figure 3.1. Carbon relaxation probes and elongation of HIV-1 TAR. Shown are the base and sugar carbon relaxation probes, secondary structure of non-elongated (NE-TAR) and elongated (E-GC-TAR and E-AU-TAR) TAR and chemical structure of argininamide. Uniformly ^{13}C/^{15}N labeled and unlabeled RNA residues are shown in color and grey, respectively.

Here, we describe application of carbon relaxation in characterizing the dynamics of large, highly anisotropic, uniformly ^{13}C/^{15}N labeled RNA with specific application to elongated HIV-1 TAR (E-TAR)[34-36] both in free form and bound to argininamide, a ligand

mimic of the TAR cognate protein target Tat (Figure 3.1). Our results provide fundamental new insights into the internal motions in TAR and their role in adaptive recognition as well as establish the ability to quantitatively study the dynamics of RNAs significantly larger and more anisotropic than customarily studied by NMR carbon relaxation.

3.2 Materials and Methods

3.2.1 NMR spectroscopy

All NMR samples were prepared by <u>in vitro</u> transcription as described previously.[25] The NMR buffer consisted of 15 mM sodium phosphate, 0.1 mM EDTA, and 25 mM NaCl at pH ~6.4. The argininamide bound TAR sample also contained ~8 mM argininamide (Sigma-Aldrich). All NMR experiments were performed at 298 K, unless specified otherwise, using an Avance Bruker 600 MHz spectrometer equipped with a 5mm triple-resonance cryogenic probe. NMR spectra were processed using nmrPipe[37] and analyzed using NMRView.[38]

Longitudinal (R_1) and rotating-frame ($R_{1\rho}$) relaxation rates were measured for nucleobase carbons C2, C5, C6 and C8 (Figure 3.1) using a TROSY detected (TD) experiment shown in Figure 3.3a.[39-41] Narrow and wide rectangles indicate 90° and 180° pulses, respectively. Selective pulses a and b are on resonance and c is off resonance. The **a** pulse selectively inverts carbon magnetization of interest. The **b** (**c**) pulses selectively refocus (invert) carbon magnetization to eliminate C-C scalar coupling evolution. τ = $1/4J_{CH}$ and $\tau' = \tau - \frac{1}{2} G_6$. Pulse field gradients (PFG) are sine shaped with the following amplitude (G/cm)/durations (ms): G_0 = -6.0/1.0, G_1 = 0.5/0.25, G_2 = 8.0/1.0, $G_3(R_1)$ = 3.3/1.0, $G_3(R_{1\rho})$ = 6.0/1.0, G_4 = 5.0/0.15, G_5 = 9.0/0.6, G_6 = 9.052/0.15. Phases are for Bruker spectrometers. Unless noted otherwise, all pulses have an x phase. The phase cycle is ϕ_1 = 4 (x, -x), ϕ_2 = 4 (y) 4 (-y), ϕ_3 = 2 (y, y, -y, -y), ϕ_4 = -y, ϕ_5 = -x, and ϕ_6 = (x, -x, -x, x, -x, x, x, -x). Axial peaks are shifted to the edge of the spectrum by incrementing ϕ_3 and ϕ_6 by

Spin	On-Resonance Inversion Shape	Pulse width (μs)	On-Resonance Refocusing Shape	Pulse Width (μs)	Off-Resonance Inversion Shape	Pulse width (μs)	Offset (ppm)	Carrier (ppm)	Sweep Width (ppm)	Spin Lock Offset (Hz)	Spin Lock power (Hz)
E-AU-TAR and E-AU-TAR+ARG											
C2 C6 C8	ISNOB2	500	REBURP	1600	ISNOB2	450	94	136.5	22	+2750	3484.1 ± 27.1
C5	ISNOB2	500	REBURP	1000	IBURP2	750	152	98	14	-2000	3484.1 ± 27.1
C1′	Q3	2000	RSNOB	1250	Q3	2000	73	91	20	+2000	2244.7 ± 18.5
E-GC-TAR, E-GC-TAR+ARG, and NE-TAR											
C2 C6 C8	Q3	750	REBURP	1000	ISNOB2	500	99	142.5	27	+1700	3484.1 ± 27.1
C5	ISNOB2	450	REBURP	1000	IBURP2	750	152	99	20	-1750	3484.1 ± 27.1
C1′	Q3	2000	RSNOB	1250	Q3	2000	73	91	20	+2000	2244.7 ± 18.5

Table 3.1. Parameters for the R_1 and $R_{1\varrho}$ experiments. A recycle delay of 1.5 sec was used for all experiments.

R_1	Delays (ms) C2, C6, and C8	C5	C1′
TD E-TAR			
25°C	20, 60 (x2), 100, 200, 400, 700 (x2), 1000	20, 760 (x4)	na
7°C	20, 700 (x4)	na	na
non-selective	20, 60 (x2), 100, 200, 400, 700 (x2), 1000	na	na
Argininamide bound	20, 860 (x4)	20, 760 (x4)	na

	Delays (ms)		
R_1	C2, C6, and C8	C5	C1′
non-TD E-TAR			
25°C	20, 60 (x2), 100, 200, 400, 700 (x2), 1000	na	20, 1000 (x4)
7°C	20	na	na
Argininamide bound	na	na	20, 1000 (x4)
non-TD NE-TAR			
25°C	20, 580 (x4)	20, 660 (x4)	20, 640 (x4)
$R_{1\varrho}$			
TD E-TAR			
25°C	4, 8 (x2), 12, 24, 32, 48 (x2), 64	4, 23 (x4)	na
7°C	4, 10 (x2), 18 (x2)	na	na
Argininamide bound	4, 15 (x2), 30 (x2)	4, 23 (x4)	na
non-TD E-TAR			
25°C	4, 8 (x2), 12, 24, 32, 48 (x2), 64	na	4, 12 (x2), 32 (x2)
7°C	4	na	na
Argininamide bound	na	na	4, 12 (x2), 32 (x2)
non-TD NE-TAR			
25°C	4, 60 (x4)	4, 70 (x4)	4, 78 (x4)

Table 3.2. Relaxation delays used in the R_1 and $R_{1\varrho}$ experiments. Duplicate and quadruplicate measurements used to estimate error are indicated using "x2" and "x4", respectively.

180° for each t_1 increment. ω_C represents the carrier offset frequency. In the R_1 element, Δ is set to 10 ms and the carrier remains on resonance, while in the $R_{1\varrho}$ element the carrier is shifted before and after the adiabatic passages. Detailed experimental parameters are provided in Tables 3.1 and 3.2. A non-TROSY version of the pulse sequence was used to measure relaxation data for C1'. Set-up and acquisition parameters are listed in Tables 3.1 and 3.2. High power off-resonance spin locks were used in the $R_{1\varrho}$ experiment to minimize contributions from chemical exchange while suppressing Hartman-Hahn type transfers to scalar coupled carbon spins (<u>vide infra</u>, Table 3.1). Accurate alignment of the $\pm C_z$ magnetization to and from the effective field tilt angle θ at the beginning and end of the relaxation period was achieved using adiabatic half passages.[42] Spin lock powers were carefully calibrated as previously described (Figure 3.2).[43]
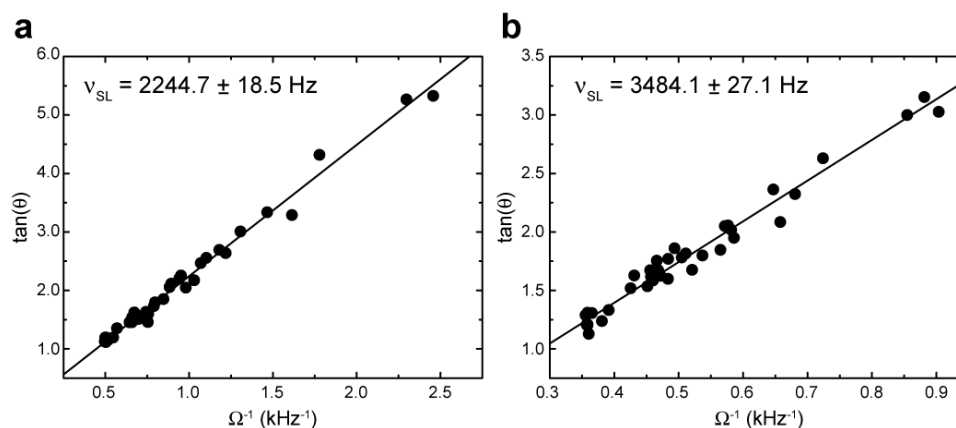
Figure 3.2. Calibration of spin lock used in the $R_{1\varrho}$ experiment for (a) C1' and (b) C2, C5, C6, and C8 carbons.

The $R_{1\varrho}$ rates were corrected for off-resonance effects according to $R_{1\varrho} = R_1 \cos^2\theta + R_2 \sin^2\theta$, in which $\theta = \arctan(\nu_{SL}/\Omega)$ is the effective tilt angle of the spinlock field, ν_{SL} is the spinlock field strength in Hz, and Ω is the resonance offset from the spinlock carrier frequency in Hz. All relaxation series were recorded in an interleaved manner with alternating short and long relaxation (T) delays (Table 3.2). Relaxation rates and errors were determined by fitting intensities to a mono-exponential decay using Origin 7.0 (OriginLab Corporation) and in-house software. The ^{13}C-{^1H} NOEs were measured for C2 and C8 using conventional experiments from the intensity ratio with and without proton saturation. NOEs were not measured for C1', C5, and C6 because the effects of

homonuclear C-C relaxation lead to significant errors in the measurements.[44] The measured relaxation data is listed in Tables 3.3-3.5.

Residue	Carbon	R_1 (Hz)	R_2 (Hz)
G17	C8	1.929 ± 0.003	26.99 ± 0.04
G18	C1′	1.458 ± 0.017	26.58 ± 0.04
	C8	2.002 ± 0.002	27.66 ± 0.04
C19	C5	2.275 ± 0.004	30.37 ± 0.03
	C6	2.642 ± 0.002	33.55 ± 0.03
A20	C1′	1.531 ± 0.011	21.97 ± 0.05
	C2	2.140 ± 0.006	30.30 ± 0.03
	C8	1.999 ± 0.003	27.58 ± 0.04
G21	C1′	1.563 ± 0.010	21.25 ± 0.05
	C8	1.936 ± 0.005	28.73 ± 0.03
A22	C1′	1.650 ± 0.009	21.88 ± 0.05
	C2	2.043 ± 0.004	32.54 ± 0.03
	C8	1.949 ± 0.004	27.95 ± 0.04
U23	C1′	2.010 ± 0.009	17.25 ± 0.06
	C5	2.349 ± 0.004	23.94 ± 0.04
	C6	2.735 ± 0.004	28.96 ± 0.03
C24	C5	2.541 ± 0.004	20.03 ± 0.05
	C6	2.821 ± 0.004	23.12 ± 0.04
U25	C5	2.407 ± 0.003	21.22 ± 0.05
	C6	2.762 ± 0.003	25.89 ± 0.04
G26	C8	1.901 ± 0.002	29.07 ± 0.03
A27	C1′	1.401 ± 0.010	26.28 ± 0.04
	C2	2.005 ± 0.006	32.85 ± 0.03
	C8	1.937 ± 0.003	29.18 ± 0.03
G28	C1′	1.478 ± 0.009	24.07 ± 0.04
	C8	1.977 ± 0.004	28.15 ± 0.04
C29	C5	2.280 ± 0.008	29.51 ± 0.03
	C6	2.550 ± 0.005	36.25 ± 0.03
U31	C1′	1.576 ± 0.010	21.52 ± 0.05
	C5	2.273 ± 0.004	28.63 ± 0.03
	C6	2.526 ± 0.005	35.91 ± 0.03
U32	C1′	1.600 ± 0.011	20.27 ± 0.05
	C5	1.912 ± 0.005	21.34 ± 0.05
	C6	2.137 ± 0.005	24.11 ± 0.04
C33	C1′	1.564 ± 0.014	22.91 ± 0.04
	C5	2.164 ± 0.007	28.92 ± 0.03
	C6	2.326 ± 0.003	33.76 ± 0.03
G34	C1′	1.577 ± 0.010	20.95 ± 0.05
	C8	1.888 ± 0.003	25.25 ± 0.04
G36	C1′	1.440 ± 0.012	23.17 ± 0.04
	C8	1.972 ± 0.003	27.30 ± 0.04

C37	C1′	1.537 ± 0.009	22.69 ± 0.04
	C5	2.295 ± 0.004	29.59 ± 0.03
	C6	2.542 ± 0.004	36.27 ± 0.03
U38	C5	2.253 ± 0.007	29.00 ± 0.03
	C6	2.546 ± 0.004	36.74 ± 0.03
C39	C5	2.308 ± 0.006	29.77 ± 0.03
	C6	2.477 ± 0.007	36.86 ± 0.03
U40	C1′	1.665 ± 0.010	20.81 ± 0.05
	C5	2.243 ± 0.006	28.29 ± 0.04
C41	C1′	1.534 ± 0.009	23.08 ± 0.04
	C5	2.211 ± 0.009	28.98 ± 0.03
	C6	2.428 ± 0.005	35.97 ± 0.03
U42	C1′	1.561 ± 0.011	24.89 ± 0.04
	C5	2.168 ± 0.011	29.89 ± 0.03
G43	C1′	1.602 ± 0.014	22.20 ± 0.05
	C8	1.978 ± 0.005	28.11 ± 0.04
C44	C1′	1.669 ± 0.012	19.69 ± 0.05
	C5	2.275 ± 0.007	29.63 ± 0.03
	C6	2.621 ± 0.005	34.14 ± 0.03
C45	C1′	1.807 ± 0.010	17.06 ± 0.06
	C5	2.351 ± 0.018	27.28 ± 0.04
	C6	2.569 ± 0.004	32.70 ± 0.03

Table 3.3. R_1 and R_2 measured for NE-TAR using standard (non-TROSY) experiments.

Residue	Carbon	R_1[a] (Hz)	R_1[b] (Hz)	σ_{C5C6} (Hz)	R_2 (Hz)	NOE[c]
G17	C8	0.942 ± 0.019	0.909 ± 0.040		104.64 ± 2.28	1.257 ± 0.128
G18	C8	0.980 ± 0.016	0.972 ± 0.066		112.90 ± 2.38	1.218 ± 0.121
C19	C5[d]	1.631 ± 0.045			110.00 ± 5.08	
	C6	1.600 ± 0.056	0.925 ± 0.088	-0.675 ± 0.104	130.58 ± 8.69	
A20	C1′	0.814 ± 0.103			85.17 ± 15.10	
	C2	1.086 ± 0.024			123.82 ± 8.47	1.147 ± 0.146
	C8	1.069 ± 0.027			99.31 ± 6.24	1.252 ± 0.154
G21	C1′	0.975 ± 0.063			90.63 ± 8.52	
	C8	1.027 ± 0.016	1.079 ± 0.033		107.28 ± 2.15	1.188 ± 0.118
A22	C1′	1.192 ± 0.063			93.33 ± 6.13	
	C2	1.143 ± 0.017			123.28 ± 5.39	1.174 ± 0.119
	C8	1.190 ± 0.025			102.21 ± 4.34	1.243 ± 0.127
U23	C1′	1.805 ± 0.027			51.97 ± 1.14	
	C5[d]	2.044 ± 0.028			87.49 ± 1.71	
	C6	2.088 ± 0.038			107.63 ± 4.51	
C24	C5[d]	2.315 ± 0.017			55.52 ± 0.54	
	C6	2.310 ± 0.016	2.057 ± 0.037	-0.253 ± 0.040	67.09 ± 0.53	
U25	C1′	1.756 ± 0.032			62.29 ± 1.70	
	C5[d]	2.210 ± 0.023			70.12 ± 1.07	
	C6	2.366 ± 0.022			73.79 ± 1.28	
G26	C8	1.341 ± 0.013	1.270 ± 0.035		87.51 ± 1.11	1.220 ± 0.077

Residue	Atom	R$_1$ (Hz)^a	R$_1$ (Hz)^b	σ_{C5C6}	R$_2$ (Hz)	NOE^c
A27	C1′	1.208 ± 0.078			80.74 ± 8.59	
	C2	1.355 ± 0.020			101.98 ± 3.59	1.198 ± 0.097
	C8	1.364 ± 0.021			83.80 ± 2.67	1.214 ± 0.085
G28	C8	1.470 ± 0.015	1.410 ± 0.023		79.15 ± 0.99	1.210 ± 0.065
C29	C5^d	2.102 ± 0.033			93.68 ± 2.03	
	C6	2.145 ± 0.040	1.877 ± 0.066	-0.268 ± 0.078	103.47 ± 2.59	
U31	C1′	1.369 ± 0.045			56.99 ± 2.52	
	C5^d	2.153 ± 0.040			91.03 ± 2.42	
	C6	2.143 ± 0.058			99.70 ± 6.06	
U32	C1′	1.411 ± 0.021			54.16 ± 1.35	
	C5^d	1.977 ± 0.025			67.58 ± 1.27	
	C6	2.100 ± 0.026			61.91 ± 1.39	
C33	C1′	1.505 ± 0.024			56.74 ± 1.68	
	C5^d	2.017 ± 0.043			91.29 ± 2.56	
	C6	2.014 ± 0.032	1.538 ± 0.040	-0.476 ± 0.052	96.51 ± 2.38	
G34	C1′	1.435 ± 0.019			58.12 ± 1.24	
	C8	1.448 ± 0.009	1.381 ± 0.021		67.53 ± 0.55	1.270 ± 0.049
G36	C1′	1.366 ± 0.026			62.00 ± 1.99	
	C8	1.456 ± 0.011	1.385 ± 0.029		81.40 ± 0.83	1.259 ± 0.070
C37	C5^d	2.098 ± 0.032			92.47 ± 2.01	
U38	C1′	1.424 ± 0.043			62.94 ± 2.70	
	C5^d	2.015 ± 0.046			92.65 ± 2.95	
	C6	2.199 ± 0.064			97.67 ± 6.84	
C39	C1′	1.367 ± 0.025			65.61 ± 1.92	
	C5^d	2.168 ± 0.042			95.14 ± 2.50	
U40	C1′	1.478 ± 0.053			67.47 ± 3.62	
	C5^d	2.055 ± 0.046			91.31 ± 2.93	
C41	C5^d	1.711 ± 0.044			111.28 ± 4.51	
	C6	1.672 ± 0.048	1.079 ± 0.085	-0.593 ± 0.097	140.71 ± 6.47	
U42	C1′	1.084 ± 0.096			73.88 ± 14.08	
	C5^d	1.690 ± 0.058			114.08 ± 6.32	
G43	C8	0.994 ± 0.020	1.002 ± 0.043		97.75 ± 2.28	1.265 ± 0.140
C44	C5^d	1.671 ± 0.047			117.13 ± 5.87	

Table 3.4. R$_1$, R$_2$, σ_{C5C6} and C-H NOE measured for E-TAR using the TROSY-detected (C2 C5 C6 C8) and non-TROSY detected (C1′) experiments. Shown are the R$_1$ values measured ^{a}with and ^{b}without selective inversion of the carbon of interest during the INEPT. ^{c}Non-TROSY detected experiments were used to determine heteronuclear NOE values for C2 and C8 spins. ^{d}To minimize overlap with water signals, the F2 semi-TROSY peak ($\Omega_{C5}+\pi$ J$_{CH}$, $\Omega_{H5}+\pi$ J$_{CH}$) was detected.

Residue	Atom	R$_1$ (Hz)	R$_2$ (Hz)	NOE ^{a}
G17	C8	0.827 ± 0.018	116.65 ± 3.83	1.180 ± 0.072
G18	C8	0.924 ± 0.017	117.18 ± 3.59	1.187 ± 0.084
C19	C5^b	1.713 ± 0.038	123.67 ± 4.22	
	C6	1.517 ± 0.049	139.18 ± 8.13	

A20	C2	0.928 ± 0.021	138.04 ± 7.92	1.342 ± 0.213
	C8	0.914 ± 0.023	118.05 ± 5.13	1.238 ± 0.184
G21	C1′	0.883 ± 0.060	85.29 ± 5.96	
	C8	0.925 ± 0.019	111.01 ± 3.57	1.195 ± 0.082
A22	C2	1.058 ± 0.021	122.11 ± 6.15	1.146 ± 0.200
	C8	1.012 ± 0.029	116.41 ± 5.36	1.093 ± 0.185
U23	C1′	1.356 ± 0.083	50.85 ± 5.82	
	C5b	1.736 ± 0.067	115.49 ± 5.95	
	C6	1.651 ± 0.069	101.21 ± 10.78	
C24	C1′	2.115 ± 0.003	21.72 ± 0.27	
	C5b	2.323 ± 0.005	30.85 ± 0.32	
	C6	2.390 ± 0.006	35.63 ± 0.39	
U25	C1′	1.935 ± 0.012	36.16 ± 0.73	
	C5b	2.176 ± 0.011	40.70 ± 0.65	
	C6	2.550 ± 0.013	38.92 ± 0.48	
G26	C8	1.021 ± 0.016	111.24 ± 2.99	1.224 ± 0.075
A27	C1′	0.815 ± 0.103	46.37 ± 14.74	
	C2	0.999 ± 0.021	123.48 ± 7.75	1.163 ± 0.182
	C8	1.114 ± 0.028	111.44 ± 4.88	1.112 ± 0.176
G28	C8	1.026 ± 0.018	107.98 ± 3.27	1.213 ± 0.083
C29	C5b	1.833 ± 0.038	120.11 ± 3.85	
	C6	1.544 ± 0.051	132.28 ± 7.93	
U31	C1′	1.273 ± 0.097	55.45 ± 8.89	
	C5b	1.894 ± 0.063	118.69 ± 5.34	
	C6	1.775 ± 0.052	117.27 ± 7.76	
U32	C1′	1.182 ± 0.038	59.25 ± 3.24	
	C5b	1.698 ± 0.029	80.03 ± 1.99	
	C6	1.701 ± 0.025	77.42 ± 2.04	
C33	C1′	1.285 ± 0.030	75.47 ± 2.20	
	C5b	1.691 ± 0.048	96.24 ± 3.50	
	C6	1.695 ± 0.040	110.53 ± 4.86	
G34	C8	1.079 ± 0.011	88.36 ± 1.59	1.256 ± 0.042
G36	C1′	1.163 ± 0.055	81.59 ± 4.28	
	C8	1.094 ± 0.014	109.05 ± 2.52	1.301 ± 0.070
C37	C5b	1.823 ± 0.040	125.73 ± 4.12	
U38	C5b	1.770 ± 0.074	127.35 ± 8.30	
	C6	1.732 ± 0.069	154.79 ± 14.16	
C39	C1′	1.052 ± 0.060	95.03 ± 5.45	
	C5b	1.751 ± 0.043	132.95 ± 4.82	
	C6	1.527 ± 0.041	137.62 ± 7.18	
U40	C1′	0.871 ± 0.087	67.43 ± 15.27	
	C5b	1.671 ± 0.072	124.20 ± 7.68	
	C6	1.588 ± 0.065	119.24 ± 12.29	
C41	C5b	1.708 ± 0.042	112.74 ± 3.95	
	C6	1.662 ± 0.058	144.12 ± 10.41	
U42	C5b	1.535 ± 0.071	128.99 ± 8.35	
	C6	1.615 ± 0.072	189.94 ± 24.59	
G43	C8	0.898 ± 0.020	112.66 ± 3.71	1.187 ± 0.094

C44	C5[b]	1.600 ± 0.037	118.65 ± 3.99
C45	C1′	1.282 ± 0.034	68.09 ± 2.26
	C5[b]	1.886 ± 0.054	114.97 ± 4.56

Table 3.5. R_1, R_2, and C-H NOE measured for E-TAR+ARG using the TROSY-detected (C2 C5 C6 C8) and non-TROSY detected (C1′) experiments. [a]Non-TROSY detected experiments were used. [b]Due to proximity to water, the F2 semi-TROSY peak ($\Omega_{C5}+\pi J_{CH}$, $\Omega_{H5}+\pi J_{CH}$) was detected.

In typical spin relaxation studies, a single decay will be measured using ~10 decay times, some of which are repeated to assess error in the measurement. Under reasonable conditions (~1 mM $^{13}C/^{15}N$ labeled RNA, 16 transients, 128 complex points, and recover delay of 1.5 sec), each 2D decay point can be measured in ~2-3 hours, resulting in a day of acquisition time per experiment (R_1 and $R_{1\rho}$). When sample conditions are not optimal and/or experiments need to be repeated under a variety of conditions/spin systems/spinlock field strengths, this can result in a prohibitively long amount of time. In situations where the relaxation decay is known to be mono-exponential, an optimized sampling strategy can be used, acquiring between two and five decay points, to dramatically reduce the experimental time.[45,46]

When relaxation times are very similar among all spin systems ($T_{max} < ~3\ T_{min}$), only two decay points are necessary at T=0 and T= ~1.2 $(T_{max}\cdot T_{min})^{1/2}$, the latter of which can be repeated several times. When times are not very similar ($T_{max} > ~3\ T_{min}$), as can occur for R2 measurements in highly anisotropic RNAs, more complicated schemes can be used which use either three or four decay points.[74] Obviously, an estimate for T_{max} and T_{min} is necessary to choose appropriate decay points and can be obtained from literature values of similar sized RNAs or from simulation. Alternatively, one can choose decay points experimentally by recording quick 1D traces of the relaxation experiment. A decay time of T= ~1.2 $(T_{max}\cdot T_{min})^{1/2}$ can be estimated as the decay time which results in a signal reduction of about 1/3 and the longest time point, if necessary, should be chosen such that the signal remains 3-5 times the signal/noise ratio. Optimized sampling times in this study are presented in Table 3.2.

3.2.2 Model free analysis

The carbon relaxation data was combined and analyzed with the nitrogen data reported by Zhang et al.[25] using an extended model free approach[14,47] implemented with in-house software that incorporates spectral density functions[48] (Equations 3.4-3.5) that can account for asymmetric CSAs under axially symmetric overall diffusion and includes contributions from all, non-collinear C-C and C-H dipolar interactions. In these calculations, it was assumed that the principal axes of all interaction tensors (i.e. CSA, C-H and C-C Dipole) experience identical isotropic internal motions. All relaxation data were calculated using Equations 3.1-3.5 and analyzed separately for E-GC-TAR and E-AU-TAR.

Motionally averaged bond lengths of 1.104 Å,[32] 1.041 Å,[49] and 1.115 Å[30,49] were used for the nucleobase C-H, imino N-H, and sugar C1'-H1', respectively. The solution NMR derived CSAs were used for C2, C5, C6, and C8[32] and C1'.[30] The static DFT computed imino nitrogen CSAs[50] were used after uniform scaling by a factor of 0.913[49] to account for the similar motional averaging of the CSA and N-H dipolar interaction.[51] The orientation of D_{zz} with respect to helices I and II was assumed to be equal to the orientation of the principal direction of alignment (S_{zz}) in Pf1 phage[52,53] determined by order tensor analysis[54,55] of RDCs measured in E-TAR.[56] Several studies have shown that in the absence of electrostatic attraction, the orientation of the alignment tensor frame is similar to that of the diffusion tensor.[57-60] Virtually identical D_{zz} and S_{zz} orientations (deviations ~3°) are also predicted for E-TAR based on its structure using HydroNMR[61] and PALES,[62] respectively. The experimentally derived S_{zz} orientation deviates from perfect coincidence with the elongated helix axis by ~6°. The hydrodynamically predicted D_{ratio} value of 4.7 was assumed[25] noting that ±10% variations had a negligible impact on the analysis (data not shown). For globally rigid E-TAR+ARG, the hydrodynamically predicted D_{ratio} (4.7) and D_{zz} orientation obtained for the RDC-derived NE-TAR+ARG inter-helical conformation[63] was assumed as previously described.[25] The local structure of the bulge was modeled into the RDC derived inter-helical

conformation using previous NOE structures of TAR (1ANR for free TAR[35] and both 1ARJ[64] and 1AJU[65] for ARG-bound TAR).

The global correlation time, τ_m, was initially determined through a χ^2 minimization of the elongated helix C2, C8, and N1/3 relaxation data (for which NOE data was also available) while also allowing a single internal correlation time (τ_e) and order parameter (S^2) to vary. The latter was crucial for determining a global correlation time that agrees with all carbon and nitrogen relaxation data. Analysis of the carbon data while excluding nitrogen data resulted in nearly identical motional parameters (S^2 rmsd < 0.02). The τ_m values obtained for free (16.8-18.1 ± 0.8 ns) and ARG-bound TAR (17.6-18.6 ± 1.4 ns) were in good agreement with values reported previously by ^{15}N relaxation (18.9-19.0 ± 0.9 ns and 18.4-18.6 ± 0.6 ns, respectively).[25] Following determination of the global correlation time, internal motional parameters were selected from five possible single field models (see §3.3.5).[66] Only models 1-3 were tested for the C1', C5, and C6 data since NOEs could not be measured reliably. The internal motional parameters, $S^2_{f/s}$ and τ_e, were minimized using a simplex algorithm[67] following a grid search with initial step sizes set sufficiently small to avoid trapping the simplex algorithm into false minima. For models including internal correlation times, the results were inspected for model elimination before being subjected to model selection.[68] The best internal motional parameters were selected using the Akaike's Information Criteria (AIC).[69]

The error in the internal motional parameters due to uncertainty in experimental measurements was obtained by performing Monte Carlo simulations of each R_1, R_2, and NOE set while leaving the global diffusion parameters fixed. In each simulation the relaxation data was perturbed randomly based on measurement error and minimized assuming the same error as the original data set. Motional parameter uncertainties were then determined from the trimmed mean of the distribution of 1000 model free parameters, including removal of simulations falling under model elimination criteria.[68] To estimate the uncertainty in motional parameters arising from potential errors in the assumed CSAs, the model free analysis was repeated using the solid-state NMR CSAs

for all spins[70] and the errors were generously estimated as the difference between the two sets of computed motional parameters. Likewise, conservative errors due to potential variations in the D_{zz} orientation were estimated by repeating the model free analysis assuming D_{zz} is perfectly coincident with the elongated helix axis and taking the difference between the two sets of motional parameters. For bulge residues, the standard deviation of the parameters determined using all input conformations was computed. The final error in the derived motional parameters was calculated as the root sum square of the individual error contributions. All motional parameters and uncertainties are listed in Tables 3.6-3.7.

Residue		S^2_t	S^2_t (normalized)	τ_{eff} (ps)	Model
A20	C1′	0.857 ± 0.098	0.857 ± 0.098		1
G21	C1′	0.958 ± 0.055	0.958 ± 0.055		1
A22	C1′	0.925 ± 0.053	0.925 ± 0.053	918.48 ± 387.48	2
U23	C1′	0.619 ± 0.102	0.619 ± 0.102	280.74 ± 152.52	2
U25	C1′	0.622 ± 0.133	0.622 ± 0.133	549.65 ± 430.86	2
A27	C1′	0.626 ± 0.072	0.626 ± 0.072	124.81 ± 33.38	2
U31	C1′	0.746 ± 0.102	0.746 ± 0.102	151.44 ± 49.83	2
U32	C1′	0.741 ± 0.106	0.741 ± 0.106	226.49 ± 86.46	2
C33	C1′	0.703 ± 0.022	0.703 ± 0.022	131.06 ± 26.38	2
G34	C1′	0.735 ± 0.05	0.735 ± 0.050	201.52 ± 45.86	2
G36	C1′	0.752 ± 0.063	0.752 ± 0.063	142.61 ± 30.39	2
U38	C1′	0.872 ± 0.103	0.872 ± 0.103	181.50 ± 153.89	2
C39	C1′	0.852 ± 0.028	0.852 ± 0.028	152.40 ± 58.68	2
U40	C1′	0.823 ± 0.093	0.823 ± 0.093	318.30 ± 195.53	2
U42	C1′	1.000 ± 0.083	1.000 ± 0.083		1
A20	C2	0.933 ± 0.025	1.000 ± 0.025	780.12 ± 480.27	2
A22	C2	0.917 ± 0.017	0.984 ± 0.017	584.80 ± 499.65	2
A27	C2	0.778 ± 0.077	0.834 ± 0.077	797.09 ± 1233.38	5
C19	C5	0.849 ± 0.026	0.927 ± 0.026		1
U23	C5	0.699 ± 0.080	0.763 ± 0.080	97.43 ± 43.70	2
C24	C5	0.405 ± 0.052	0.442 ± 0.052	125.42 ± 10.37	2
U25	C5	0.535 ± 0.123	0.584 ± 0.123	110.57 ± 30.97	2
C29	C5	0.701 ± 0.036	0.766 ± 0.036	126.49 ± 11.76	2
U31	C5	0.728 ± 0.064	0.796 ± 0.064	151.03 ± 32.79	2
U32	C5	0.642 ± 0.023	0.701 ± 0.023	73.02 ± 6.53	2
C33	C5	0.669 ± 0.037	0.730 ± 0.037	104.45 ± 8.92	2
C37	C5	0.684 ± 0.036	0.747 ± 0.036	125.96 ± 10.67	2

U38	C5	0.767 ± 0.060	0.837 ± 0.060	128.16 ± 29.20	2
C39	C5	0.764 ± 0.036	0.834 ± 0.036	147.30 ± 25.23	2
U40	C5	0.740 ± 0.062	0.808 ± 0.062	130.57 ± 23.25	2
C41	C5	0.876 ± 0.024	0.957 ± 0.024		1
U42	C5	0.916 ± 0.030	1.000 ± 0.030		1
C44	C5	0.884 ± 0.031	0.966 ± 0.031		1
C19	C6	0.824 ± 0.109	0.942 ± 0.109	70.49 ± 38.41	2
U23	C6	0.733 ± 0.097	0.837 ± 0.097	171.73 ± 58.81	2
C24	C6	0.434 ± 0.071	0.497 ± 0.071	137.46 ± 22.57	2
U25	C6	0.485 ± 0.081	0.555 ± 0.081	155.99 ± 21.58	2
C29	C6	0.632 ± 0.089	0.723 ± 0.089	127.36 ± 43.63	2
U31	C6	0.652 ± 0.108	0.745 ± 0.108	129.72 ± 56.95	2
U32	C6	0.503 ± 0.054	0.575 ± 0.054	94.27 ± 19.72	2
C33	C6	0.585 ± 0.071	0.668 ± 0.071	105.63 ± 26.15	2
U38	C6	0.657 ± 0.107	0.751 ± 0.107	137.78 ± 71.62	2
C41	C6	0.875 ± 0.109	1.000 ± 0.109	81.85 ± 80.48	2
G17	C8	0.859 ± 0.020	0.924 ± 0.020	510.47 ± 346.37	5
G18	C8	0.930 ± 0.008	1.000 ± 0.008	706.59 ± 288.52	2
A20	C8	0.845 ± 0.057	0.909 ± 0.057	553.32 ± 754.30	5
G21	C8	0.895 ± 0.027	0.962 ± 0.027	801.56 ± 925.83	5
A22	C8	0.889 ± 0.016	0.956 ± 0.016	489.49 ± 194.86	2
G26	C8	0.741 ± 0.037	0.797 ± 0.037	853.07 ± 351.77	5
A27	C8	0.753 ± 0.037	0.809 ± 0.037	802.00 ± 1277.16	5
G28	C8	0.663 ± 0.017	0.713 ± 0.017	914.91 ± 495.18	5
G34	C8	0.524 ± 0.007	0.564 ± 0.007	724.30 ± 165.37	5
G36	C8	0.655 ± 0.012	0.704 ± 0.012	745.62 ± 309.06	5
G43	C8	0.814 ± 0.026	0.875 ± 0.026	534.61 ± 322.41	5
G17	N1	0.974 ± 0.005	1.000 ± 0.005	297.03 ± 78.05	2
G18	N1	0.965 ± 0.017	0.990 ± 0.017	192.49 ± 171.81	2
G21	N1	0.965 ± 0.010	0.991 ± 0.010	724.56 ± 301.81	2
G28	N1	0.742 ± 0.016	0.762 ± 0.016	1443.93 ± 76.36	5
G34	N1	0.682 ± 0.010	0.700 ± 0.010	1379.83 ± 47.23	5
G36	N1	0.705 ± 0.018	0.724 ± 0.018	1407.83 ± 62.56	5
U38	N3	0.718 ± 0.051	0.737 ± 0.051	1490.69 ± 159.89	5
U42	N3	0.967 ± 0.023	0.992 ± 0.023	152.11 ± 487.64	2

Table 3.6. Motional parameters for free E-TAR. τ_{eff} is τ_f for models 1-4 and τ_s for model 5.

Residue		S^2_t	S^2_t (normalized)	τ_{eff} (ps)	Model
G21	C1′	0.821 ± 0.044	0.824 ± 0.044		1
U23	C1′	0.685 ± 0.130	0.688 ± 0.130	130.48 ± 30.44	2
C24	C1′	0.232 ± 0.015	0.233 ± 0.015	162.40 ± 3.44	2
U25	C1′	0.433 ± 0.071	0.434 ± 0.071	197.97 ± 36.26	2
U31	C1′	0.486 ± 0.141	0.488 ± 0.141	70.16 ± 13.32	2
U32	C1′	0.712 ± 0.117	0.714 ± 0.117	97.82 ± 25.37	2

C33	C1′	0.791 ± 0.021	0.793 ± 0.021	175.98 ± 29.67	2
G36	C1′	0.917 ± 0.061	0.920 ± 0.061	80.39 ± 190.59	2
C39	C1′	0.996 ± 0.026	1.000 ± 0.026		1
A20	C2	0.937 ± 0.028	1.000 ± 0.028	268.69 ± 272.14	2
A22	C2	0.816 ± 0.055	0.871 ± 0.055	1054.84 ± 441.58	5
A27	C2	0.930 ± 0.042	0.993 ± 0.042	402.04 ± 384.14	2
C19	C5	0.893 ± 0.021	0.950 ± 0.021		1
U23	C5	0.703 ± 0.040	0.748 ± 0.040	82.52 ± 15.81	2
C24	C5	0.219 ± 0.021	0.233 ± 0.021	117.94 ± 3.39	2
U25	C5	0.305 ± 0.025	0.325 ± 0.025	107.59 ± 6.16	2
C29	C5	0.865 ± 0.049	0.921 ± 0.049	56.86 ± 20.06	2
U31	C5	0.895 ± 0.054	0.953 ± 0.054	104.78 ± 53.30	2
U32	C5	0.648 ± 0.015	0.690 ± 0.015	49.93 ± 4.83	2
C33	C5	0.663 ± 0.039	0.706 ± 0.039	49.82 ± 7.67	2
C37	C5	0.923 ± 0.023	0.983 ± 0.023		1
U38	C5	0.940 ± 0.037	1.000 ± 0.037	0.000 ± 28.96	2
C39	C5	0.901 ± 0.022	0.959 ± 0.022		1
U40	C5	0.892 ± 0.031	0.949 ± 0.031		1
C41	C5	0.795 ± 0.046	0.846 ± 0.046	33.89 ± 17.05	2
U42	C5	0.807 ± 0.039	0.859 ± 0.039		1
C44	C5	0.835 ± 0.021	0.889 ± 0.021		1
C45	C5	0.837 ± 0.050	0.891 ± 0.050	74.13 ± 19.16	2
C19	C6	0.812 ± 0.104	1.000 ± 0.104	70.73 ± 20.62	2
U23	C6	0.715 ± 0.054	0.880 ± 0.054	85.73 ± 9.57	2
C24	C6	0.197 ± 0.027	0.243 ± 0.027	123.29 ± 11.59	2
U25	C6	0.277 ± 0.021	0.342 ± 0.021	138.89 ± 10.52	2
C29	C6	0.762 ± 0.098	0.939 ± 0.098	71.71 ± 16.75	2
U31	C6	0.766 ± 0.056	0.943 ± 0.056	122.68 ± 27.89	2
U32	C6	0.527 ± 0.015	0.649 ± 0.015	85.80 ± 6.40	2
C33	C6	0.622 ± 0.077	0.767 ± 0.077	86.86 ± 14.39	2
C39	C6	0.808 ± 0.106	0.996 ± 0.106	1023.75 ± 353.53	2
U40	C6	0.741 ± 0.077	0.913 ± 0.077	74.83 ± 15.14	2
C41	C6	0.809 ± 0.112	0.997 ± 0.112	80.78 ± 19.13	2
G17	C8	0.885 ± 0.028	0.934 ± 0.028	692.04 ± 459.42	5
G18	C8	0.889 ± 0.026	0.938 ± 0.026	750.05 ± 1510.35	5
A20	C8	0.947 ± 0.024	1.000 ± 0.024	455.94 ± 240.44	2
G21	C8	0.831 ± 0.024	0.878 ± 0.024	740.51 ± 399.20	5
A22	C8	0.918 ± 0.017	0.969 ± 0.017	2583.36 ± 390.14	2
G26	C8	0.855 ± 0.021	0.903 ± 0.021	676.10 ± 833.48	5
A27	C8	0.903 ± 0.015	0.953 ± 0.015	1545.91 ± 317.94	2
G28	C8	0.816 ± 0.023	0.861 ± 0.023	708.66 ± 323.91	5
G34	C8	0.666 ± 0.011	0.703 ± 0.011	638.99 ± 147.75	5
G36	C8	0.814 ± 0.016	0.859 ± 0.016	515.68 ± 153.56	5
G43	C8	0.847 ± 0.024	0.894 ± 0.024	706.74 ± 338.63	5
G17	N1	0.942 ± 0.009	0.960 ± 0.009	1800.37 ± 241.13	2
G18	N1	0.936 ± 0.010	0.954 ± 0.010	1321.05 ± 194.59	2
G21	N1	0.912 ± 0.008	0.930 ± 0.008	1393.71 ± 106.75	2
G26	N1	0.898 ± 0.009	0.916 ± 0.009	1485.80 ± 108.16	2

G28	N1	0.908 ± 0.011	0.926 ± 0.011	1002.50 ± 132.57	2
G36	N1	0.888 ± 0.010	0.906 ± 0.010	1413.39 ± 106.36	2
U38	N3	0.934 ± 0.063	0.952 ± 0.063	1130.31 ± 176.55	2
U42	N3	0.981 ± 0.036	1.000 ± 0.036	59.84 ± 35.13	2
G43	N1	0.964 ± 0.006	0.983 ± 0.006	988.40 ± 1035.14	2

Table 3.7. Motional parameters for E-TAR+ARG.

3.3 Results and Discussion

3.3.1 Contributions to carbon relaxation

It is instructive to consider the various relaxation contributions to our targeted carbons. The longitudinal and transverse carbon relaxation rates, taking into account all homo- and heteronuclear interactions, can be best understood through examination of their time dependancies:[18,44]

$$
\frac{d(\Delta C_z(t))}{dt} = -\left(\varrho_{C,CSA} + \sum_i \varrho_{CH_i} + \sum_j \varrho^0_{CC_j} + \sum_k \varrho^1_{CC_k} \right)(\Delta C_z(t)) - \sum_i \sigma_{CH_i}\left(\Delta H_{i,z}(t)\right)
$$
$$
- \sum_j \sigma^0_{CC_j}\left(\Delta C_{j,z}(t)\right) - \sum_k \sigma^1_{CC_k}\left(\Delta C_{k,z}(t)\right)
$$

(3.1)

$$
\frac{d(\Delta C_+(t))}{dt} = -\left(R_{2,CSA} + \sum_i R_{2,CH_i} + \sum_j R^0_{2,CC_j} + \sum_k R^1_{2,CC_k} \right)(\Delta C_+(t)) + R_{ex}
$$

(3.2)

in which the various auto- (ϱ) and cross- (σ) relaxation longitudinal rates and R_2 transverse relaxation rates are given by:

$$
\varrho_{CX} = R_{1,CX} = \frac{1}{10} D_{CX}^2 \left\{ 6g_2^{DD}(\omega_C + \omega_X) + g_2^{DD}(\omega_C - \omega_X) + 3g_2^{DD}(\omega_C) \right\}
$$

$$
\sigma_{CX} = \frac{1}{10} D_{CX}^2 \left\{ 6g_2^{DD}(\omega_C + \omega_X) - g_2^{DD}(\omega_C - \omega_X) \right\}
$$

$$
R_{2,CX} = \frac{1}{20} D_{CX}^2 \left\{ 6g_2^{DD}(\omega_C + \omega_X) + 6g_2^{DD}(\omega_X) + g_2^{DD}(\omega_C - \omega_X) + 3g_2^{DD}(\omega_C) + 4g_2^{DD}(0) \right\}
$$

$$
\varrho_{CSA} = R_{1,CSA} = \frac{1}{10} C_C^2 \left\{ 3g_2^{CSA}(\omega_C) \right\}
$$

$$
R_{2,CSA} = \frac{1}{20} C_C^2 \left\{ 3g_2^{CSA}(\omega_C) + 4g_2^{CSA}(0) \right\}
$$

(3.3)

D_{CX} and CC are the familiar dipolar coupling ($\mu_0 h \gamma_C \gamma_X / 8\pi^2 r_{CX}^3$) and CSA ($\omega_C \sigma_{zz}$) constants, R_{ex} is the chemical exchange contribution to transverse relaxation, and g_2 is the half-sided Fourier transform of the autocorrelation function describing the time dependence of the CSA (g_2^{CSA}) or dipolar (g_2^{DD}) interactions due to internal motions.[47] In the absence of asymmetric relaxation mechanisms, g_2 is equal to the common spectral density function, $J(\omega)$. R_2, ϱ, and σ subscripts indicate the type of relaxation mechanism (e.g. C-C dipolar, C-H dipolar, or CSA) while superscripts of homonuclear carbon dipolar interactions indicate the number of protons bound to the neighboring carbon (e.g. $\varrho_{C5C4} = \varrho_{CC}^0$). The carbon-carbon cross-relaxation in Equation 3.1 is separated into two terms because the magnetization state of neighboring carbons after the INEPT, and thus the contribution to the initial decay rate from cross-relaxation, will vary depending on whether the carbon is attached to a proton or not.

For an RNA with $\tau_m > 15$ ns, the dipolar contribution to R_2 from neighboring nitrogens, protons (>2 Å), and carbons (>1.3 Å) are negligible (< 2%), and can be safely ignored. Both the R_1 and R_2 for purine C2 and C8 and the R_2 for C5 and C6 are dominated by C-H dipolar and carbon CSA relaxation. The CSA contribution to R_2 ranges between 25-45% at 600 MHz, but can be as large as 35-65% at 900 MHz. For R_1, the corresponding CSA contribution at 600/900 MHz is 15-30%/24-33% for C2 and C8 and 5-30%/10-40% for C5 and C6. The CSA contribution to R_1 and R_2 for C1′ is negligible (<4% even at 900 MHz) and R_2 is dominated by C-H dipolar relaxation. In contrast, the C-C dipolar contribution from nearby carbons to R_1 for C5 (40-80%), C6 (20-70%), and C1′ (15-60%) is significant. As shown in Equation 3.3, of the three mechanisms in question, only CC dipolar contains a $g_2(0)$ term arising from $g_2(\omega_x-\omega_y)$ difference term. This term increases linearly as a function of correlation time, whereas all other spectral density terms decrease dramatically. The C-C auto- and cross-relaxation will therefore require careful consideration for the latter carbons. Longitudinal and transverse CSA_C/DD_{CC}, DD_{CC}/DD_{CC}, DD_{CC}/DD_{CH}, and DD_{C5H5}/DD_{C5H6} or DD_{C6H6}/DD_{C6H5} cross-correlated relaxation can be safely ignored as they are typically two to three orders of

magnitude smaller than the auto relaxation rates. The CSA_C/DD_{CH} cross-correlated relaxation and C-H cross-relaxation contributions to R_1 and CSA_C/DD_{CH} cross-correlated relaxation contribution to R_2, which can be on the order of the relaxation measurement itself, must be suppressed using an appropriate proton decoupling scheme during the relaxation period.[71,72] For the $R_{1\varrho}$ scheme of Figure 3.3a we use a decoupling scheme of Massi et al[71,72] which uses a pair of 180 pulses at T/4 and 3T/4 and performs well over a wide range of spin lock field strengths.

3.3.2 TROSY-detected pulse sequences

We implemented pulse sequences (Figure 3.3a) for measuring carbon relaxation that address two problems encountered in applications to large RNAs. The greater transverse relaxation rate for carbon spins (3-6 times greater than for nitrogen) leads to unfavorable loss in sensitivity that can make accurate measurement of relaxation data difficult. We used TROSY[73] detection (TD) to improve sensitivity and resolution in the R_1 and $R_{1\varrho}$ experiment for the nucleobase carbons C2, C5, C6, and C8, all of which have sizeable CSAs that give rise to favorable TROSY effects.[33,74] Following the normal relaxation period of longitudinal or in-phase ^{13}C magnetization, TROSY coherence selection in both ^{13}C and ^{1}H dimensions is used for detection of the slowly relaxing component resulting from destructive interference between CSA and dipole-dipole (DD) interactions. In addition, selective carbon pulses are used throughout to eliminate signal losses to neighboring scalar coupled carbons (J_{C5C6} ~67 Hz, $J_{C1'C2'}$ ~ 40 Hz) during the INEPT transfers and indirect detection period. The TD experiments yielded sensitivity improvements on the order of 50%, 65%, and 40% for C2, C6 and C8, respectively (Figure 3.3b, inset) for E-TAR at 600 MHz with τ_m = 18 ns, in agreement with theoretical predictions.[74] The TD experiments allowed us to reliably measure relaxation data for E-TAR at 280 K with τ_m ~ 35 ns corresponding to a ~150 nt RNA at 298 K, that could not otherwise be measured using conventional sequences due to overlap and/or poor signal-to-noise.
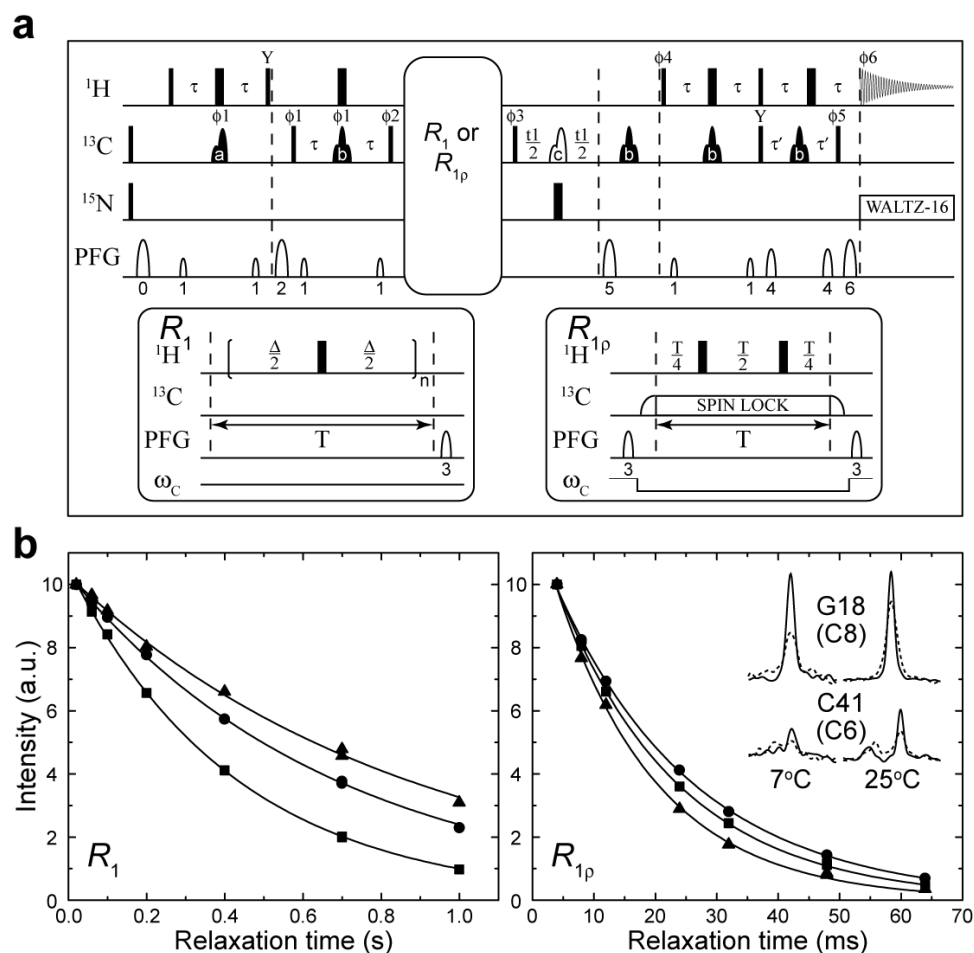
Figure 3.3. TROSY-detected (TD) experiments for the measurement of nucleobase carbon R_1 and $R_{1\varrho}$ in uniformly $^{13}C/^{15}N$ labeled RNA. (a) TD pulse sequence. (b) Representative R_1 and $R_{1\varrho}$ decays for residues in the elongated helix I (triangles), helix II (circles), and the bulge (squares). The inset depicts representative slices along the indirect carbon dimension comparing the TROSY (solid line) and non-TROSY (dotted line) detected experiments. Intensities are normalized relative to the TROSY G18 peak at each temperature.

The second problem encountered is that C-C dipolar interactions increase dramatically with molecular weight and large cross-relaxation rates can lead to multi-exponential behavior when measuring R_1 for C5, C6, and C1'.[44] Although the C-C cross-relaxation rate is approximately equal and opposite in magnitude to C-C auto-relaxation (Equations 3.1 and 3.3), their mutual cancellation[18,44] only occurs if the equilibrium magnetization of the neighboring carbons is identical to that of the carbon of interest and the relaxation time delays do not significantly exceed $1/R_1$. In our R_1 experiment, cross-relaxation to neighboring carbons is suppressed as originally described by Kay

and co-workers by gradient dephasing carbon magnetization at the beginning of the pulse sequence followed by selective excitation of the carbon nucleus of interest using a selective inversion ^{13}C 180° pulse during the first INEPT period.[44] This is particularly important for C5, C6, and C1' in which neighboring carbons can contribute significantly to R_1 (Equation 3.1). The remaining C-C dipolar auto-relaxation contribution is then explicitly taken into account in the model free analysis of the relaxation data. Other features implemented in the pulse sequences include use of selective off-resonance spin locks in the $R_{1\varrho}$ experiment that minimize Hartman-Hahn transfers to scalar coupled carbon spins, such as between C5-C6, C1'-C2', and C4/6-C8 to <0.1% maximum transfer efficiency. This was accomplished by ensuring that the difference in the effective field strengths experienced by two coupled carbon spins (C_x and C_y) is much greater than $^nJ_{xy}$ (Table 3.1).[19,44,75] The effects of CSA_C/DD_{CH} cross-correlated relaxation and C-H cross-relaxation are also suppressed by proton decoupling during the relaxation period.[71,72]

Figure 3.3b shows representative R_1 and $R_{1\varrho}$ fits obtained using the TD experiment. Mono-exponential behavior was observed in all cases, indicating the absence of any detectable C-C cross-relaxation and Hartman-Hahn transfer. Excellent agreement was also observed between the R_1 and $R_{1\varrho}$ rates measured using the TD and conventional experiment though the latter had ~24% and 82% greater fitting errors for R_1 and $R_{1\varrho}$, respectively (data not shown). Having confirmed the mono-exponential behavior of the TD relaxation experiments for all spins in E-TAR, an optimized sampling strategy[45,46] was adopted for the remaining experiments (see §3.2.1).
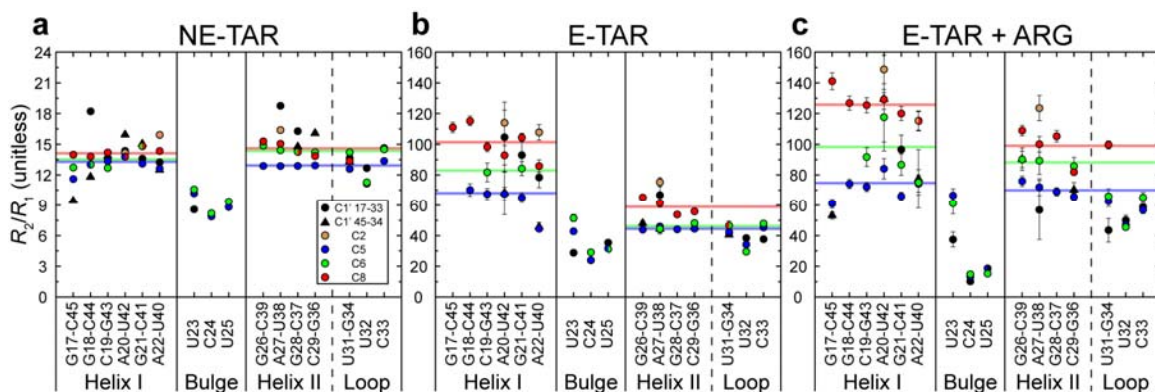
Figure 3.4. The carbon R_2/R_1 values for (a) free non-elongated TAR (NE-TAR), (b) free elongated TAR (E-TAR), and (c) elongated TAR in complex with ARG (E-TAR + ARG). Values for C1', C2, C5, C6, and C8 values are indicated in black, brown, blue, green, and red, respectively. Horizontal lines in blue, green, and red indicate the average R_2/R_1 value in a given helix for C5, C6, and C8, respectively.

3.3.3 Analysis of R_2/R_1 values

In Figure 3.4, we compare the carbon R_2/R_1 values measured in non-elongated TAR (NE-TAR) (Figure 3.4a), E-TAR (Figure 3.4b), and E-TAR bound to ARG (Figure 3.4c). Different R_2/R_1 values are observed for the various carbon types reflecting their inherently different relaxation mechanisms, and in particular, differences in R_1 due to differing numbers of C-C interactions. In NE-TAR, similar R_2/R_1 values were observed for the two helical domains. Normally, this would be interpreted as evidence that the RNA reorients as a rigid unit and that the two helices are therefore held rigid relative to one another. However, given the similar size of the two helices, one cannot rule out that they may reorient semi-independently of one another. These motions could go undetected, either because they cause similar reductions in the R_2/R_1 values observed in both helices, or because they occur at timescales slower than overall tumbling. Fortunately, domain-elongation resolves this ambiguity. Unlike NE-TAR, the R_2/R_1 values measured in the short helix of E-TAR are attenuated relative to counterparts measured in the elongated helix (Figure 3.4b). This uniform attenuation is observed across a variety of carbons, which have C-H, C-C, and CSA interaction tensors spanning diverse orientations in different residues. This suggests that the short helix moves collectively and semi-independently relative to the elongated helix at timescales faster

109

than the overall tumbling of E-TAR. This underscores that collective helix motions can easily go undetected in small non-elongated RNA such as NE-TAR. The addition of ARG to E-TAR leads to an increase in virtually all of the short helix R_2/R_1 values, including residues at the apical loop that are remote from the bulge ARG binding site, such that they are now far more similar to values measured in the elongated helix. This is exactly as would be expected if ARG were to arrest the collective helix motions in agreement with previous RDC studies.[56,63]

For both free NE-TAR and E-TAR, significantly attenuated R_2/R_1 values were observed for bulge residues, particularly the "spacer" residues C24 and U25, indicating that the inter-helix linker is highly flexible. However, the relative degree of attenuation is much greater for E-TAR, likely reflecting greater sensitivity to internal motions owing to its much slower overall molecular tumbling rate. An extreme example is that the E-TAR R_2/R_1 values appear to expose local mobility at the helix I A22-U40 base-pair that is not observed in NE-TAR. The addition of ARG does not significantly affect bulge residue U23, leads to apparent stabilization of the A22-U40 base-pair, and causes a dramatic reduction in R_2/R_1 and therefore an apparent increase in the local mobility of bulge residues C24 and U25, some of which have R_2/R_1 values approaching those observed in NE-TAR.

3.3.4 Orientational dependence of carbon relaxation data

Unlike the nearly isotropically tumbling NE-TAR (D_{ratio} ~ 2.0), spin relaxation in E-TAR (D_{ratio} ~ 4.7) strongly depends on the orientation of the principal axis (D_{zz}) of the axially symmetric rotational diffusion tensor relative to the relevant dipolar and CSA interaction tensors. Since the relative orientation of the C-H, C-C, and carbon CSA tensors can be assumed to be known, this orientational dependence can be specified based on the angles α^{CSA} and β^{CSA} that orient D_{zz} relative to the principal axis system (PAS) of the CSA tensor (Figure 3.5). This orientational dependence, together with the non-collinearity of C-C, C-H, and CSA interactions, makes the nucleobase carbon R_2/R_1 a

complex function of average orientation and internal and global motional parameters which cannot be interpreted as easily as R_2/R_1 values obtained for the case of an axially symmetric CSA that is co-linear with a single dominant dipolar interaction, as is normally assumed for amide and imino nitrogens.[76]
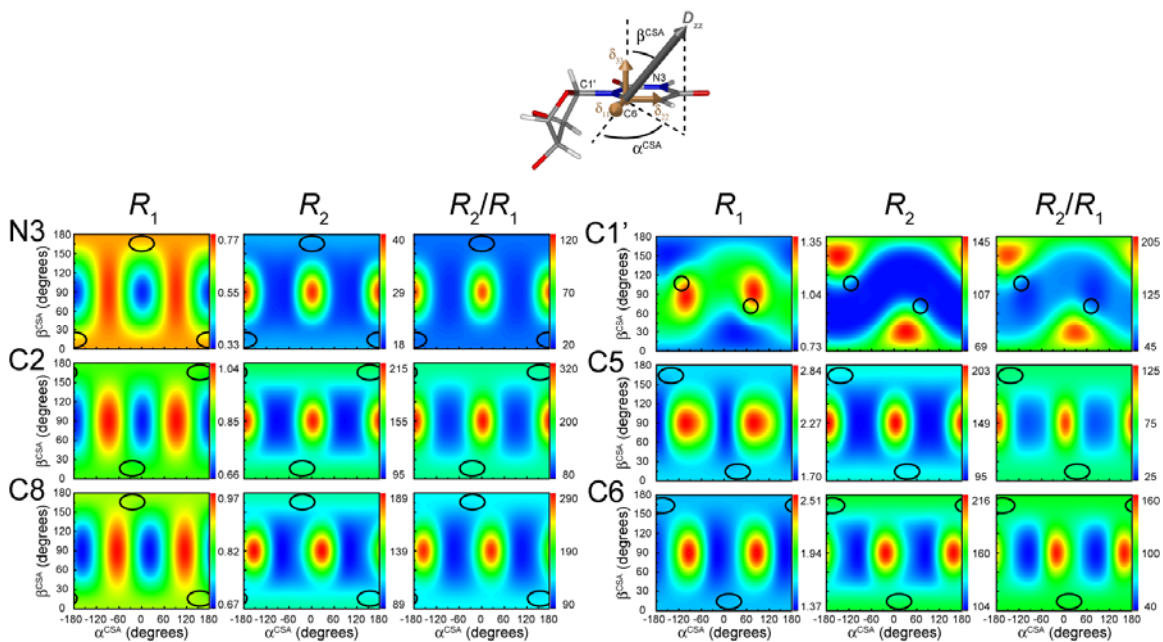

Figure 3.5. Orientational dependence of relaxation data in elongated RNA. Shown are the computed R_1, R_2, and R_2/R_1 values for imino nitrogen (N3) and carbons (C2 C5 C6 C8 C1') as a function of the orientation of the principal axis of diffusion (D_{zz}) relative to the principal axis system of the CSA tensor for each spin as defined by the polar angles α^{CSA} and β^{CSA}. The span of values is depicted to the right of each graph and range from the minimum (blue) to maximum (red) value attainable under the simulation conditions. The expected orientations for spins in the elongated RNA helix assuming D_{zz} is perfectly along the elongated helix axis are highlighted. Calculations assumed $\tau_m = 18.5$ ns, $D_{ratio} = 4.7$, $St^2 = 0.9$, and $\tau_{eff} = 100$ ps.

It has generally been assumed that the imino nitrogen CSAs are axially symmetric with principal direction (δ_{11}) oriented along the N-H dipolar vector. In this case, relaxation only depends on the angle between the N-H bond and D_{zz}. However, both solid-state NMR[70] and DFT studies[77] suggest that, like nucleobase carbons, the imino nitrogen CSAs, especially those in hydrogen bonded Watson-Crick base-pairs, are asymmetric and deviate from coincidence with the N-H dipolar vector (~20-30°). This modifies the orientational dependence of nitrogen relaxation by only a modest amount given that the CSA contribution remains small at 600 MHz. Nevertheless, this leads to observation of minimum and maximum R_2 and R_1 values, respectively, for orientations

in which D_{zz} is not only perpendicular to the N-H bond vector, but also to both the δ_{11} and δ_{33} principal axes of the CSA tensor (β ~90° and α ~90°) (Figure 3.5). The CSA orientational contributions are more pronounced for the nucleobase carbons due to their larger CSAs and, in the cases of C1', C5, and C6, the orientational dependence of R_1 is further modified by dependence on the orientation of C-C bonds (Figure 3.5). For C1', the orientational dependence is principally governed by the orientation of the C-H bond relative to D_{zz}, which is also non-coincident with the principal axes of the CSA tensor (Figure 3.5).

For imino nitrogens, the R_2/R_1 values measured in the elongated helix in which D_{zz} is assumed to be perfectly along the long axis of the E-RNA represent approximate lower bound values expected for a globally rigid structure. Only marginally smaller R_2/R_1 values (<10% of the range of R_2/R_1) can be observed for orientations that maintain the N-H dipolar vector and both δ_{11} and δ_{33} perpendicular to D_{zz}. Thus, the observation of R_2/R_1 values that are substantially lower than those measured in the elongated helix can to a good approximation be interpreted as evidence for internal motions. The more complicated orientational dependence of the carbon R_2 and R_2/R_1 is such that the values observed in the elongated helices do not correspond to perfect minima. Hence, the observation of attenuated R_2 and R_2/R_1 in regions outside the elongated helices cannot as easily be interpreted as evidence for internal motions since a similar degree of attenuation can arise from unique static orientations. This underscores the importance of taking into account the orientational dependence of various relaxation contributions in the dynamical interpretation of the relaxation data.

3.3.5 Model free analysis

The carbon and nitrogen relaxation data was analyzed using a model-free analysis that takes into account non-collinearity of relevant spin interactions and their distinct orientational dependencies. In principle, separate motional parameters need to be specified for each CSA, C-H, and C-C relaxation mechanism, as the interaction tensors

are all non-coincident to one another. As a first approximation, we assume that the interaction tensors experience identical isotropic internal motions. A recent molecular dynamics simulation of TAR revealed similar motional amplitudes for the nucleobase C-H and N-H bonds in a given residue.[53] With this assumption, a single set of motional parameters is needed to describe the internal motional amplitudes (S) and correlation times (τ). The spectral density function $g_2(\omega)$ by Spiess[48] can be used to take into account the asymmetry of the CSA under highly anisotropic diffusion. By expanding the function according to the extended model free formalism,[47] and including contributions from C-C and C-H dipolar interactions, one can interpret the relaxation data in terms of up to two distinct internal motional modes:[32,48,78]

$$g_2^\lambda(\omega) = \sum_{i=0}^{2} c_i^\lambda \left(\frac{S_f^2 S_s^2 \tau_i}{1+\omega^2 \tau_i^2} + \frac{(1-S_f^2)\tau_{i,f}}{1+\omega^2 \tau_{i,f}^2} + \frac{(S_f^2 - S_f^2 S_s^2)\tau_{i,s}}{1+\omega^2 \tau_{i,s}^2} \right) \tag{3.4}$$

where S_f^2 and S_s^2 are order parameters describing the amplitudes of the fast and slow internal motions and τ_F and τ_S describe their internal correlation times, respectively. $\tau_{i,n}^{-1} = \tau_i^{-1} + \tau_n^{-1}$ (i = 0, 1, 2 and n = f or s), in which τ_0^{-1} = 6 D_S – 2 D_a, τ_1^{-1} = 6 D_S – D_a and τ_2^{-1} = 6 D_S + 2 D_a with $D_a = D_{zz} - \frac{1}{2} (D_{xx} + D_{yy})$, $D_S = 1/3 (D_{xx} + D_{yy} + D_{zz})$, and $\tau_m = (6 D_S)^{-1}$. For axially symmetric overall diffusion, the coefficients c_i^λ are given by:

$$c_0^\lambda = \left(\frac{3\cos^2\beta^\lambda - 1}{2} - \frac{\eta^\lambda}{2}\cos(2\alpha^\lambda)\sin^2\beta^\lambda \right)^2$$

$$c_1^\lambda = \frac{1}{3}\left[\left(\frac{\eta^\lambda}{2}\cos(2\alpha^\lambda)\sin(2\beta^\lambda) + 3\cos\beta^\lambda\sin\beta^\lambda \right)^2 + \left(\eta^\lambda\sin(2\alpha^\lambda)\sin\beta^\lambda\right)^2 \right]$$

$$c_2^\lambda = \frac{1}{3}\left[\left(\frac{\eta^\lambda}{4}\cos(2\alpha^\lambda)\left(3 + \cos(2\beta^\lambda)\right) - \frac{3}{2}\sin^2\beta^\lambda \right)^2 + \left(\eta^\lambda\sin(2\alpha^\lambda)\cos\beta^\lambda\right)^2 \right] \tag{3.5}$$

in which η^λ is the asymmetry of the interaction (λ = CSA or DD) with $\eta_{CSA} = (\sigma_{xx} - \sigma_{yy})/\sigma_{zz}$ ≤ 1, and η_{DD} = 0. The angles α^λ and β^λ are the polar angles defining the orientation of the principal axis of diffusion (D_{zz}) relative to the axially symmetric dipolar (α^{DD} = 0 and β^{DD}) and asymmetric CSA (α^{CSA} and β^{CSA})) interaction frame. Note that DD includes both C-H

and C-C vectors, each of which have unique orientations relative to D_{zz}. Equation 3.4 has four unknown local parameters (S^2_f, S^2_s, τ_f, τ_s) whereas only 2 (3) measurements have been made for C1′, C5, and C6 (^{15}N, C2 and C8) nuclei. For this reason, the five standard single field models have been used in this study[66] and selected using Akaike's Information Criteria (AIC, see §3.2.2).[68]

Model 1 → $S^2_s = 1$, $S^2_f = S^2_t$, $\tau_f = \tau_s = 0$, $R_{ex} = 0$

Model 2 → $S^2_s = 1$, $S^2_f = S^2_t$, $\tau_s = 0$, $R_{ex} = 0$

Model 3 → $S^2_s = 1$, $S^2_f = S^2_t$, $\tau_f = \tau_s = 0$

Model 4 → $S^2_s = 1$, $S^2_f = S^2_t$, $\tau_s = 0$

Model 5 → $\tau_f = 0$, $R_{ex} = 0$

Deriving dynamical parameters from the relaxation data using Equations 3.1-3.5 is greatly facilitated by having a priori knowledge regarding the average orientation of spin interaction tensors (α^λ and β^λ) relative to D_{zz}. Though elongation is expected to align D_{zz} nearly perfectly along the elongated helix axis, deciphering the orientation of D_{zz} relative to other fragments such as helix II can be challenging, particularly for the globally flexible free E-TAR. In our study, we used the average orientation of the two helices as obtained from an order tensor analysis of RDCs recently measured in E-TAR[56] using Pf1 phage[52,53] as an ordering medium. The orientation of D_{zz} was assumed to be either equal to the RDC-derived principal orientation of alignment (S_{zz}) or perfectly along the elongated helix axis (similar results were obtained in the two cases). For the globally rigid and more well-defined TAR+ARG complex, the previous RDC-derived inter-helical orientation was assumed along with a hydrodynamically predicted D_{zz} orientation, as previously described.[25] The local structure of the bulge was modeled using previous NOE structures of TAR (1ANR for free TAR[35] and both 1ARJ[64] and 1AJU[65] for ARG-bound TAR). In all cases, the overall diffusion tensor was assumed to be axially symmetric with a hydrodynamically computed D_{ratio} value of 4.7±10%.

The inherently large uncertainty for the C1′, C5, and C6 NOEs due to C-C interactions[44] made it impossible to assess the validity of model 5 during the model selection for those spins. However, model 5 was selected consistently for the more isolated C2 and C8 carbons in helix II, for which more reliable NOE measurements were available, supporting the existence of at least two motional modes in helix II. Some carbons in helix I also resulted in selection of model 5. However, the total amplitude of motions (S^2_f x S^2_s) for these carbons remained comparable in magnitude to the corresponding S^2_f value obtained for carbons in helix I with models 1-3. For simplicity, we chose to report the total order parameter $S^2_t = S^2_f$ (models 1-4) or S^2_f x S^2_s (model 5) which, unlike the internal correlation time, is primarily dependent on $g_2(0)$ terms which can be accurately defined by the R_2 and R_1 rates. The much greater uncertainty in the internal correlation times (Tables 3.6-3.7) precluded their quantitative interpretation. However, any observable collective motions must occur at rates faster than overall diffusion.

The impact of using solution versus solid state CSAs[70] was also explored. For the majority of carbons (C1′, C5, and C8), this had a small impact on the derived motional parameters (rmsd between two S^2_t sets < 0.037), which is on the order of the variations expected due to measurement uncertainty (on average < 0.039). Larger differences were observed for C6 (rmsd ~ 0.074), for which the largest difference exists between the solution and solid state CSAs. The C6 S^2_t values obtained using the solution NMR CSAs were systematically smaller than all other carbons, including C5 on the same nucleobase in both free and ARG-bound TAR. Assuming that C5 and C6 in a given base should have similar motional parameters, the best agreement is observed when using the solution CSAs for C5[32] and solid state CSAs for C6.[70] It is noteworthy that the C6 CSAs were also the least reliably determined in the RCSA solution NMR study.[32] The main results shown in Figure 3.6 are therefore based on solution NMR CSAs for C1′, C2, C5, and C8 and the solid state NMR CSA for cytosine C6, which is assumed to be the same for uridine and cytosine. Finally, we note that small differences in the absolute magnitude of S^2_t were observed for various carbon types (Table 3.6-3.7). While this could

reflect real differences in the dynamics experienced by different carbons, for example due to anisotropic motions, it may also be the result of small discrepancies in calibrating the motionally averaged bond lengths and CSAs from carbon to carbon. In order to make comparisons between spin types, the S^2_t values have been normalized such that the highest value (lowest amplitude) for each nucleus is equal to 1.0.
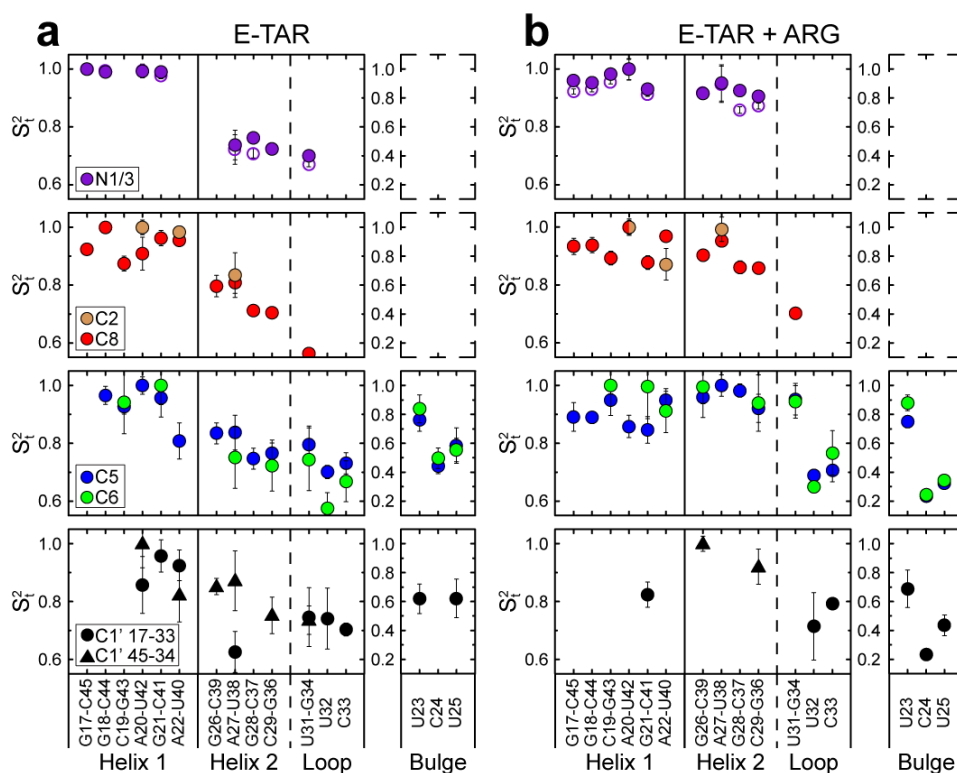

Figure 3.6. Amplitude of internal motions in free and ARG-bound TAR. The total spin relaxation order parameter $S^2_t = S^2_f \times S^2_s$ is shown for (a) free E-TAR and (b) E-TAR + ARG. The S^2_t values are normalized for a given carbon type (C1' C2 C5 C6 C8) and for nitrogen (N1 & N3) to have the maximum allowed value of 1. Conservative error bars account for uncertainty in the measurement, CSA, and D_{zz} orientation (see §3.2.2).

The normalized carbon S^2_t values in free and ARG-bound TAR are shown in Figure 3.6. Conservative error bars are shown to account for uncertainty in the measurement, D_{zz} orientation (~6°), and CSAs (see §3.2.2). The motional parameters obtained for the imino nitrogen relaxation data when conducting the analysis assuming asymmetric CSAs that are non-collinear with the N-H dipolar vector are in excellent agreement with those reported previously when assuming axially symmetric CSAs that are collinear with the N-H dipolar vector.[25] This is not surprising given that CSA contribution to

nitrogen relaxation is relatively small at 600 MHz (15%). In addition, the nitrogen motional parameters changed very little when analyzed with or without carbon relaxation data in free and ARG-bound E-TAR (S^2_t rmsd < 0.02), indicating that the two sets of data are mutually consistent with one another. Despite the large C6 uncertainty, similar S^2_t values are observed for C5 and C6 in a given nucleobase. Likewise, similar S^2_t values are observed for carbon and nitrogen spins on the same uridine or guanine nucleobase. This lends support to our assumption that the different interaction tensors experience similar internal motions.

3.3.6 Internal motions in free and ARG-bound E-TAR

With the exception of U40 at the junction of the two helices, limited local mobility is observed in the elongated helix (S^2_t ~0.9 – 1.0) in both free (Figure 3.6a) and ARG-bound (Figure 3.6b) E-TAR. The high local mobility observed for both the base (C5) and sugar (C1′) in U40 helps explain why its imino proton is exchange broadened out of detection and why it does not form the predicted Watson-Crick hydrogen bond alignment with A22.[63] In contrast, the greater rigidity observed for the nucleobase of A22 is in agreement with the NMR structure of free TAR which shows A22 stacking between U23 and G21.[35] Importantly, the mobility at U40 is arrested upon ARG binding which is consistent with formation of the A22-U40 Watson-Crick hydrogen bond alignment upon ARG recognition.[63]

In free E-TAR, the S^2_t values observed for the shorter helix II are consistently smaller than counterparts in the elongated helix (Figure 3.6a). Similar levels of attenuation (~0.75-0.85 %) are observed for the various carbon and nitrogen spins in the locally stable Watson-Crick base-pairs, consistent with a single collective dynamical process that reorients helix II relative to helix I. Although less reliably determined by the relaxation data, the time constant for the slow collective process as obtained by C8 for which NOEs were available (0.8 ± 0.6 ns) is in reasonable agreement with those obtained by nitrogen relaxation (1.4 ± 0.1 ns) and support that the collective motions are diffusion

117

limited fluctuations that occur at timescales approaching the predicted overall correlation time for the short helix II.[25] Even smaller S^2_t values are observed for the apical loop residues U32 and C33, which have been shown previously by carbon[19] and deuterium[15] relaxation to be the most locally flexible residues in the UUCG loop. These residues likely experience a combination of collective and local motions. ARG binding leads to the arrest of collective helix motions, as indicated by an increase in the S^2_t value of virtually every residue in the short helix, including residues at the tip of the helix in the apical loop which show no chemical shift perturbations upon ARG binding. The ARG induced arrest of collective motions, which has previously also been independently reported by RDCs,[63] exposes local mobility at residues U32 and C33 in the apical loop as a persistent attenuation in S^2_t.

The carbon relaxation data allowed us to quantitatively characterize internal motions in bulge residues for which no suitable imino nitrogen probes are available. For free E-TAR, restricted mobility was observed for the nucleobase of the highly conserved U23 residues, which is critical for Tat recognition, and is in good agreement with NMR structures of free TAR which show that U23 stacks on A22 (Figure 3.6a).[64] In contrast, very high mobility (S^2_t ~0.4-0.6) was observed for the sugar backbone of U23 C1', which likely facilitates collective motions between the two helices, as well as the nucleobases of C24 and U25, which are only involved in partial stacking interactions (Figure 3.6a). [64] The limited mobility at U23 is not greatly affected by ARG binding (Figure 3.6b), consistent with the replacement of stacking interactions with a U23-A27-U38 base-triple alignment in the ARG-bound state.[34] In contrast, a dramatic increase in the local mobility of residues C24 and U25 is observed, indicating that they essentially undergo spatially unrestricted motions in the ARG-bound state (S^2_t ~0.2, Figure 3.6b). To the best of our knowledge, the S^2_t values observed for these residues are the smallest reported to date in nucleic acids. The large motional amplitudes observed at C24 and U25 is consistent with their looped out geometry in the TAR+ARG complex in which they are not involved in any interactions.[34,35] These results show that complex formation need not solely be accompanied by conformational stabilization. Rather, mobility in the form of collective

helix motions is conserved as local motions in the linker while the inter-helix orientation is stabilized in the E-TAR+ARG complex.

Two factors can complicate interpretation of relaxation data in the bulge. First, the carbon CSAs may significantly deviate from values in A-form helices. It is well known that changes in the chemical environment and hydrogen bonding can lead to changes in all five elements of the CSA tensor.[50,79,80] However, virtually identical S^2_t values were obtained when using the mononucleotide CSAs obtained by solid-state NMR,[70] even for C6 for which the CSAs are quite different. Second, an average conformation can be difficult to define for these highly flexible residues. However, repeating the analysis using different input bulge conformations from as many as 40 NMR models (see §3.2.2) also had a negligible impact on the derived S^2_t values. Thus, the high degree of internal mobility at these sites renders analysis of relaxation data far less sensitive to the details of the CSA and average structure. This suggests that carbon relaxation will provide insights into the dynamics of extremely flexible regions in RNA with high tolerance to potential deviations in the CSAs or lack of knowledge regarding average conformation.

3.3.7 Role of internal motions in TAR adaptation

We previously provided evidence based on qualitative analysis of resonance intensities in E-TAR that the extent of internal motions at various sites in TAR correlates with the degree to which a given site changes conformation in response to recognition of seven distinct small molecule and ligand targets.[25] Specifically, we observed a correlation (R = 0.8) between the normalized intensity observed for a given C-H site in 2D HSQC spectra of E-TAR and the mean angular deviation of the C-H bond ($\Delta\theta$) obtained following superposition of the reference helix I. The latter provides a qualitative measure of the conformational freedom available to a given bond when adapting conformation to bind different targets. With the determination of quantitative order parameters for various sites, we were able to re-visit this correlation devoid of the complications that enter analysis of resonance intensities in terms of dynamics,

including chemical exchange and the strong orientational dependence of relaxation. As shown in Figure 3.7, a plot of $\Delta\theta$ versus the $1-S^2$ reveals a correlation with a similar R factor of 0.80. Thus, sites that undergo the largest changes in conformation upon ligand recognition also undergo the largest amplitude internal motions in the free state at rates faster than overall diffusion. This provides supporting evidence that intrinsic internal dynamics in TAR play a role in how its conformation adapts upon binding to distinct molecular targets.
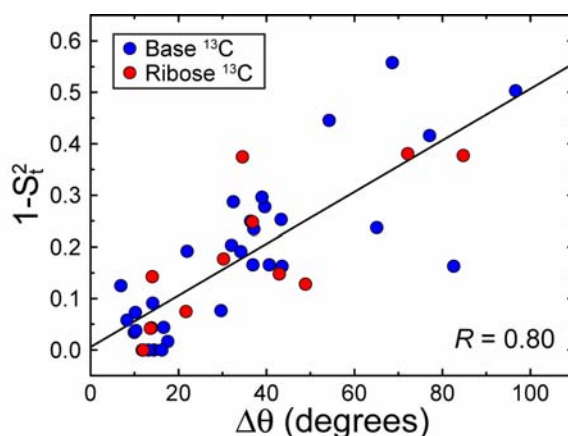

Figure 3.7. Role of internal motions in TAR adaptation. Shown is a correlated plot between $1-S^2_t$ and the mean angular difference ($\Delta\theta$) in the orientation of individual sugar (red) and nucleobase (blue) C-H bonds in seven distinct ligand bound structures of TAR obtained following superposition of helix I as described previously.[25]

3.4 Conclusions

By decoupling internal motions from overall reorientation, domain-elongation provides the basis for quantitatively characterizing picosecond-nanosecond internal motions in RNA by NMR relaxation methods. Elongation does however accentuate potentially unfavorable effects in carbon relaxation studies that grow with molecular weight and structural anisotropy, including the magnitude of C-C relaxation contributions, orientational dependence of relaxation data due to multiple dipolar interactions and highly asymmetric CSAs. Our study suggests that the latter problems can be overcome by combined use of appropriate pulse sequences, analytical methods

and by taking advantage of structural and diffusion tensor orientation information from the measurement of RDCs.

Of particular importance in studies of E-RNA is to have accurate information regarding the asymmetric nucleobase carbon CSAs, including their orientation, which can normally be ignored in isotropically tumbling systems. In this regard, our study benefited tremendously from recent advances in using RCSAs to measure CSAs under solution conditions[30-32] which when combined with previously reported solid-state NMR values,[70] provide a basis for exploring the potential error arising from CSA uncertainty. Our results suggest that, with the exception of C6, the errors in motional amplitudes for our targeted carbons due to potential variations in CSA are only slightly higher than the error contribution from typical measurement uncertainty. This error contribution becomes smaller with increasing mobility, making analysis of relaxation data highly tolerant to potentially large CSA variations in flexible non-helical regions.

A potentially much larger source of uncertainty in the analysis of the carbon relaxation data is the orientation of the D_{zz} relative to the RNA structure. Relative to the ideal nitrogen spins, the determination of the overall diffusion tensor parameters by the carbon relaxation data is made more difficult by the more complex dependence of R_2/R_1 on orientational and motional parameters. Clearly, the measurement of additional relaxation data, including at different magnetic fields, can help define the complex model free parameter space. In our study, we took advantage of RDCs both in defining an average RNA conformation over sub-millisecond timescales and in defining the average orientation of D_{zz} relative to helices I and II.[56] In the latter, we assumed that the principal axis of alignment (S_{zz}) in phage ordering media is identical to D_{zz}, which seems to be a reasonable assumption given that both properties are primarily governed by the overall molecular shape of the elongated RNA. For highly flexible regions such as bulge residues C24 and U25, the model free analysis is considerably less sensitive to the orientation of D_{zz}.

Our study of TAR confirmed the presence of complex heterogeneous dynamics consisting of local and collective motions that were previously inferred based on a smaller number of imino nitrogen relaxation data and qualitative analysis of motional narrowing of resonances.[25] It also revealed that the internal motions can undergo complex reorganization upon ligand recognition involving a combination of stabilization and, surprisingly, dramatic increases in local mobility. Both the local and collective motions in TAR occur at rates that approach or are slower than the overall molecular tumbling of non-elongated RNAs, and suggest a spectrum of local and collective motions exist at nanosecond to microsecond timescales. By expanding the types of relaxation data that is measured, it may be possible to define the timescale and anisotropy of motions as well as long-range aspects of RNA structure.

3.5 References

1. Al-Hashimi, H.M. Dynamics-based amplification of RNA function and its characterization by using NMR spectroscopy. *Chembiochem* **6**, 1506-1519 (2005).

2. Micura, R. & Hobartner, C. On secondary structure rearrangements and equilibria of small RNAs. *Chembiochem* **4**, 984-990 (2003).

3. Leulliot, N. & Varani, G. Current topics in RNA-protein recognition: Control of specificity and biological function through induced fit and conformational capture. *Biochemistry* **40**, 7947-7956 (2001).

4. Williamson, J.R. Induced fit in RNA-protein recognition. *Nature Structural Biology* **7**, 834-837 (2000).

5. Mandal, M. & Breaker, R.R. Gene regulation by riboswitches. *Nature Reviews Molecular Cell Biology* **5**, 451-463 (2004).

6. Schwalbe, H., Buck, J., Furtig, B., Noeske, J. & Wohnert, J. Structures of RNA switches: Insight into molecular recognition and tertiary structure. *Angewandte Chemie-International Edition* **46**, 1212-1219 (2007).

7. Lilley, D.M. Analysis of global conformational transitions in ribozymes. *Methods Mol Biol.* **252**, 77-108. (2004).

8. Walter, N.G. & Engelke, D.R. Ribozymes: catalytic RNAs that cut things, make things, and do odd and useful jobs. *Biologist (London).* **49**, 199-203. (2002).

9. Furtig, B. et al. Time-resolved NMR studies of RNA folding. *Biopolymers* **86**, 360-383 (2007).

10. Getz, M., Sun, X.Y., Casiano-Negroni, A., Zhang, Q. & Al-Hashimi, H.M. NMR studies of RNA dynamics and structural plasticity using NMR residual dipolar couplings. *Biopolymers* **86**, 384-402 (2007).

11. Palmer, A.G. & Massi, F. Characterization of the dynamics of biomacromolecules using rotating-frame spin relaxation NMR spectroscopy. *Chemical Reviews* **106**, 1700-1719 (2006).

12. Mittermaier, A. & Kay, L.E. Review - New tools provide new insights in NMR studies of protein dynamics. *Science* **312**, 224-228 (2006).

13. Shajani, Z. & Varani, G. NMR studies of dynamics in RNA and DNA by C-13 relaxation. *Biopolymers* **86**, 348-359 (2007).

14. Lipari, G. & Szabo, A. Model-Free Approach To The Interpretation Of Nuclear Magnetic-Resonance Relaxation In Macromolecules.1. Theory And Range Of Validity. *Journal Of The American Chemical Society* **104**, 4546-4559 (1982).

15. Vallurupalli, P. & Kay, L.E. A suite of H-2 NMR spin relaxation experiments for the measurement of RNA dynamics. *Journal Of The American Chemical Society* **127**, 6893-6901 (2005).

16. Williamson, J.R. & Boxer, S.G. Synthesis Of A Thymidine Phosphoramidite Labeled With C-13 At C6 - Relaxation Studies Of The Loop Region In A C-13 Labeled DNA Hairpin. *Nucleic Acids Research* **16**, 1529-1540 (1988).

17. Hall, K.B. & Tang, C.G. C-13 relaxation and dynamics of the purine bases in the iron responsive element RNA hairpin. *Biochemistry* **37**, 9323-9332 (1998).

18. Boisbouvier, J., Wu, Z.R., Ono, A., Kainosho, M. & Bax, A. Rotational diffusion tensor of nucleic acids from C-13 NMR relaxation. *Journal Of Biomolecular NMR* **27**, 133-142 (2003).

19. Duchardt, E. & Schwalbe, H. Residue specific ribose and nucleobase dynamics of the cUUCGg RNA tetraloop motif by NMR C-13 relaxation. *Journal Of Biomolecular NMR* **32**, 295-308 (2005).

20. Shajani, Z. & Varani, G. C-13 NMR relaxation studies of RNA base and ribose nuclei reveal a complex pattern of motions in the RNA binding site for human U1A protein. *Journal Of Molecular Biology* **349**, 699-715 (2005).

21. Ravindranathan, S., Kim, C.H. & Bodenhausen, G. Determination of C-13 CSA tensors: Extension of the model-independent approach to an RNA kissing complex undergoing anisotropic rotational diffusion in solution. *Journal Of Biomolecular NMR* **33**, 163-174 (2005).

22. Johnson, J.E., Julien, K.R. & Hoogstraten, C.G. Alternate-site isotopic labeling of ribonucleotides for NMR studies of ribose conformational dynamics in RNA. *Journal Of Biomolecular NMR* **35**, 261-274 (2006).

23. Sun, X.Y., Zhang, Q. & Al-Hashimi, H.M. Resolving fast and slow motions in the internal loop containing stem-loop 1 of HIV-1 that are modulated by Mg2+ binding: role in the kissing-duplex structural transition. *Nucleic Acids Research* **35**, 1698-1713 (2007).

24. Shajani, Z., Drobny, G. & Varani, G. Binding of U1A protein changes RNA dynamics as observed by C-13 NMR relaxation studies. *Biochemistry* **46**, 5875-5883 (2007).

25. Zhang, Q., Sun, X.Y., Watt, E.D. & Al-Hashimi, H.M. Resolving the motional modes that code for RNA adaptation. *Science* **311**, 653-656 (2006).

26. Getz, M.M., Andrews, A.J., Fierke, C.A. & Al-Hashimi, H.M. Structural plasticity and Mg2+ binding properties of RNase PP4 from combined analysis of NMR residual dipolar couplings and motionally decoupled spin relaxation. *RNA-A Publication Of The RNA Society* **13**, 251-266 (2007).

27. Showalter, S.A. & Hall, K.B. Isotropic reorientational eigenmode dynamics complements NMR relaxation measurements for RNA. in *Nuclear Magnetic Resonance Of Biological Macromolecules, Part C*, Vol. 394 465-480 (2005).

28. Zhang, Q., Throolin, R., Pitt, S.W., Serganov, A. & Al-Hashimi, H.M. Probing motions between equivalent RNA domains using magnetic field induced residual dipolar couplings: Accounting for correlations between motions and alignment. *Journal Of The American Chemical Society* **125**, 10530-10531 (2003).

29. Showalter, S.A., Baker, N.A., Tang, C.G. & Hall, K. Iron responsive element RNA flexibility described by NMR and isotropic reorientational eigenmode dynamics. *Journal Of Biomolecular NMR* **32**, 179-193 (2005).

30. Bryce, D.L., Grishaev, A. & Bax, A. Measurement of ribose carbon chemical shift tensors for A-form RNA by liquid crystal NMR spectroscopy. *Journal Of The American Chemical Society* **127**, 7387-7396 (2005).

31. Hansen, A.L. & Al-Hashimi, H.M. Insight into the CSA tensors of nucleobase carbons in RNA polynucleotides from solution measurements of residual CSA: Towards new long-range orientational constraints. *Journal Of Magnetic Resonance* **179**, 299-307 (2006).

32. Ying, J.F., Grishaev, A., Bryce, D.L. & Bax, A. Chemical shift tensors of protonated base carbons in helical RNA and DNA from NMR relaxation and liquid crystal measurements. *Journal Of The American Chemical Society* **128**, 11443-11454 (2006).

33. Boisbouvier, J., Brutscher, B., Simorre, J.P. & Marion, D. C-13 spin relaxation measurements in RNA: Sensitivity and resolution improvement using spin-state selective correlation experiments. *Journal Of Biomolecular NMR* **14**, 241-252 (1999).

34. Puglisi, J.D., Tan, R.Y., Calnan, B.J., Frankel, A.D. & Williamson, J.R. Conformation Of The Tar RNA-Arginine Complex By NMR-Spectroscopy. *Science* **257**, 76-80 (1992).

35. Aboul-ela, F., Karn, J. & Varani, G. Structure of HIV-1 TAR RNA in the absence of ligands reveals a novel conformation of the trinucleotide bulge. *Nucleic Acids Research* **24**, 3974-3981 (1996).

36. Bannwarth, S. & Gatignol, A. HIV-1 TAR RNA: The target of molecular interactions between the virus and its host. *Current Hiv Research* **3**, 61-71 (2005).

37. Delaglio, F. et al. NMRpipe - A Multidimensional Spectral Processing System Based On Unix Pipes. *Journal Of Biomolecular NMR* **6**, 277-293 (1995).

38. Johnson, B.A. & Blevins, R.A. NMR View - A Computer-Program For The Visualization And Analysis Of NMR Data. *Journal Of Biomolecular NMR* **4**, 603-614 (1994).

39. Igumenova, T.I. & Palmer, A.G. Off-resonance TROSY-selected R-1p experiment with improved sensitivity for medium- and high-molecular-weight proteins. *Journal Of The American Chemical Society* **128**, 8110-8111 (2006).

40. Zhu, G., Xia, Y.L., Nicholson, L.K. & Sze, K.H. Protein dynamics measurements by TROSY-based NMR experiments. *Journal Of Magnetic Resonance* **143**, 423-426 (2000).

41. Loria, J.P., Rance, M. & Palmer, A.G. A TROSY CPMG sequence for characterizing chemical exchange in large proteins. *Journal Of Biomolecular NMR* **15**, 151-155 (1999).

42. Mulder, F.A.A., de Graaf, R.A., Kaptein, R. & Boelens, R. An off-resonance rotating frame relaxation experiment for the investigation of macromolecular dynamics using adiabatic rotations. *Journal Of Magnetic Resonance* **131**, 351-357 (1998).

43. Palmer, A.G., Kroenke, C.D. & Loria, J.P. Nuclear magnetic resonance methods for quantifying microsecond-to-millisecond motions in biological macromolecules. in *Nuclear Magnetic Resonance Of Biological Macromolecules, Pt B*, Vol. 339 204-238 (2001).

44. Yamazaki, T., Muhandiram, R. & Kay, L.E. NMR Experiments For The Measurement Of Carbon Relaxation Properties In Highly Enriched, Uniformly C-13,N-15-Labeled Proteins - Application To C-13(Alpha) Carbons. *Journal Of The American Chemical Society* **116**, 8266-8278 (1994).

45. Jones, J.A. Optimal sampling strategies for the measurement of relaxation times in proteins. *Journal Of Magnetic Resonance* **126**, 283-286 (1997).

46. Jones, J.A., Hodgkinson, P., Barker, A.L. & Hore, P.J. Optimal sampling strategies for the measurement of spin-spin relaxation times. *Journal Of Magnetic Resonance Series B* **113**, 25-34 (1996).

47. Clore, G.M. et al. Deviations From The Simple 2-Parameter Model-Free Approach To The Interpretation Of N-15 Nuclear Magnetic-Relaxation Of Proteins. *Journal Of The American Chemical Society* **112**, 4989-4991 (1990).

48. Spiess, H.W. Rotation of Molecules and Nuclear Spin Relaxation. *NMR - Basic Principles and Progress* **15**, 55-214 (1978).

49. Case, D.A. Calculations of NMR dipolar coupling strengths in model peptides. *Journal Of Biomolecular NMR* **15**, 95-102 (1999).

50. Czernek, J. An ab initio study of hydrogen bonding effects on the N-15 and H-1 chemical shielding tensors in the Watson-Crick base pairs. *Journal Of Physical Chemistry A* **105**, 1357-1365 (2001).

51. Hallock, K.J., Lee, D.K. & Ramamoorthy, A. The effects of librations on the C-13 chemical shift and H-2 electric field gradient tensors in beta-calcium formate. *Journal Of Chemical Physics* **113**, 11187-11193 (2000).

52. Hansen, M.R., Mueller, L. & Pardi, A. Tunable alignment of macromolecules by filamentous phage yields dipolar coupling interactions. *Nature Structural Biology* **5**, 1065-1074 (1998).

53. Clore, G.M., Starich, M.R. & Gronenborn, A.M. Measurement of residual dipolar couplings of macromolecules aligned in the nematic phase of a colloidal suspension of rod-shaped viruses. *Journal Of The American Chemical Society* **120**, 10571-10572 (1998).

54. Saupe, A. Recent Results In Field Of Liquid Crystals. *Angewandte Chemie-International Edition* **7**, 97-& (1968).

55. Musselman, C. et al. Impact of static and dynamic A-form heterogeneity on the determination of RNA global structural dynamics using NMR residual dipolar couplings. *Journal Of Biomolecular NMR* **36**, 235-249 (2006).

56. Zhang, Q., Stelzer, A.C., Fisher, C.K. & Al-Hashimi, H.M. Visualizing spatially correlated dynamics that directs RNA conformational transitions. *Nature* **450**, 1263-U14 (2007).

57. Tjandra, N. & Bax, A. Direct measurement of distances and angles in biomolecules by NMR in a dilute liquid crystalline medium (vol 278, pg 1111, 1997). *Science* **278**, 1697-1697 (1997).

58. Tjandra, N. & Bax, A. Direct measurement of distances and angles in biomolecules by NMR in a dilute liquid crystalline medium. *Science* **278**, 1111-1114 (1997).

59. Bax, A. & Tjandra, N. High-resolution heteronuclear NMR of human ubiquitin in an aqueous liquid crystalline medium. *Journal Of Biomolecular NMR* **10**, 289-292 (1997).

60. van Dijk, A.D.J., Fushman, D. & Bonvin, A. Various strategies of using residual dipolar couplings in NMR-driven protein docking: Application to Lys48-linked Di-ubiquitin and validation against N-15-relaxation data. *Proteins Structure Function And Bioinformatics* **60**, 367-381 (2005).

61. de la Torre, J.G., Huertas, M.L. & Carrasco, B. HYDRONMR: Prediction of NMR relaxation of globular proteins from atomic-level structures and hydrodynamic calculations. *Journal Of Magnetic Resonance* **147**, 138-146 (2000).

62. Zweckstetter, M. & Bax, A. Prediction of sterically induced alignment in a dilute liquid crystalline phase: Aid to protein structure determination by NMR. *Journal Of The American Chemical Society* **122**, 3791-3792 (2000).

63. Pitt, S.W., Majumdar, A., Serganov, A., Patel, D.J. & Al-Hashimi, H.M. Argininamide binding arrests global motions in HIV-1 TAR RNA: Comparison with Mg2+-induced conformational stabilization. *Journal Of Molecular Biology* **338**, 7-16 (2004).

64. Aboul-ela, F., Karn, J. & Varani, G. The Structure Of The Human-Immunodeficiency-Virus Type-1 TAR RNA Reveals Principles Of RNA Recognition By Tat Protein. *Journal Of Molecular Biology* **253**, 313-332 (1995).

65. Brodsky, A.S. & Williamson, J.R. Solution structure of the HIV-2 TAR-argininamide complex. *Journal Of Molecular Biology* **267**, 624-639 (1997).

66. Mandel, A.M., Akke, M. & Palmer, A.G. Backbone Dynamics Of Escherichia-Coli Ribonuclease Hi - Correlations With Structure And Function In An Active Enzyme. *Journal Of Molecular Biology* **246**, 144-163 (1995).

67. Nelder, J.A. & Mead, R. A Simplex-Method For Function Minimization. *Computer Journal* **7**, 308-313 (1965).

68. d'Auvergne, E.J. & Gooley, P.R. Model-free model elimination: A new step in the model-free dynamic analysis of NMR relaxation data. *Journal Of Biomolecular NMR* **35**, 117-135 (2006).

69. d'Auvergne, E.J. & Gooley, P.R. The use of model selection in the model-free analysis of protein dynamics. *Journal Of Biomolecular NMR* **25**, 25-39 (2003).

70. Stueber, D. & Grant, D.M. C-13 and N-15 chemical shift tensors in adenosine, guanosine dihydrate, 2 '-deoxythymidine, and cytidine. *Journal Of The American Chemical Society* **124**, 10539-10551 (2002).

71. Korzhnev, D.M., Skrynnikov, N.R., Millet, O., Torchia, D.A. & Kay, L.E. An NMR experiment for the accurate measurement of heteronuclear spin-lock relaxation rates. *Journal Of The American Chemical Society* **124**, 10743-10753 (2002).

72. Massi, F., Johnson, E., Wang, C.Y., Rance, M. & Palmer, A.G. NMR R-1 rho rotating-frame relaxation with weak radio frequency fields. *Journal Of The American Chemical Society* **126**, 2247-2256 (2004).

73. Pervushin, K., Riek, R., Wider, G. & Wuthrich, K. Attenuated T-2 relaxation by mutual cancellation of dipole-dipole coupling and chemical shift anisotropy indicates an avenue to NMR structures of very large biological macromolecules in solution. *Proceedings Of The National Academy Of Sciences Of The United States Of America* **94**, 12366-12371 (1997).

74. Brutscher, B., Boisbouvier, J., Pardi, A., Marion, D. & Simorre, J.P. Improved sensitivity and resolution in H-1-C-13 NMR experiments of RNA. *Journal Of The American Chemical Society* **120**, 11845-11851 (1998).

75. Bax, A. & Davis, D.G. Practical Aspects Of Two-Dimensional Transverse Noe Spectroscopy. *Journal Of Magnetic Resonance* **63**, 207-213 (1985).

76. Tjandra, N., Feller, S.E., Pastor, R.W. & Bax, A. Rotational diffusion anisotropy of human ubiquitin from N-15 NMR relaxation. *Journal Of The American Chemical Society* **117**, 12562-12566 (1995).

77. Czernek, J., Fiala, R. & Sklenar, V. Hydrogen bonding effects on the N-15 and H-1 shielding tensors in nucleic acid base pairs. *Journal Of Magnetic Resonance* **145**, 142-146 (2000).

78. Chang, S.L. & Tjandra, N. Temperature dependence of protein backbone motion from carbonyl C-13 and amide N-15 NMR relaxation. *Journal Of Magnetic Resonance* **174**, 43-53 (2005).

79. Hall, J.B. & Fushman, D. Variability of the N-15 chemical shielding tensors in the B3 domain of protein G from N-15 relaxation measurements at several fields. Implications for backbone order parameters. *Journal Of The American Chemical Society* **128**, 7855-7870 (2006).

80. Poon, A., Birn, J. & Ramamoorthy, A. How does an amide-N-15 chemical shift tensor vary in peptides? *Journal Of Physical Chemistry B* **108**, 16577-16585 (2004).

Chapter 4. Characterizing μs-ms Exchange in Labeled and Unlabeled Nucleic Acids by Carbon $R_{1\varrho}$ NMR

4.1 Introduction

Internal motions occurring at micro-to-millisecond timescales play essential roles in the functions of nucleic acids.[1,2] Relaxation dispersion Nuclear Magnetic Resonance (NMR) spectroscopy is one of the few techniques that can be used to site-specifically quantify these motions.[3,4] This involves monitoring the transverse relaxation rate (R_2) of signals from nuclei that exchange between chemically distinct states via so-called $R_{1\varrho}$ or Carr-Purcell-Meiboom-Gill (CPMG) experiments as a function of various controllable experimental parameters. $R_{1\varrho}$ carbon relaxation dispersion has provided unique insights into such site-specific processes in nucleic acids,[5,6] although studies so far have employed effective radiofrequency fields in the range of 1-6 kHz thus limiting sensitivity to exchange processes occurring at ~25 to 160 microsecond timescales. Slower millisecond motions can in principle be accessed by CPMG relaxation dispersion experiments, but extensive C-C scalar coupling networks in base and sugar moieties of nucleic acids can severely complicate these experiments.[7] The multi-dimensional relaxation dispersion experiments also remain prohibitively time-consuming for carrying out measurements at natural abundance. This has made it difficult to characterize a large class of functional dynamics occurring at chemically modified sites that are difficult to enrich isotopically.

Here, we present a carbon $R_{1\varrho}$ NMR experiment (Figure 4.1) that extends accessible timescales to ~10 ms and that can be applied to both uniformly labeled and unlabeled nucleic acid samples. Sensitivity to slower motions can be achieved through the appropriate use of ^{1}H decoupling and magnetization aligning schemes that permit use of

significantly weaker RF fields (25-1000 Hz) as described by Palmer[8] and Kay[9] for amide ^{15}N in proteins. We have adapted the scheme introduced by Kay et al. for measuring nitrogen off-resonance $R_{1\varrho}$ in proteins in designing the pulse sequence shown in Figure 4.1 which is optimized to measure off-resonance $R_{1\varrho}$ for protonated carbons in uniformly labeled and unlabelled nucleic acids.

4.2 Methods

4.2.1 Sample Preparation and Assignment

The uniformly ^{13}C/^{15}N labeled A-site rRNA sample was prepared by <u>in vitro</u> transcription using synthetic double stranded DNA templates containing a T7 promoter and the A-site rRNA sequence of interest (Integrated DNA Technologies, Inc.), T7 RNA polymerase (Takara Mirus Bio, Inc.), and ^{13}C/^{15}N labeled nucleotide triphosphates (Cambridege Isotiopes, Inc.). The RNA was purified by 20% (w/v) denaturing polyacrylamide gel electrophoresis containing 8M urea and 1x TBE followed by electroelution in 20 mM Tris pH 8 buffer and ethanol precipitation. The RNA pellet was dissolved and exchanged into NMR buffer (15 mM sodium phosphate, 0.1 mM EDTA, and 25 mM NaCl at pH ~6.4) using a Centricon Ultracel YM-3 concentrator (Millipore Corp.). The final NMR sample had an RNA concentration of ~1mM NMR buffer and 10% D_2O. The A-site rRNA NMR spectra were assigned using conventional NMR methods such as 3D exchangeable ^{1}H-^{15}N NOESY-HSQC, 3D non-exchangeable ^{1}H-^{13}C NOESY-HSQC, 2D HCN[10], HCCH-COSY (correlates H2/H8 resonances)[11,12], 2D IP-COSY (correlated H5/H6 resonances).[13,14] The assignments were further verified with previous assignments.[15]

Unmodified DNA oligonucleotides were purchased from IDT, Inc. (Coralville, IA) and purified by standard desalting. The gel filtration grade 1,N6-ethenoadenine modified oligonucleotide (5' GATCCTeACCTTCG 3') was purchased from Midland Certified Reagent Company, Inc. (Midland, TX). The sequences for the control (A-DNA)

and damaged (eA-DNA) duplex were identical (5′ CGAAGGTAGGATC[G]/ [C]GATCCTXCCTTCG 3′) except for the damaged residue (X = eA or A) and a terminal base pair substitution (in brackets) introduced in A-DNA to prevent spectral overlap of the target adenine. The DNA oligos were resuspended in 10mM Na-MES (pH 6.1), 100 mM NaCl, 0.1 mM DTT, 0.1 mM EDTA buffer at ~200 µM concentrations. Duplexes were annealed by mixing an equal molar ratio of the complementary DNA strands, heating for 2 min at 95°C and gradual cooling (~30 min) at room temperature. DNA preparations were further washed 3X in resuspension buffer by micro-centrifugation using an Amicon Ultra-4 centrifugal filter (3 kDa cutoff), concentrated to ~ 250 µl (~5 mM) for NMR studies and supplied with 10% D_2O. Exchangeable and non-exchangeable protons of the unlabeled DNA duplexes were assigned using conventional NMR methods (^1H,^1H-NOESY) at 25°C in 10% D_2O.[16] The assignments for the adenine adduct were consistent with previous assignments.[17]   All 2D ^{13}C-^1H HSQC spectra of aromatic and sugar resonances were acquired at natural abundance.

4.2.2 Selective ^{13}C $R_{1\varrho}$ Pulse Sequence

The selective $R_{1\varrho}$ pulse sequence is shown in Figure 4.1. Solid, narrow bars represent hard 90° pulses, while the open, narrow ^{13}C pulses apply a tip angle θ = arccot($|\Omega|/\omega_{13C}$), where Ω is the ^{13}C resonance offset from the spinlock and ω_{13C} is the spinlock field strength. Open rectangles represent periods of continuous-wave irradiation for water presaturation (ca. 10 Hz), cross polarization (ω_{CP}, ca. 100 Hz), decoupling CH DD/CSA cross-correlated relaxation and $^1J_{CH}$ evolution (ω_{1H}, ca. 8-10 kHz), and the $R_{1\varrho}$ spinlock (ω_{13C}, 100 – 3500 Hz). Spinlock powers were calibrated as described previously.[18,19] Additional purge elements at the end of the ω_{1H} spinlock are included to aid water suppression. Decoupling during acquisition is accomplished with a 3.5 kHz GARP sequence. For uniformly ^{13}C/^{15}N samples 2.4 kHz and 1.0 kHz GARP decoupling is used on ^{13}C and ^{15}N channels, respectively. A heat compensation element is applied following acquisition for a time T_{max} - T, where T_{max} is the maximum
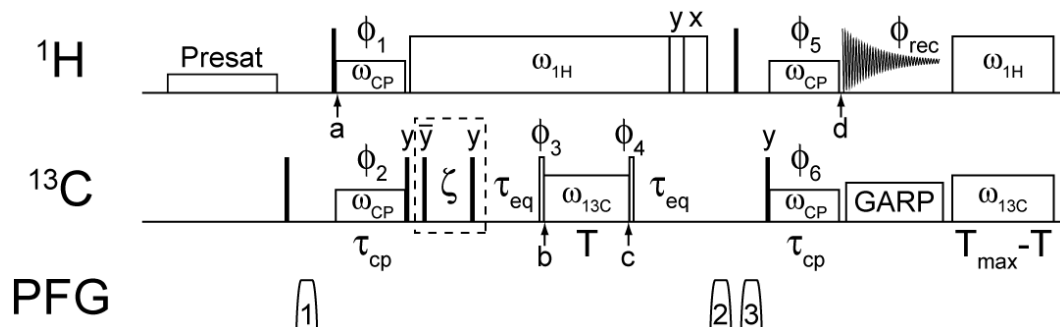
Figure 4.1. Selective ^{13}C $R_{1\varrho}$ pulse sequence for quantifying μs-ms exchange in uniformly labeled and unlabeled nucleic acids. Briefly, proton magnetization is selectively transferred to the carbon spin using weak continuous-wave irradiation (ω_{CP}) where it is then allowed to relax under a variable offset and power spin lock. The magnetization is returned to the proton via another selective cross-polarization for detection and signal intensities are monitored as a function of spin lock time, T, to determine $R_{1\varrho}$ at a given offset and power.

value of T used in the relaxation series. The nearly constant rf irradiation of the proton channel affords excellent water suppression even for ribose and C5 resonances near the water signal. Between points a and d, the ^{1}H carrier is placed on-resonance with the signal of interest while between b and c, the carbon spinlock is placed at a desired offset Ω from the ^{13}C frequency of the resonance of interest. The optional ζ delay (dotted line) can be used to suppress ^{13}C signals with similar ^{1}H frequencies, where $\zeta = \pi/(2\delta)$ and $\delta/(2\pi)$ is the carbon offset (in Hz) of the undesirable signal. Proton decoupling is maintained during the ζ and τ_{eq} delays to prevent $^{1}J_{CH}$ coupling evolution which would lead to anti-phase signals in the 1D spectrum. Delay τ_{eq} allows equilibration of the exchanging spins, optimally ~$3/k_{ex}$, and is set to 5 ms. The maximum length of high power proton spinlock ($T_{max} + \zeta + 2\tau_{eq}$ + purge pulses) is determined by the particular spectrometer hardware. A typical Bruker 600 MHz spectrometer with a cryogenic probe can maintain a 10 kHz spinlock on the proton channel for 200 ms, with 1 second interscan delays. For a T_{max} of 50 ms, this means the ζ delay can be applied up to 140 ms or $\delta/2\pi$ of ~2 Hz without damaging the spectrometer, disregarding of course the presence of additional potentially high power spinlocks and decoupling on the carbon channel. However, the carbon magnetization is decaying quickly in the transverse plane during this time, especially if chemical exchange is present, and the sensitivity will be

significantly diminished. Use of ζ delays up to ~10 ms, or $\delta/2\pi$ of >25 Hz, will likely be tolerable, both to the experiments sensitivity and the spectrometer. The efficacy of the delay can be monitored by replacing the relaxation delay with indirect detection of the carbon spin, as illustrated by Ferrage et al.[20] Gradients 1, 2, and 3 are applied for 1 ms with SMSQ1.100 profiles and amplitudes of 4, 9, and 7.5 G/cm, respectively. The phase cycle is ϕ_1 = {8(y) 8(-y)}, ϕ_2 = {-x x}, ϕ_5 = {4(x) 4(-x)}, ϕ_6 = {2(x) 2(-x)}, ϕ_{rec} = {x -x -x x -x x x - x -x x x -x x -x -x x}. For Ω > 0 (resonance downfield of spinlock), ϕ_3 = -y, ϕ_4 = y. For Ω < 0, ϕ_3 = y, ϕ_4 = -y. Data for eA20 C5 and C2 were acquired using 1536 and 2048 transients, respectively, by setting the selective heteronuclear Hartman-Hahn transfers on-resonance with the desired peak yielding signal:noise ratios > 40:1 at T = 0.
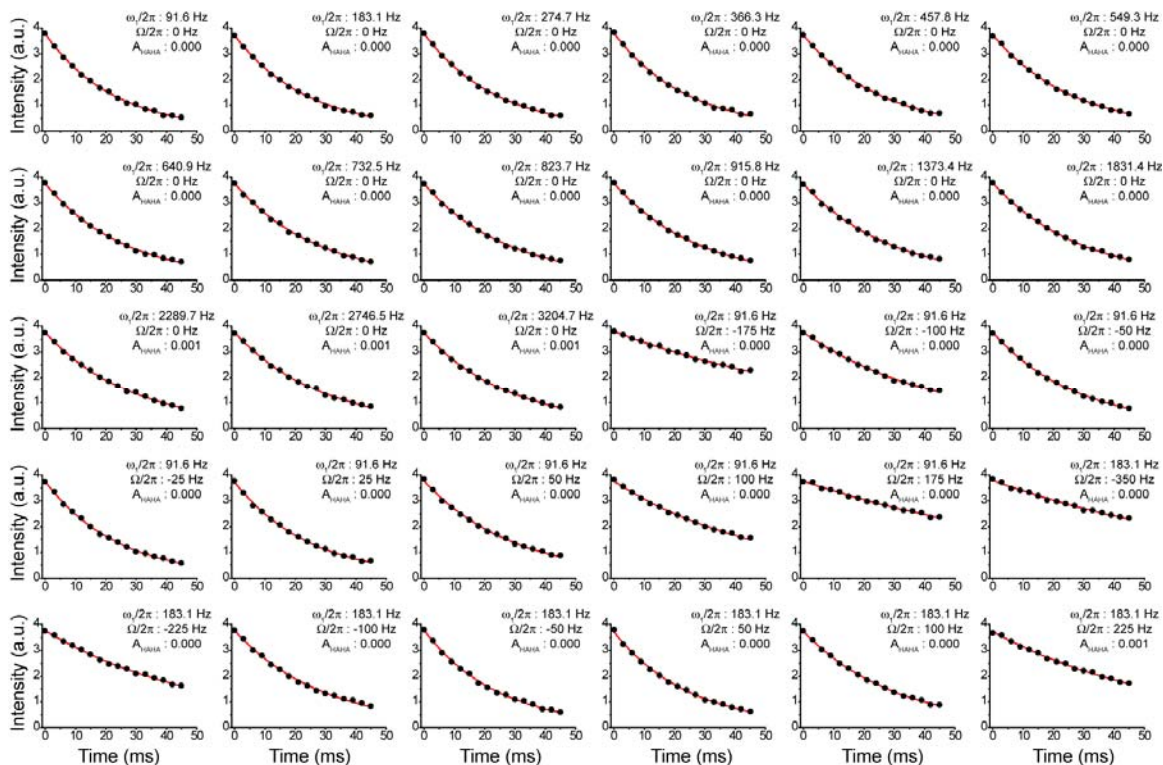
Figure 4.2. Examples of mono-exponential decays for the C2 of A08 at a various offsets and powers, indicated in the frames along with the maximum A_{HAHA} value using Equation 4.1.

4.2.3 Calculating Hartman-Hahn contributions to relaxation

Heteronuclear cross polarization can be achieved with high efficiency as long as $\omega_{CP}/(2\pi)$ is larger than $|J_{CH}| \sqrt{3}/4$. For nucleic acids, a value for $\omega_{CP}/(2\pi)$ of ~70-100 Hz

can therefore be used to minimize transfers to nearby carbon resonances (within about 1.5 x ω_{CP}).[21,22] When using uniformly labeled samples, care must be taken to avoid Hartman-Hahn matching conditions owing to sizable scalar couplings (8-12 Hz) to remote carbons in the aromatic bases and large one-bond homonuclear couplings in both sugar and bases. The maximum efficiency of Hartman-Hahn transfer between spins I and S is given by[23]

$$
A_{HAHA} = \left(1 + \left(\frac{\omega_{eff,I} - \omega_{eff,S}}{J_{IS}(1 + \cos(\theta_I - \theta_S))}\right)^2\right)^{-1}
$$
[4.1]

where $\omega_{eff,X} = (\omega_1^2 + \Omega_X^2)^{1/2}$ is the effective spinlock strength at spin X, J_{IS} is the scalar coupling constant, and $\theta_X = \text{atan}(\omega_1/\Omega_X)$ is the tip angle of the magnetization of spin X with respect to the static magnetic field. In the present study, the chemical shifts of quaternary carbons in purine bases were determined using a TROSY relayed HCCH-COSY experiment.[11] Data with computed A_{HAHA} >1% for the C2-C4 or C2-C6 couplings (using a J_{CC} of -1 Hz) and >0.1% for C2-C5 couplings (J_{CC} = 11 Hz) were removed from the analysis (Table 4.1)[14,16]. Mono-exponential decays were observed for all offset/power combinations for the C2 spins of A08, A10, A92, and A93 and C1' of A93 in the bacterial ribosomal A-site. Example decays are shown in Figure 4.2.

Offset (Hz)	Power (Hz)	A_{HAHA}					
		A08 - C4	A08- C5	A08- C6	A10 - C4	A10 - C5	A10 - C6
0	91.58	0.0000	0.0000	0.0000	0.0000	0.0000	0.0000
0	183.14	0.0000	0.0000	0.0000	0.0000	0.0000	0.0000
0	274.65	0.0000	0.0000	0.0000	0.0000	0.0000	0.0000
0	366.25	0.0000	0.0000	0.0000	0.0000	0.0000	0.0000
0	457.91	0.0000	0.0000	0.0000	0.0000	0.0000	0.0000
0	549.26	0.0000	0.0000	0.0000	0.0000	0.0000	0.0000
0	640.89	0.0000	0.0000	0.0000	0.0000	0.0000	0.0000
0	732.45	0.0000	0.0000	0.0001	0.0000	0.0000	0.0000
0	823.72	0.0000	0.0000	0.0001	0.0000	0.0000	0.0000
0	915.76	0.0000	0.0000	0.0001	0.0000	0.0000	0.0000
0	1373.35	0.0000	0.0000	0.0002	0.0001	0.0000	0.0000
0	1831.39	0.0000	0.0000	0.0003	0.0001	0.0000	0.0001
0	2289.71	0.0001	0.0000	0.0005	0.0002	0.0000	0.0001
0	2746.50	0.0001	0.0000	0.0008	0.0003	0.0000	0.0001
0	3204.65	0.0001	0.0000	0.0011	0.0004	0.0000	0.0002

-175	91.58	0.0000	0.0000	0.0000	0.0000	0.0000	0.0000
-100	91.58	0.0000	0.0000	0.0000	0.0000	0.0000	0.0000
-50	91.58	0.0000	0.0000	0.0000	0.0000	0.0000	0.0000
-25	91.58	0.0000	0.0000	0.0000	0.0000	0.0000	0.0000
25	91.58	0.0000	0.0000	0.0000	0.0000	0.0000	0.0000
50	91.58	0.0000	0.0000	0.0000	0.0000	0.0000	0.0000
100	91.58	0.0000	0.0000	0.0000	0.0000	0.0000	0.0000
175	91.58	0.0000	0.0000	0.0000	0.0000	0.0000	0.0000
-350	183.14	0.0000	0.0000	0.0000	0.0000	0.0000	0.0000
-225	183.14	0.0000	0.0000	0.0000	0.0000	0.0000	0.0000
-100	183.14	0.0000	0.0000	0.0000	0.0000	0.0000	0.0000
-50	183.14	0.0000	0.0000	0.0000	0.0000	0.0000	0.0000
50	183.14	0.0000	0.0000	0.0000	0.0000	0.0000	0.0000
100	183.14	0.0000	0.0000	0.0000	0.0000	0.0000	0.0000
225	183.14	0.0000	0.0000	0.0078	0.0000	0.0000	0.0000
350	183.14	0.0000	0.0000	0.0000	0.0000	0.0000	0.0002
-850	457.91	0.0000	0.0000	0.0000	0.0000	0.0000	0.0000
-625	457.91	0.0000	0.0000	0.0000	0.0000	0.0000	0.0000
-475	457.91	0.0000	0.0000	0.0000	0.0000	0.0000	0.0000
-325	457.91	0.0001	0.0000	0.0000	0.0002	0.0000	0.0000
325	457.91	0.0000	0.0000	0.0001	0.0000	0.0000	0.0002
475	457.91	0.0000	0.0000	0.0000	0.0000	0.0000	0.0000
625	457.91	0.0000	0.0000	0.0000	0.0000	0.0000	0.0000
850	457.91	0.0000	0.0000	0.0000	0.0000	0.0000	0.0000
-1700	915.76	0.0000	0.0000	0.0000	0.0000	0.0000	0.0000
-1100	915.76	0.0000	0.0000	0.0000	0.0000	0.0000	0.0000
-650	915.76	0.0000	0.0000	0.0000	0.0000	0.0000	0.0000
-450	915.76	0.0003	0.0000	0.0000	0.0001	0.0000	0.0000
450	915.76	0.0000	0.0000	0.0001	0.0000	0.0000	0.0002
650	915.76	0.0000	0.0000	0.0000	0.0000	0.0000	0.0000
1100	915.76	0.0000	0.0000	0.0000	0.0000	0.0000	0.0000
1700	915.76	0.0000	0.0000	0.0000	0.0000	0.0000	0.0000
-2500	2289.71	0.0000	**0.0280**	0.0000	0.0000	**0.0030**	0.0000
2500	2289.71	0.0000	0.0000	0.0000	0.0000	0.0000	0.0000
-1800	2746.50	0.0000	0.0000	0.0000	0.0000	0.0001	0.0000
1800	2746.50	0.0000	0.0000	0.0000	0.0000	0.0000	0.0000
-2000	3204.65	0.0000	0.0001	0.0000	0.0000	0.0002	0.0000
2000	3204.65	0.0000	0.0000	0.0000	0.0000	0.0000	0.0000
2800	3204.65	0.0000	0.0000	0.0000	0.0000	0.0000	0.0000
3500	3204.65	0.0000	0.0000	0.0000	0.0000	0.0000	0.0000
4800	3204.65	0.0000	0.0000	0.0000	0.0000	0.0000	0.0000
6000	3204.65	0.0000	0.0000	0.0000	0.0000	0.0000	0.0000

Table 4.1. Hartman-Hahn efficiencies calculated for the C2 spins in A08 and A10 using Equation 4.1. Bold data were excluded from analysis. Spinlock offsets of $(\Omega_{C1'} + \Omega_{C2'})/2 \pm \omega_1$ ($\Omega_{C1'}$ = 87.8 ppm, $\Omega_{C2'}$ = 74.1 ppm) were avoided to prevent Hartman-Hahn matching during the experiments on C1′ of A93.

4.2.4 Analyzing chemical exchange data

Chemical exchange in the ribosomal A-site was determined to be near intermediate exchange ($k_{ex} \approx |\Delta\omega|$) on the NMR timescale. Under these conditions, the simple expression for fast chemical exchange, $R_{1\varrho} = R_1\cos^2\theta + R_{2,0}\sin^2\theta + \sin^2\theta\, \Phi_{ex}\, k_{ex}/(\omega_{eff}^2 + k_{ex}^2)$, where $\Phi_{ex} = p_a p_b \Delta\omega^2$ is used as a single fitting parameter and $\omega_{eff} = (\omega_{13C}^2 + \omega^2)^{1/2}$, is not adequate to accurately determine chemical exchange parameters.[3]   Here, chemical exchange parameters were determined using the expression for asymmetric two-site chemical exchange,

$$R_{1\varrho} = R_1 \cos^2\theta + R_{2,0}\sin^2\theta + \sin^2\theta \frac{p_a p_b \Delta\omega^2 k_{ex}}{(\Omega + \Delta\omega)^2 + \omega_1^2 + k_{ex}^2} \qquad [4.2]$$

where $\Omega \approx \Omega_A$ is the resonance offset from the spinlock carrier, $\tan(\theta) = \omega_1/\Omega_{avg}$, $\Delta\omega = \Omega_B - \Omega_A$, $\Omega_{avg} = p_a\Omega_A + p_b\Omega_B$. The analysis was implemented using Origin v7.0383 (OriginLab Corporation). The best fit parameters, as determined from F-statistics at the 99% confidence level (Table 4.2), yield R_2 of 33.71 ± 0.11 and 22.68 ± 0.42 Hz, $\Delta\omega$ of -0.96 ± 0.02 and -4.33 ± 0.11 ppm for A08 and A93, respectively, and shared p_b of 4.60 ± 0.12 %, and k_{ex} of 3133 ± 77 s^{-1}. The best fit R_2 for A10 is 34.70 ± 0.07 Hz.

Chemical exchange in the unlabeled damaged DNA was determined to be fast ($k_{ex} \gg |\Delta\omega|$) on the NMR timescale. Under these conditions, the chemical shift difference between the exchanging states becomes inseparable from the populations and therefore the simple expression for fast exchange was used. The best fit parameters for the C2 resonance of the damaged base are $k_{ex} = 3.9 \pm 1.2 \times 10^4$ sec^{-1}, $R_1 = 2.87 \pm 0.93$ Hz, $R_{2,0} = 53 \pm 32$ Hz, and $\Phi_{ex} = 3.11 \pm 2.16 \times 10^6$ sec^{-2}.

Residue	N	F-statistic	p-value	R_2 (Hz)	$\Delta\omega/2\pi$ (Hz)	p_b (%)	k_{ex} (s^{-1})
Individual							
A08 C2	56	1092.79	0	37.85 ± 0.06	--	--	--
				33.87 ± 0.12	199.7 ± 15.9	2.28 ± 0.34	2830.9 ± 106.0
A10 C2	56	0.83039	0.483333	**34.70 ± 0.07**	--	--	--
				34.64 ± 0.08	111.4 ± 259.8	0.79 ± 165.3	48.4 ± 10269.5
A93 C1′	64	2078.012	0	56.34 ± 0.22	--	--	--
				22.29 ± 0.46	641.1 ± 16.7	4.63 ± 0.13	3339.7 ± 110.5
Shared p_b,k_{ex}							
A08 C2	120	3.8989	2.30714E-2	**33.71 ± 0.11**	**144.3 ± 2.8**	**4.60 ± 0.12**	**3133.3 ± 76.7**
A93 C1′				**22.68 ± 0.42**	**653.9 ± 16.1**		

Table 4.2. Chemical exchange parameters and statistical analysis of A-site rRNA. In bold are the final parameter choices.

4.3 Results and Discussion

The experiment uses selective Hartmann-Hahn polarization transfers[21] to excite specific spins of interest and collect data in a 1D manner.[9] This scheme is particularly well suited for nucleic acids where chemical exchange is very often limited to a small number of residues in non-canonical regions making it unnecessary to record full multidimensional experiments. The resultant ~100 fold time-saving makes it possible to comprehensively map out the carbon $R_{1\varrho}$ dependence on spin-lock amplitude (ω_1) and offset (Ω) and thus thoroughly characterize the exchange process. It can also obviate the need for isotopic enrichment when working with concentrated nucleic acid samples (>2 mM). One bond C-H scalar coupling ($^1J_{CH}$) evolution and cross correlated relaxation between C-C dipole-dipole and carbon CSA during the relaxation period are efficiently suppressed by a strong ^{1}H continuous wave (CW) field applied on the resonance of interest. By focusing on a single carbon resonance at a time, it becomes trivial to apply appropriately calibrated flip-angle pulses that align magnetization along the effective magnetic field. These features make it possible to employ effective spin lock fields as low as ca. 100 Hz. However, Hartman-Hahn matching conditions must be avoided for the targeted carbons in uniformly labeled samples by choosing appropriate experimental parameters (ω_1, Ω) and/or explicitly computing transfer efficiencies (see §4.2.3).[19,23]

The A-site is a classic example of an RNA that uses conformational dynamics to carry out its function (insets in Figure 4.3). The A-site decodes the mRNA message by dynamically flipping out two internal loop adenines (A92 and A93, insets in Figure 4.3) once a proper codon/anti-codon mini helix is formed between the amino-acyl tRNA and mRNA.[15,24] The A-site is also the target for many antibiotics which bind the internal loop and stabilize a flipped out A92 and A93 conformation.

We used our experiment to probe intrinsic dynamics in the A-site RNA internal loop which may be important for decoding and adaptive recognition. In this unbound form, A92 and A93 adopt a looped in conformation with A93 forming a non-canonical
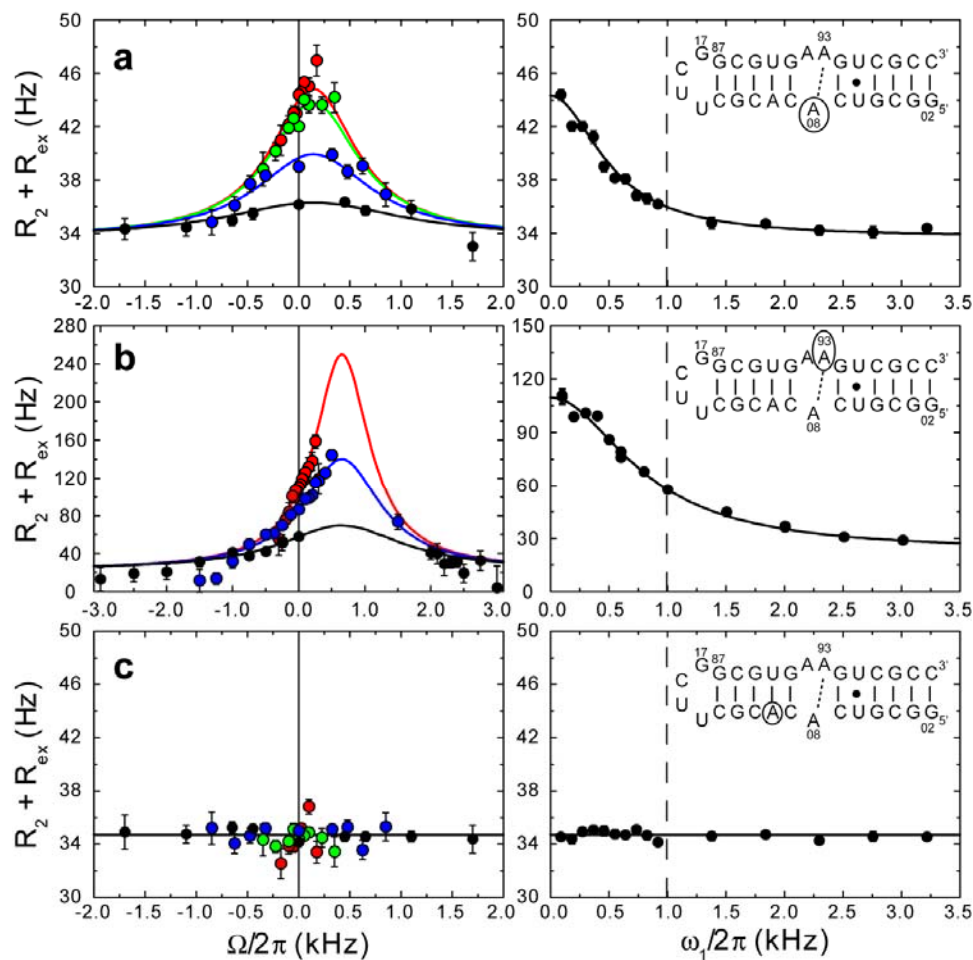
Figure 4.3. Characterizing decoding motions in the ribosomal A-site. The bacterial ribosomal A-site construct is shown in the insets of the right panels. (a-c) Relaxation dispersion profiles for (a) C2 in A08 (b), C1′ in A93 (c), C2 in A10. Shown in left panel is offset and power dependence of R_2 at spinlock powers of ~100 (in red), ~200 (in green), ~500 (in blue), and ~1000 Hz (in black). Shown in right panel is the corresponding on-resonance power dependence of R_2. Dashed lines represent the approximate limit of $R_{1\varrho}$ dispersion experiments measured using conventional 2D relaxation experiments. Solid lines represent the best fit solution to two-site asymmetric chemical exchange.

hydrogen bond with A08.[24] Mono-exponential $R_{1\varrho}$ decays were observed for carbon spin lock fields ranging between 90-3200 Hz (Figure 4.2). The strong offset and spinlock power dependence observed for the C2 R_2 of residue A08 (Figure 4.3a) and C1′ R_2 of residue A93 (Figure 4.3b) demonstrates existence of exchange at the internal loop. Importantly, this process would be difficult if not impossible to characterize by conventional methods since the observed exchange is already nearly completely

suppressed at ~1000 Hz spin lock fields (Figure 4.3a-b, right panels). In contrast to the internal loop, we did not observe any evidence for exchange at A10 in the canonical helix (Figure 4.3c).

Data from loop residues A08 and A93 could be fit simultaneously to a single exchange process with time constant of 319 ± 8 μs and a low populated (4.6 ± 0.1%) "invisible" state. The measured time constant is short compared to decoding (~10 ms) and could reflect internal fluctuations that disrupt the A08-A93 base-pair and thus enhance the looping out of A93. The new experiment also allowed us to thoroughly map the offset dependence of R_2 for C2 in A08 and C1' in A93 and thus deduce the sign of the chemical shift difference ($\Omega = -\Delta\omega$, see §4.2.4). This is not feasible using either on-resonance $R_{1\varrho}$ or CPMG experiments at multiple static magnetic fields as noted by Palmer and co-workers.[25]

The dramatic time-saving and sensitivity boost afforded by the new experiment makes possible the quantitative characterization of chemical exchange in unlabeled samples. This is particularly important for nucleic acids containing chemical modifications which cannot be easily isotopically enriched. This includes a wide-range of DNA lesions in which motions are believed to play an important role in the recognition by repair enzymes.[26] To this end, we used our experiment to probe exchange dynamics in a DNA duplex containing a 1,N6-ethenoadenine (eA) lesion (Figure 4.4a). This allowed us for the first time to use relaxation dispersion to quantify dynamic exchange at a damaged DNA site.

The well-resolved C2H2 and C5H5 resonances in eA (Figure 4.4b) provided ideal probes for measuring exchange at the damaged site. Anomalously weak intensities indicative of chemical exchange were observed for the eA20 resonances. A small albeit significant offset and power-dependence for R_2 was observed for C2 in eA20 (Figure 4.4c), which was measured in a constant-time manner to further reduce experiment time and because Hartman-Hahn transfers are not a concern in unlabeled samples. In contrast, the power-dependence for R_2 measured in an identical sample lacking the

damaged base was negligible (Figure 4.4c, open symbols). Despite the relatively large intrinsic R_2, which can be attributed to elevated viscosity due to high DNA concentration (~5 mM), and the very fast timescale of the exchange, the time constant for the eA20 exchange process could be reliably determined to be 26 ± 8 μs. This faster process may reflect transient destacking of eA20 that may help present the damaged base to repair enzymes.
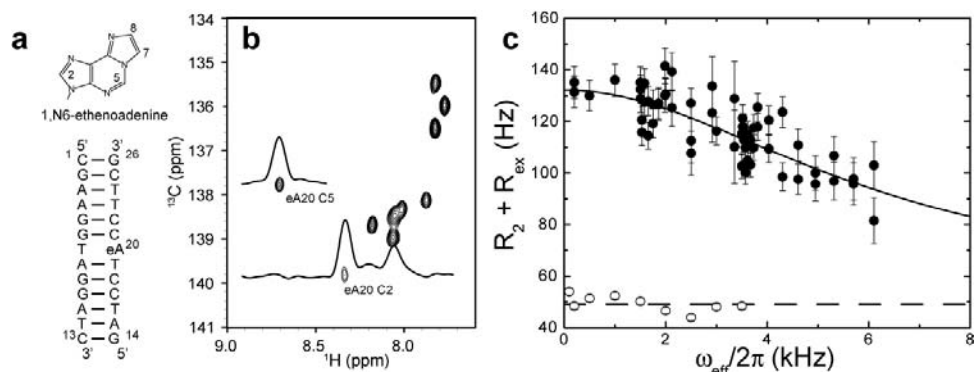

Figure 4.4. Quantifying chemical exchange in an unlabeled 1,N6-ethenoadenine damaged 26mer DNA. (a) DNA sequence and chemical structure of the 1,N6-ethenoadenine base. (b) 2D ^{1}H-^{13}C correlation spectrum of the DNA sample at 14.4 T and 25°C with 1D overlays to illustrate sensitivity and selectivity of the pulse sequence in Figure 1. (c) The effective-field dependence of R_2+R_{ex}.. A sequence where eA20 is replaced with an adenine was used as a control (open symbols, C8 spin of A20).

4.4 Conclusion

In conclusion, we have presented an NMR experiment for quantifying exchange dynamics over a broad range of timescales in both labeled and unlabeled nucleic acid samples. While the applications presented here are found to be in intermediate-fast exchange, the ability to use very weak spinlock fields with this experiment affords the opportunity to reveal millisecond timescale motions in nucleic acids. This significantly expands the potential for site-specifically characterizing biologically important motions in a range of nucleic acid systems that have so far proven difficult to quantify reliably by conventional methods.

4.5 References

1. Al-Hashimi, H.M. & Walter, N.G. RNA dynamics: it is about time. *Current Opinion In Structural Biology* **18**, 321-329 (2008).

2. Furtig, B. et al. Time-resolved NMR studies of RNA folding. *Biopolymers* **86**, 360-383 (2007).

3. Palmer, A.G. & Massi, F. Characterization of the dynamics of biomacromolecules using rotating-frame spin relaxation NMR spectroscopy. *Chemical Reviews* **106**, 1700-1719 (2006).

4. Mittermaier, A. & Kay, L.E. Review - New tools provide new insights in NMR studies of protein dynamics. *Science* **312**, 224-228 (2006).

5. Shajani, Z. & Varani, G. NMR studies of dynamics in RNA and DNA by C-13 relaxation. *Biopolymers* **86**, 348-359 (2007).

6. Latham, M.R., Brown, D.J., McCallum, S.A. & Pardi, A. NMR methods for studying the structure and dynamics of RNA. *Chembiochem* **6**, 1492-1505 (2005).

7. Lundstom, P., Hansen, D.F. & Kay, L.E. Measurement of carbonyl chemical shifts of excited protein states by relaxation dispersion NMR spectroscopy: comparison between uniformly and selectively C-13 labeled samples. *Journal Of Biomolecular Nmr* **42**, 35-47 (2008).

8. Massi, F., Johnson, E., Wang, C.Y., Rance, M. & Palmer, A.G. NMR R-1 rho rotating-frame relaxation with weak radio frequency fields. *Journal Of The American Chemical Society* **126**, 2247-2256 (2004).

9. Korzhnev, D.M., Orekhov, V.Y. & Kay, L.E. Off-resonance R1(p) NMR studies of exchange dynamics in proteins with low spin-lock fields: An application to a fyn SH3 domain. *Journal Of The American Chemical Society* **127**, 713-721 (2005).

10. Sklenar, V., Peterson, R.D., Rejante, M.R. & Feigon, J. 2-Dimensional And 3-Dimensional Hcn Experiments For Correlating Base And Sugar Resonances In N-15,C-13-Labeled Rna Oligonucleotides. *Journal Of Biomolecular Nmr* **3**, 721-727 (1993).

11. Simon, B., Zanier, K. & Sattler, M. A TROSY relayed HCCH-COSY experiment for correlating adenine H2/H8 resonances in uniformly C-13-labeled RNA molecules. *Journal Of Biomolecular Nmr* **20**, 173-176 (2001).

12. Furtig, B., Richter, C., Wohnert, J. & Schwalbe, H. NMR spectroscopy of RNA. *Chembiochem* **4**, 936-962 (2003).

13. Xia, Y.L. et al. IP-COSY, a totally in-phase and sensitive COSY experiment. *Magnetic Resonance In Chemistry* **43**, 372-379 (2005).

14. Fiala, R., Munzarova, M.L. & Sklenar, V. Experiments for correlating quaternary carbons in RNA bases. *Journal Of Biomolecular Nmr* **29**, 477-490 (2004).

15. Fourmy, D., Yoshizawa, S. & Puglisi, J.D. Paromomycin binding induces a local conformational change in the A-site of 16 S rRNA. *Journal Of Molecular Biology* **277**, 333-345 (1998).

16. Wijmenga, S.S. & van Buuren, B.N.M. The use of NMR methods for conformational studies of nucleic acids. *Progress In Nuclear Magnetic Resonance Spectroscopy* **32**, 287-387 (1998).

17. Kouchakdjian, M. et al. Nmr-Studies Of The Exocyclic 1,N(6)-Ethenodeoxyadenosine Adduct (Epsilon-Da) Opposite Thymidine In A Dna Duplex - Nonplanar Alignment Of Epsilon-Da(Anti) And Dt(Anti) At The Lesion Site. *Biochemistry* **30**, 1820-1828 (1991).

18. Guenneugues, M., Berthault, P. & Desvaux, H. A method for determining B-1 field inhomogeneity. Are the biases assumed in heteronuclear relaxation experiments usually underestimated? *Journal Of Magnetic Resonance* **136**, 118-126 (1999).

19. Hansen, A.L. & Al-Hashimi, H.M. Dynamics of large elongated RNA by NMR carbon relaxation. *Journal Of The American Chemical Society* **129**, 16072-16082 (2007).

20. Ferrage, F., Eykyn, T.R. & Bodenhausen, G. Frequency-switched single-transition cross-polarization: A tool for selective experiments in biomolecular NMR. *Chemphyschem* **5**, 76-84 (2004).

21. Pelupessy, P., Chiarparin, E. & Bodenhausen, G. Excitation of selected proton signals in NMR of isotopically labeled macromolecules. *Journal Of Magnetic Resonance* **138**, 178-181 (1999).

22. Pelupessy, P. & Chiarparin, E. Hartmann-Hahn polarization transfer in liquids: An ideal tool for selective experiments. *Concepts In Magnetic Resonance* **12**, 103-124 (2000).

23. Bax, A. & Davis, D.G. Practical Aspects Of Two-Dimensional Transverse Noe Spectroscopy. *Journal Of Magnetic Resonance* **63**, 207-213 (1985).

24. Fourmy, D., Recht, M.I., Blanchard, S.C. & Puglisi, J.D. Structure of the A site of Escherichia coli 16S ribosomal RNA complexed with an aminoglycoside antibiotic. *Science* **274**, 1367-1371 (1996).

25. Trott, O. & Palmer, A.G. R-1 rho relaxation outside of the fast-exchange limit. *Journal Of Magnetic Resonance* **154**, 157-160 (2002).

26. Yang, W. Structure and mechanism for DNA lesion recognition. *Cell Research* **18**, 184-197 (2008).

Chapter 5. Conclusion

The study of nucleic acids by NMR has come a long way since the initial studies of polydisperse RNAs and DNAs. While always in the shadow of achievements made in protein studies, many obstacles have been overcome and the field continues to push to ever larger systems and more complex problems. However, there are a number of significant challenges still to overcome. As discussed in chapters 1 and 3, the numerous carbon-carbon interactions complicate almost every quantitative study of dynamics in nucleic acids. Developments in specific isotope labeling of large proteins have been instrumental in being able to study complexes of up to 1 MDa in size.[1] Likely, similar efforts will be beneficial for the study of large nucleic acids as well. With an increase in size, it also can become difficult to accurately measure scalar and dipolar couplings as cross-correlated relaxation begins to devastate the anti-TROSY component of the splittings, whereas the measurement of the TROSY component alone may be necessary to obtain pseudo-CSA restraints.[2] However, it is a valid assessment that still not enough is known about how the nucleobase CSAs vary in different structural environments. Brumovska et al. showed using DFT calculations how something simple, like the glycosidic bond angle, may have a profound impact on the pyrimidine C6 and purine C8 CSA tensors[3] while Czernek has demonstrated significant effects that hydrogen bonding has on the proton and nitrogen CSAs.[4,5] It will be important in the future to characterize and validate these differences experimentally.

5.1 Investigating Excited States of Nucleic Acids

RNA achieves much of its functional diversity and complexity by undergoing dramatic conformational rearrangements in response to a variety of cellular signals.[6] For

146

example, riboswitches, cis-acting gene control elements found in the 5′ UTR of many mRNAs, regulate gene expression in response to changes in a particular physiological parameter. Purine-sensing riboswitches accomplish this by forming a transcription (anti)terminator helix at a downstream decision-making expression platform when the physiological concentration of the specific purine under control reaches a predefined threshold.[7] Recently these RNAs have attracted interest as potential antibacterial targets, given their abundance in bacteria and their ability to bind small molecules. The guanine-sensing riboswitch (G-switch) in particular is found in many bacterial species, including the pathogen associated with anthrax, and is thought to exist as several slowly (30-60 s^{-1}) interconverting conformers in the absence of guanine.[8] Understanding these dynamics will likely be crucial in developing successful new antibiotics. The techniques developed in this thesis are an important step towards these goals.

Traditionally, deciphering the function of such a system has relied on the production of stable "snapshots", often derived from X-ray crystallography or solution NMR spectroscopy. Unfortunately, due in part to the limitations of current biophysical techniques, this disregards higher energy "excited" state conformations which are at least equally biologically relevant. In the past year, novel solution NMR relaxation dispersion techniques have been developed, making it possible to investigate the structure of low-populated excited states in proteins with lifetimes on the millisecond timescale.[9] Much of the success of these new experiments depends on the ability to prepare isotopically labeled samples with isolated NMR probes. This prevents unfavorable interference between pairs of probes that would otherwise make data analysis intractable. Similar specific isotope[10] and segmental labeling strategies[11] are already being developed for the study of large RNAs. This involves studying bacterial metabolic pathways to find and exploit an appropriate system that can produce ideal isotope labeling patterns for nucleic acids.[10,12,13] An exciting future project would therefore be to investigate the underlying structure and dynamics of the ~70 nucleotide (nt) G-switch aptamer domain to provide a molecular understanding of how riboswitches sense and convey cellular signals.

The first step in any biomolecular study by NMR is the chemical shift assignment of the spectra. An effective approach to overcome the inherent spectral congestion of large nucleic acids will be to use and develop isotopic and segmental labeling strategies mentioned above.[10,11,14-16] Following the method proposed by Tzakos et al.,[11] the G-switch could be prepared by labeling the first ~40 nts with ^{13}C and the last ~30 nts with ^{15}N, and vice versa, thereby reducing the spectral complexity to that of more conventionally sized RNAs. Various other labeling strategies and the development of ever more efficient experimental techniques can be pursued to maximize spectral sensitivity and resolution. Following successful resonance assignments, the fundamental dynamics of the system and changes upon drug binding can be investigated. While the techniques developed in this thesis will provide an excellent point of reference to begin these studies, specific isotope labeling strategies that can eliminate homonuclear interactions would be invaluable for recording accurate spin relaxation studies. Utilizing these techniques, new RNA-specific NMR experiments based on those for studying excited states in proteins can be developed.[9,17] An initial investigation of the ps-ns motions using the experiments developed in Chapter 3 will help identify potential regions of interest. The extracted NMR parameters (ie. chemical shifts, bond vector orientations, and exchange rates) would potentially allow the calculation of structures of the invisible excited states of the G-switch as well as the kinetics and thermodynamics of the interconversion between the states. Finally, these experiments can be repeated in the presence of guanine analogs, such as 7-deazaguanine (since guanine is highly insoluble), to investigate the change in dynamics upon ligand binding providing important details about the signaling event. This information will provide key insight into how this molecule functions and allow us to generate an energy landscape describing the process.

5.2 Sequence dependence of nucleic acid CSA tensors using SS-NMR

There are two obstacles to overcome when measuring CSAs in polynucleotides via SS NMR (i) overlap in chemical shift powder patterns and (ii) extraction of orientational

information since suitably large single crystals of oligonucleotides are difficult to obtain. These issues, however, can be addressed with recent advances in solid state NMR methodology. Using techniques such as five π replicated magic angle turning (FIREMAT)[18] or stroboscopic phase encoding in the evolution dimension (SPEED) under magic angle spinning (MAS),[19] one can separate the isotropic and anisotropic chemical shift into two dimensions, encoding the anisotropic interaction to their separate isotropic shifts, thereby eliminating the majority of the spectral overlap of the powder patterns. Analysis of the powder patterns provides highly accurate information about the magnitude of the chemical shift, but unfortunately lacks the ability to define the principle value orientations with respect to the molecular frame. However, if a given carbon nucleus neighbors a ^{14}N nucleus, as is the case for all but the pyrimidine C5 carbon in the nucleobases, the orientation of the ^{13}C-^{14}N dipolar interaction can be determined in the chemical shift principle axis frame, successfully reviving CSA orientational information of the rigid, aromatic nucleobases.[20,21] Moreover, once we obtain the CSA magnitudes from solid state NMR, it will be more feasible to refine the CSA orientations on the basis of our measured RCSAs. A number of small RNA and DNA helices with a single uniformly labeled residue can be designed to investigate any number of structural configurations. An exciting alternative to this would avert the need for singly labeling the RNA or DNA. Wylie et al.[22] proposed an elegant 2-dimensional technique whereby slow-spinning ^{15}N-^{13}CO correlation spectra were recorded using SPECIFIC[23] cross polarization on a ^{13}C/^{15}N enriched protein where only carbonyl carbons are labeled. Sidebands of the entire 2D spectrum are recorded in a single experiment, the intensities of which can be analyzed to obtain site-specific principle values of both the ^{13}CO and ^{15}N CSA tensors. This technique is directly applicable for the specific-isotope labeled purines of RNAs,[10] although other isotope labeling strategies could be pursued as discussed in §5.1. Either of these studies would prove to be crucial in understanding the, as of yet, unknown trends related to CSA variations in nucleic acids.

5.3 References

1. Sprangers, R. & Kay, L.E. Quantitative dynamics and binding studies of the 20S proteasome by NMR. *Nature* **445**, 618-622 (2007).

2. Grishaev, A., Ying, J.F. & Bax, A. Pseudo-CSA restraints for NMR refinement of nucleic acid structure. *Journal Of The American Chemical Society* **128**, 10010-10011 (2006).

3. Brumovska, E. et al. Effect of local sugar and base geometry on C-13 and N-15 magnetic shielding anisotropy in DNA nucleosides. *Journal Of Biomolecular Nmr* **42**, 209-223 (2008).

4. Czernek, J. An ab initio study of hydrogen bonding effects on the N-15 and H-1 chemical shielding tensors in the Watson-Crick base pairs. *Journal Of Physical Chemistry A* **105**, 1357-1365 (2001).

5. Czernek, J., Fiala, R. & Sklenar, V. Hydrogen bonding effects on the N-15 and H-1 shielding tensors in nucleic acid base pairs. *Journal Of Magnetic Resonance* **145**, 142-146 (2000).

6. Al-Hashimi, H.M. & Walter, N.G. RNA dynamics: it is about time. *Current Opinion In Structural Biology* **18**, 321-329 (2008).

7. Kim, J.N. & Breaker, R.R. Purine sensing by riboswitches. *Biology Of The Cell* **100**, 1-11 (2008).

8. Gilbert, S.D., Stoddard, C.D., Wise, S.J. & Batey, R.T. Thermodynamic and kinetic characterization of ligand binding to the purine riboswitch aptamer domain. *Journal Of Molecular Biology* **359**, 754-768 (2006).

9. Vallurupalli, P., Hansen, D.F. & Kay, L.E. Probing structure in invisible protein states with anisotropic NMR chemical shifts. *Journal Of The American Chemical Society* **130**, 2734-+ (2008).

10. Schultheisz, H.L., Szymczyna, B.R., Scott, L.G. & Williamson, J.R. Pathway engineered enzymatic de novo purine nucleotide synthesis. *Acs Chemical Biology* **3**, 499-511 (2008).

11. Tzakos, A.G., Easton, L.E. & Lukavsky, P.J. Complementary segmental labeling of large RNAs: Economic preparation and simplified NMR spectra for measurement of more RDCs. *Journal Of The American Chemical Society* **128**, 13344-13345 (2006).

12. Johnson, J.E., Julien, K.R. & Hoogstraten, C.G. Alternate-site isotopic labeling of ribonucleotides for NMR studies of ribose conformational dynamics in RNA. *Journal Of Biomolecular Nmr* **35**, 261-274 (2006).

13. Hoogstraten, C.G. & Johnson, J.E. Metabolic labeling: Taking advantage of bacterial pathways to prepare spectroscopically useful isotope patterns in proteins and nucleic acids. *Concepts In Magnetic Resonance Part A* **32A**, 34-55 (2008).

14. Dayie, K.T. Key labeling technologies to tackle sizeable problems in RNA structural biology. *International Journal Of Molecular Sciences* **9**, 1214-1240 (2008).

15. Kishore, A.I., Mayer, M.R. & Prestegard, J.H. Partial C-13 isotopic enrichment of nucleoside monophosphates: useful reporters for NMR structural studies. *Nucleic Acids Research* **33**(2005).

16. Nelissen, F.H.T. et al. Multiple segmental and selective isotope labeling of large RNA for NMR structural studies. *Nucleic Acids Research* **36**(2008).

17. Hansen, D.F., Vallurupalli, P., Lundstrom, P., Neudecker, P. & Kay, L.E. Probing chemical shifts of invisible states of proteins with relaxation dispersion NMR spectroscopy: How well can we do? *Journal Of The American Chemical Society* **130**, 2667-2675 (2008).

18. Alderman, D.W., McGeorge, G., Hu, J.Z., Pugmire, R.J. & Grant, D.M. A sensitive, high resolution magic angle turning experiment for measuring chemical shift tensor principal values. *Molecular Physics* **95**, 1113-1126 (1998).

19. Strohmeier, M. & Grant, D.M. A new sensitive isotropic-anisotropic separation experiment - SPEED MAS. *Journal Of Magnetic Resonance* **168**, 296-306 (2004).

20. Strohmeier, M., Alderman, D.W. & Grant, D.M. Obtaining molecular and structural information from C-13-N-14 systems with C-13 FIREMAT experiments. *Journal Of Magnetic Resonance* **155**, 263-277 (2002).

21. Strohmeier, M. & Grant, D.M. Experimental and theoretical investigation of the C-13 and N-15 chemical shift tensors in melanostatin-exploring the chemical shift tensor as a structural probe. *Journal Of The American Chemical Society* **126**, 966-977 (2004).

22. Wylie, B.J. et al. Chemical-shift anisotropy measurements of amide and carbonyl resonances in a microcrystalline protein with slow magic-angle spinning NMR spectroscopy. *Journal Of The American Chemical Society* **129**, 5318-+ (2007).

23. Baldus, M., Petkova, A.T., Herzfeld, J. & Griffin, R.G. Cross polarization in the tilted frame: assignment and spectral simplification in heteronuclear spin systems. *Molecular Physics* **95**, 1197-1207 (1998).